

**INVESTIGATIONS OF THE FLOW AND PINNING
PHENOMENA IN RADIAL FLOW REACTORS**

BY

AQEEL AHMAD KAREERI

A Thesis Presented to the
DEANSHIP OF GRADUATE STUDIES

KING FAHD UNIVERSITY OF PETROLEUM & MINERALS

DHAHRAN, SAUDI ARABIA

In Partial Fulfillment of the
Requirements for the Degree of

MASTER OF SCIENCE

In

CHEMICAL ENGINEERING

December, 2004


KING FAHD UNIVERSITY OF PETROLEUM & MINERALS
DHAHRAN 31261, SAUDI ARABIA

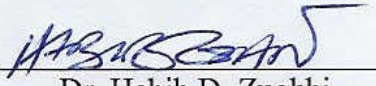
DEANSHIP OF GRADUATE STUDIES


This thesis, written by **AQEEL AHMAD KAREERI** under the direction of his thesis advisors and approved by his thesis committee, has been presented to and accepted by the Dean of Graduate Studies, in partial fulfillment of the requirements for the degree of


MASTER OF SCIENCE IN CHEMICAL ENGINEERING


Thesis Committee


Dr. Habib H. Al-Ali
(Thesis Advisor)


Dr. Habib D. Zughbi
(Co-Advisor)


Prof. Mohamed B. Amin
(Department Chairman)


Prof. Mazen Shalabi
(Member)


Dr. Mohammad Al-Ohali
(Dean of Graduate Studies)


Dr. Usamah Al-Mubaiyedh
(Member)


Date

25-5-2005




Dr. Nadhir Al-Baghli
(Member)

**Dedicated to my parents & my brother Abdulhameed
and my wife & my children: Ahmad, Reham and Zakaria**

ACKNOWLEDGMENTS

In the name of ALLAH, the Most Beneficent, the Most Merciful.

All praise and glory be to ALLAH (SWT) who gave me the courage and patience to carry out this work and peace and blessings of ALLAH be upon the prophet, Mohammad (SAWA). Acknowledgment is due to the Saudi ARAMCO company for supporting my master program and for King Fahd University of Petroleum & Minerals for supporting this research. Also acknowledgment is due to Ras Tannura Refinery Managements for supporting me during my Master program.

I wish to express my appreciation to my thesis advisor Dr. Habib H. Al-Ali and co-advisor Dr. Habib D. Zughbi for their invaluable support, encouragement, and patient guidance. I wish also to thank my thesis committee members Professor Mazen Shalabi, Dr. Usamah Al-Mubaiyedh, Dr. Nadhir Al-Baghli, and Dr. Ashraf Fatehi for their valuable comments and suggestion. Completion of this work would not be possible without their support. I would like to thank Professor M. B. Amin, chairman of the Chemical Engineering Department, and all the CHE department faculty members for their support during my Master program. Especial thanks for CHE Lab staff, Kamal Ahmad, Mehdi Saffar, Romeo Caroeso and Ibrahim Salem, for their support of the experimental part of this research

I would like to thanks Professor H. I. Al-AbdulWahhab, chairman of the Civil Engineering Department, Mr Saleh H. Zakariy, and M. H. Essa, from Soil Mechanics Lab, Dr. Adly Saaffeen, from the Earth Sciences Department, and Musaed Al-

Ghamdi, from the Research Institute, for their support of the experimental part of this research.

I appreciate the help of Waleed Al-Dossary and Saeed Al-Ghamdi, Ras Tanura Refinery engineer, in getting drawings and operating data for refinery processes. I would like to thank SABIC KEMYA for providing us with the HDPE that was used in this research. I am also thankful to my friends, Bassem Al-Harthy and Wajeh Malibary, for their help in selecting the solid materials for the experimental part of this research. I also would like to thank all the CHE graduate students for their discussion and cooperation.

Finally, a great thank to my parents for their help and support. Also I would like to thank all my family members for their encouragement and support.

TABLE OF CONTENTS

ACKNOWLEDGMENTS	iii
TABLE OF CONTENTS	v
LIST OF TABLES	ix
LIST OF FIGURES.....	x
THESIS ABSTRACT	xv
ARABIC ABSTRACT	xvii
CHAPTER 1	1
INTRODUCTION	1
1.1 Packed Bed Reactor.....	1
1.2 Radial Flow Reactor	1
1.2.1 A Radial Flow Moving Bed Reactor (RFMBR)	4
1.2.2 Pinning.....	6
1.3 Computational Fluid Dynamics CFD.....	8
CHAPTER 2	12
LITERATURE REVIEW.....	12
2.1 Radial Flow Fixed Bed Reactors (RFBR)	12
2.2 Radial Flow Moving Bed Reactors RFMBR.....	16
2.3 Reforming Moving Bed Reactors.....	24
2.4 Summary of Literature Review	25
2.5 Objectives of the Current Study.....	25
CHAPTER 3	27
MATHEMATICAL FORMULATION	27
3.1 Radial Flow Fixed Bed Reactors RFBR.....	27

3.2 Radial Flow Moving Bed Reactors (RFMBR).....	29
3.2.1 The Eulerian model.....	30
3.2.2 The Eulerian Granular Model (EGM)	30
3.2.3 The Conservation Equations.....	31
3.2.4 The Solid Pressure Equation	32
3.2.5 The Granular Temperature	33
3.2.6 The Stress Tensor	35
3.2.7 The Drag Force.....	36
3.2.8 Modeling of Turbulence	38
3.2.9 Initial and Boundary Conditions	39
3.3 The Solution Methodology	41
3.4 The Grid System.....	44
3.5 Solver Types.....	44
3.5.1 The Segregated Solution Method	45
3.5.2. The Coupled Solution Method.....	47
3.6 Multiphase Solution Method	47
CHAPTER 4	49
SIMULATION OF FLOW IN A RADIAL FLOW FIXED BED REACTOR (RFBR)	49
4.1 Introduction.....	49
4.2 Reactor Dimensions and Operating Conditions.....	49
4.2.1 Simulation Results	51
4.2.3 Effects of the Mesh Size	59
4.3 Analysis of the Flow Distribution in an RFBR	67
4.3.1 Analysis the Annular Channel and Center Pipe Flow Profiles.....	69
4.3.2 Predictions of the Annular and Center Pipe Pressure Profiles	72
4.3.3 The Reactor Dimensions and Operating Conditions	74
4.3.4 Simulation Results for CP-z Configuration.....	74
4.3.5 Simulation Results for CP- π Configuration	80
4.3.6 Simulation Results for CF- π Configuration	80
4.3.7 Simulation Results for CF-z Configuration	90
4.3.8. Uniformity Analysis for the Four Configurations.....	90

CHAPTER 5	99
VALIDATION OF THE NUMERICAL MODEL AND PARAMETRIC STUDY	99
5.1 CFD Model Validation.....	99
5.1.1 Validation Against Heggs <i>et al.</i> (1995).....	99
5.1.2 Validation Against Song <i>et al.</i> (1993).....	108
5.2 Parametric Study.....	110
5.2.1 Effects of the Center Pipe Porosity	111
5.2.2 Effects of a Low Center Pipe and a High Annular Channel Porosity	111
5.2.3 Effects of the Bed Porosity.....	115
5.2.4 Effects of the Ratio of the Center Pipe to the Annular Channel Cross Sectional Area	115
5.2.5 Effects of Partially Blocking the Center Pipe Top Part.....	118
CHAPTER 6	123
SIMULATIONS OF A MOVING BED REACTOR.....	123
6.1 Introduction.....	123
6.2 Moving Bed with a Side Flow Inlet.....	124
6.3 Moving Bed with a Cross Gas Flow.....	124
6.3.1 Effects of the Gas Velocity.....	130
6.3.2 Effects of the Solid Particle Density	130
6.3.3 Effects of the Solid Particle Diameter Size.....	130
6.4 Moving Bed CFD Model Limitations	135
CHAPTER 7	136
EXPERIMENTAL WORK	136
7.1 Introduction.....	136
7.2 Experimental Set Up.....	136
7.3 Characterization of Solid Particles.....	139
7.3.1 Solid Particles size.....	139
7.3.2 Solid Particles Form and Sphericity	141
7.3.3 Solid Particles Density, Bulk Density and Void Fraction	142

7.3.4 Solid Particles Angles of Internal and Wall Frictions	143
7.4 Experimental Results.....	144
7.4.1 Effect of the Flow Rate.....	144
7.4.2 Effect of the Flow distribution in the Air Feed Chamber	146
7.4.3 Using 1/2 inch Inlet Pipe with Distributor.....	154
7.4.4 Effects of the Solid Particles Properties.	158
7.4.5 Solid Particles Fluidization	161
CHAPTER 8	163
CONCLUSIONS AND RECOMMENDATIONS	163
8.1 Conclusions	163
8.2 Recommendations.....	165
REFERENCES	166

LIST OF TABLES

Table 4.1: Reactor dimensions.....	51
Table 4.2: Boundary conditions.....	51
Table 4.3: Maximum deviation from the uniform flow for the four radial flow configurations.	96
Table 5.1: Filter dimensions	101
Table 5.2: Bed layer specifications.....	101
Table 5.3: A comparison of the pressure measurements of Heggs <i>et al.</i> (1995) and the current predictions at different flow rates.	102
Table 5.4: The dimensions of the reactor used by Song <i>et al.</i> (1993)	108
Table 6.1: Boundary conditions of the RFMBR model.....	127
Table 7.1: Size distributions of particles.....	139
Table 7.2: Solid particles average size and variation coefficient.....	141
Table 7.3: Solid particles form and sphericity.....	142
Table 7.4: Solid particles density, bulk density and void fraction.....	143
Table 7.5: Solid particles angles of internal and wall frictions.....	144
Table 7.6: Bed pressure drop and flow rate for the four inlet configurations at cavity initiation and total pinning.	154
Table 7.7: Bed pressure drop and flow rate for 1/2 inch inlet pipe with and without distributor at cavity initiation and total pinning.....	156
Table 7.8: Solid material properties.....	158
Table 7.9: Bed pressure drop and flow rate for various solid materials at cavity initiation.	159

LIST OF FIGURES

Figure 1.1: An axial flow and a radial flow reactors.	2
Figure 1.2: A radial flow fixed bed reactor (RFBR).....	3
Figure 1.3: A radial flow moving bed reactor (RFMBR).	5
Figure 1.4: Forms of the catalyst bed movement: (1) Totally moving bed, (2) Partially pinned bed, (3) Totally pinned bed.	7
Figure 2.1: The four possible flow configurations for an RFBR.....	13
Figure 2.2: A schematic diagram of the geometry used by Ginestra and Jackson (1985).....	18
Figure 2.3: Theoretical and experimental cavity wall profiles by Ginestra and Jackson (1985), where π is a dimensionless pressure drop factor.....	20
Figure 2.4: The RFMBR used by Doyle <i>et al.</i> (1986).	22
Figure 3.1: A schematic diagram of the RFMBR.....	40
Figure 3.2: Overview of the segregated solution method.	46
Figure 3.3: Overview of the coupled solution method.	48
Figure 4.1: A schematic diagram of a radial flow reactor, where L_s , L_p and L_b are the lengths of the seal layer, the perforation section and the bed, respectively, D_{cp} and D_r are the diameters of the center pipe and the reactor, respectively and D_b is the outer bed diameter.....	50
Figure 4.2: The grid for the radial flow reactor.	52
Figure 4.3: A profile of the annular channel velocity in an x-z plane along a line passing through the center of the annulus.....	54
Figure 4.4: (a) Static pressure contours in a vertical centered plane (x-z plane), (b) magnified velocity vectors in a vertical centered plane (x-z plane).	55
Figure 4.5: Velocity profile along the reactor diameter, at the center of the bed $z=1$ m.	56
Figure 4.6: Velocity profile along catalyst bed section, at the center of the bed $z=1$ m.	57

Figure 4.7: A profile of the velocity in the center pipe along the bed length, at the center of an x-z plane of the channel.	58
Figure 4.8: The velocity profile along the reactor diameter, at the center of the bed z=1 m, for five different mesh sizes.....	60
Figure 4.9: The annular channel velocity profile along the bed length, at the center of an x-z plane of the channel, for five different mesh sizes.....	61
Figure 4.10: Axial profile of the static pressure in the annular channel, for five different mesh sizes.....	62
Figure 4.11: Annular channel velocity profile along the bed length, at the center of x-z plane of the channel, for mesh sizes 18 and 15 mm.....	63
Figure 4.12: Center pipe velocity profile along the bed length, at the center of x-z plane of the channel, for five different mesh sizes.	64
Figure 4.13: Axial profile of the static pressure in the center pipe, for five different mesh sizes.	65
Figure 4.14: Radial pressure drop (the pressure difference between the center pipe and the annular channel) variation along bed length.	66
Figure 4.15: Typical flow distributions over the bed length in a radial flow reactor at the same feed flow rate for CP configurations (a-c) and for CF configurations (d-f). The arrow length represents the mass flow magnitude.	68
Figure 4.16: An illustration of the discharge and the collecting channels pressure profile that leads to a uniform flow distribution inside an RFBR.....	70
Figure 4.17: The axial static pressure profile in the annular channel and the center pipe of a CP-z RFBR.	75
Figure 4.18: CP-z type bed radial velocity profiles along the bed length, at x-z plane of the bed.....	77
Figure 4.19: CP-z type annular channel and center pipe velocity profiles, at the center of x-z plane of the channels.	78
Figure 4.20: A CP-z type axial velocity profile along the reactor radial direction at different axial levels.....	79
Figure 4.21: The axial static pressure profile in the annular channel and the center pipe of a CP- π RFBR.	81

Figure 4.22: CP- π type bed radial velocity profiles along the bed length, at x-z plane of the bed.....	82
Figure 4.23: CP- π type annular channel and center pipe velocity profiles, at the center of the x-z plane of the channels.	83
Figure 4.24: CP- π type axial velocity profile along the reactor radial direction.	84
Figure 4.25: The axial static pressure profile in the annular channel and the center pipe of a CF- π RFBR.	85
Figure 4.26: CF- π type bed radial velocity profiles along the bed length, in an x-z plane of the bed.	87
Figure 4.27: CF- π type annular channel and center pipe velocity profiles, at the center of an x-z plane of the channels.....	88
Figure 4.28: CF- π type axial velocity profile along the reactor radial direction.	89
Figure 4.29: The axial static pressure profile in the annular channel and the center pipe of a CF-z RFBR.	91
Figure 4.30: CF-z type bed radial velocity profiles along the bed length, at an x-z plane of the bed.	92
Figure 4.31: CF-z type annular channel and center pipe velocity profiles, at the center of an x-z plane of the channels.....	93
Figure 4.32: CF-z type axial velocity profile along the reactor radial direction.....	94
Figure 4.33: Radial pressure drop variations along the perforated section length of the bed.....	95
Figure 4.34: Deviation from uniform flow for the four radial flow configurations. ..	97
Figure 5.1: Heggs <i>et al.</i> (1995) multi-layered radial flow air filter, where 1, 2, 3, 4 and 5 are the bed layers. See Table 5.2 for details.....	100
Figure 5.2: Predicted center pipe pressure profile for Heggs <i>et al.</i> (1995) multi-layered radial flow air filter at a flow rate of 85 m ³ /h.....	103
Figure 5.3: Predicted annular channel pressure profile for Heggs <i>et al.</i> (1995) multi-layered radial flow air filter at a flow rate of 85 m ³ /h.....	104
Figure 5.4: A comparison of the profile of the normalized pressure in the center pipe.	106

Figure 5.5: A comparison of the profile of the normalized pressure in the annular channel.	107
Figure 5.6: Effects of the center pipe porosity on the flow distribution in a radial flow reactor.	112
Figure 5.7: Effects of setting the center pipe porosity lower than the porosity of the annular channel perforated plate on the flow distribution.	113
Figure 5.8: Effects of setting the center pipe porosity lower than the porosity of the annular channel perforated plate on the reactor radial pressure profile.	114
Figure 5.9: Effects of the bed porosity on the flow distribution in radial flow reactor.	116
Figure 5.10: CP- π radial velocity profiles at a clean center pipe.	120
Figure 5.11: CP- π radial velocity profiles with a low blockage of the center pipe top part.	121
Figure 5.12: CP- π radial velocity profiles with a severe blockage of the top section of the center pipe.	122
Figure 6.1: Effects of the side gas velocity on the solid movement and the formation of the cavity.	125
Figure 6.2: A schematic diagram of the RFMBR CFD model.	126
Figure 6.3: Magnified gas velocity vectors at the cross flow section.	128
Figure 6.4: Impact of the gas flow on the solid bed volume fraction.	129
Figure 6.5: Effects of the side gas velocity on the formation of the cavity in an RFMBR.	131
Figure 6.6: Catalyst volume fraction as function of gas velocity inlet, solid particle size and density are 1.25 mm and 1650 kg/m ³ respectively.	132
Figure 6.7: Effect of solid density on pinning phenomena, gas velocity is 10 m/s and solid particle size is 1.25 mm.	133
Figure 6.8: Effect of solid particle diameter on pinning phenomena, gas velocity is 10 m/s and solid particle density is 1650 kg/m ³	134
Figure 7.1 A schematic diagram of the radial flow moving bed experimental set-up used in the present study.	137
Figure 7.2: Cumulative mass percentage frequency curve using sieve analysis.	140

Figure 7.3: Effect of the gas flow rate on the pinning phenomena, using sago solid particles and 1/2 inch air inlet pipe.	145
Figure 7.4: Cavity wall profile as a function of the gas flow rate, using sago solid particles and 1/2 inch air inlet pipe.	147
Figure 7.5: Cavity initiation for 3/8 inch inlet pipe.	148
Figure 7.6: Total pinning for 3/8 inch inlet pipe.	149
Figure 7.7: Cavity initiation for 1/2 inch inlet pipe.	150
Figure 7.8: Total pinning for 1/2 inch inlet pipe.	151
Figure 7.9: Cavity initiation for 3/4 inch inlet pipe.	152
Figure 7.10: Cavity profile for 3/4 inch inlet pipe at maximum air flow rate.	153
Figure 7.11: Cavity initiation for a 1/2 inch inlet pipe with a flow distributor.	155
Figure 7.12: Cavity initiation for 1/2 inch inlet pipe with and without distributor, where (a) is for 1/2 inch without distributor and (b) is for 1/2 inch with distributor.	157
Figure 7.13: Cavity initiation for different solid materials.	160
Figure 7.14: Catalyst fluidization after cavity initiation and stopping the bed motion.	162

THESIS ABSTRACT

Name: AQEEL A. KAREERI
Title: INVESTIGATIONS OF THE FLOW AND PINNING PHENOMENA IN RADIAL FLOW REACTORS
Degree: MASTER OF SCIENCE
Major Field: CHEMICAL ENGINEERING
Date of Degree: DECEMBER 2004.

The flow in a radial flow fixed bed reactor (RFBR) was simulated using computational fluid dynamics (CFD). There are four types of RFBR based on the axial directions of the flow in the distributing channel and center pipe and on the reactor radial flow direction. These types are known as CP-z, CP- π , CF-z and CF- π configurations. The flow in all four configurations was simulated. The model results showed good agreement with published experimental data. Results also showed that the present rigorous model can approximate the experimental results better than previously proposed analytical and numerical models. Results also showed that the π -flow configurations have always the most uniform axial flow compared to the z-flow configurations under the same conditions. Results also showed that for a ratio of the cross sectional area of the center pipe to that of the annular channel, less than one, the CF- π configuration gives the most uniform flow. For an area ratio larger than one, the CP- π configuration gives the best uniform flow. Results also showed that the

uniformity of the flow distribution is enhanced by lowering the porosity of the center pipe and that of the bed.

Experimental studies of flow in a radial flow moving bed reactor (RFMBR) were carried out. In this type of reactor, there is an upper limit of the gas flow rate imposed by a mechanical phenomenon called “pinning”. “Pinning” is when the catalyst particles are pinned against the center pipe due to high gas velocity. In this work experimental investigations of the hydrodynamics of a moving bed reactor were carried out. Experiments were carried out using four different solids. A range of size, density, and sphericity was used. It was found that pinning is a function of the intensity of the gas inlet jet and the geometry of the inlet chamber. A diffused rather than a jet inlet was found to allow a larger gas rate to be used without experiencing pinning. The size and density of the solid particles were found to influence the pinning phenomenon. The larger the size and/or the density, the better it is to resist pinning.

Results obtained using CFD simulation of a radial flow moving bed reactor confirmed many of the industrial findings especially the effect of gas flow rate on pinning.

ARABIC ABSTRACT

ملخص الرسالة

عقيل أحمد كيرى	الاسم:
بحوث للسريان وظاهرة تعليق جسيمات المحفز في مفاعل شعاعي	العنوان:
الماجستير	الدرجة:
هندسة كيميائية	التخصص:
ذوالقعدة 1425 هـ	التاريخ:

في كثير من المفاعلات الكيميائية ينخفض أداء المحفزات بسرعة كبيرة ولكن من الممكن إعادة فاعليتها. هذه العملية من الممكن تنفيذها في مفاعل شعاعي متحرك. عمليات إعادة الفاعلية للمحفزات في هذه الحالات تتم بشكل مستمر في مفاعل حيث يكون المحفز متحركاً نحو الأسفل بينما يتحرك الغاز في الإتجاه الشعاعي للمفاعل ويغادر من خلال الانبوب المركزي.

في مثل هذه المفاعلات يوجد حد أعلى لكمية الغاز الممكن ضخه في المفاعل لتقادي ظاهرة تعليق جسيمات المحفز إلى جدار المفاعل.

لقد تمت محاكاة السريان في مفاعل شعاعي ثابت. وتمت محاكاة جميع أنواع هذه المفاعلات الأربعة. هذه الأنواع هي $CF-\pi$, $CF-Z$, $CP-Z$, $CP-\pi$. أظهرت نتائج الدراسة تطابقاً جيداً مع نتائج معملية منشورة سابقاً وأظهرت النتائج أيضاً أن النمذجة الحالية تتطابق مع النتائج المعملية أفضل من النماذج العددية المنشورة سابقاً.

وأظهرت النتائج أن نوع π يحتوي على سريان أكثر تناسقاً مقارنة مع نوع Z . وأظهرت النتائج أيضاً أنه إذا كانت نسبة مساحة الانبوب المركزي إلى مساحة ألمجرى الحلقي أقل من 1 فإن السريان في نوع $CF-\pi$ يكون الأكثر تناسقاً. أما إذا كانت النسبة أكبر من 1 فإن السريان في نوع $CP-\pi$ يكون الأكثر تناسقاً.

ولقد تمت دراسة السريان في مفاعل شعاعي متحرك بواسطة تجارب معملية. هدفت الدراسة إلى فهم العوامل المؤثرة في ظاهرة تثبيت المحفزات على سطح الأنبوب المركزي

إذا كانت سرعة الغاز مرتفعة جداً. أظهرت النتائج أن العوامل المؤثرة في تحديد كيفية وتوقيت حصول التثبيت هي سرعة الغاز وشكل النافث بالإضافة إلى حجم وكثافة حبيبات الحفاز. كلما أزداد حجم وكثافة المحفزات كلما ازدادت كمية أو سرعة الغاز الممكن إستعمالها دون أن تثبت المحفزات.

وفي هذه الدراسة أيضاً تمت محاكاة السريان في مفاعل شعاعي متحرك وأظهرت النتائج تطابقاً نوعياً مع النتائج المعملية.

CHAPTER 1

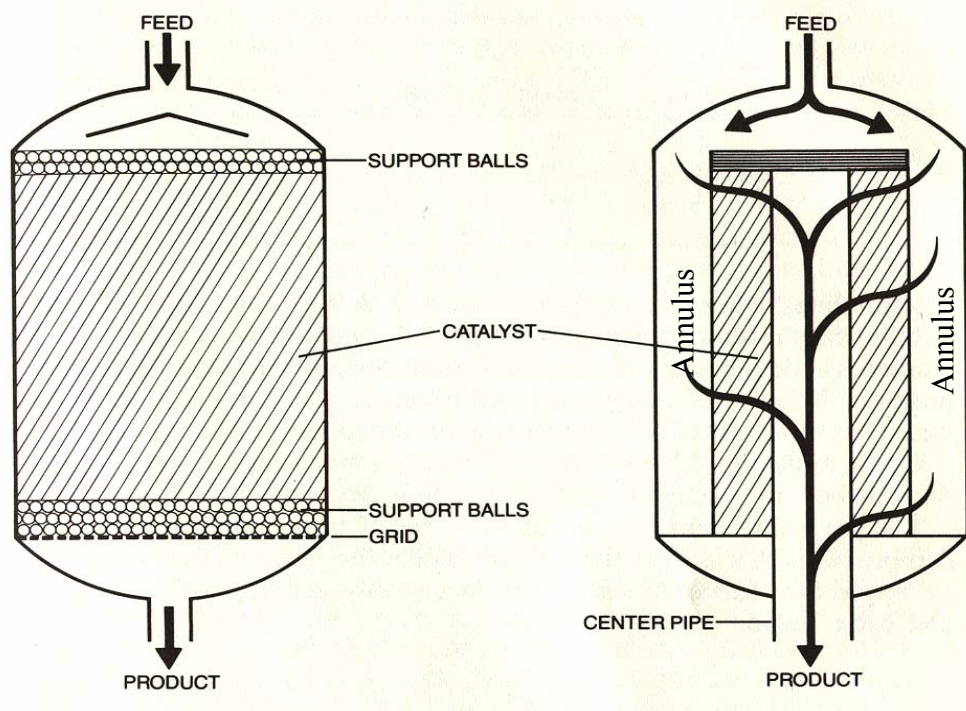
INTRODUCTION

1.1 Packed Bed Reactor

Numerous adsorption and catalytic processes are carried out in packed bed reactors. Packed bed reactors are classified into two types depending on the flow direction through the reactor. They are axial flow and radial flow reactors. Figure 1.1 illustrates these types of reactors. In an axial flow reactor, the feed enters at the top and flows axially through the catalyst bed. The product exits at the bottom. In a radial flow reactor, the feed enters at the top and the product exits at the bottom, however, the feed flows radially across the catalyst bed. The radial flow reactors provide larger mean cross-sectional area and reduce distance of travel for flow compared to axial flow reactors. The main advantages of radial flow in comparison with axial flow reactors are the low pressure drop and the high flow capacity. Due to these advantages many of the packed bed reactors have been designed with radial flow type in order to process higher feed rates.

1.2 Radial Flow Reactor

A radial flow reactor, shown in Figure 1.2, is a cylindrical vessel with especially designed internals. The main internals that provide the radial flow pattern inside the reactor are the inlet distributing header in the form of perforated channels positioned around the circumference of the vessel, and the axial outlet collecting header in the



Axial Flow Reactor

Radial Flow Reactor

Figure 1.1: An axial flow and a radial flow reactors.

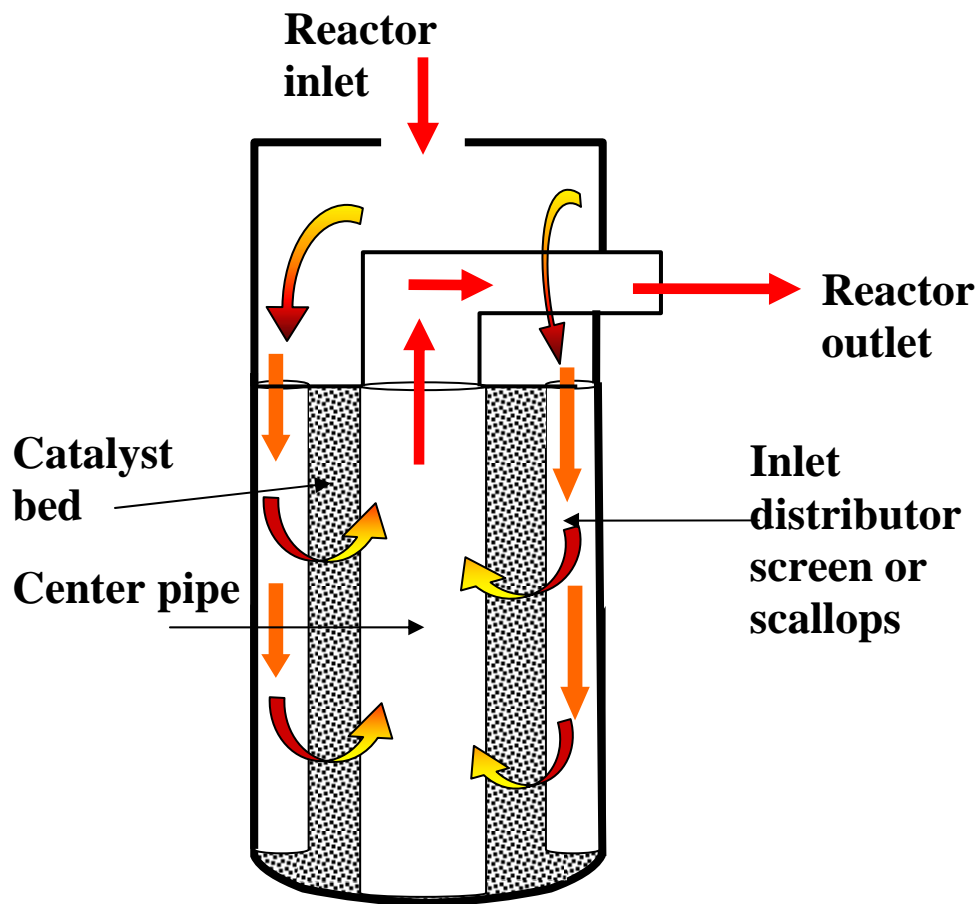


Figure 1.2: A radial flow fixed bed reactor (RFBR).

form of a perforated cylinder which is called the center pipe. The catalyst is charged to the space between the side channels and the center pipe. The top of the catalyst bed is covered with a cover plate. There are two types of inlet distributors. One is a wire screen and the other is called scallops (Little, 1985). Each scallop is a small diameter perforated half cylinder.

There are two types of radial flow reactors depending on the catalyst bed situation inside the reactor. They are the radial flow fixed bed reactor (RFBR) and the radial flow moving bed reactor (RFMBR). In the RFBR shown in Figure 1.2 the catalyst bed is stagnant inside the reactor. In the RFMBR shown in Figure 1.3 the catalyst bed moves inside the reactor.

1.2.1 A Radial Flow Moving Bed Reactor (RFMBR)

Another advantage of the radial flow reactor is that it can be designed to allow the catalyst movement inside the reactor. In a process where the catalyst is deactivated rapidly due to coke formation, an RFMBR can be used to allow regeneration of the catalyst and returning it back to the reactor without shutting down the process as in a fixed bed reactor process. An RFMBR can be used for catalytic cracking, adsorption, and granular filtration processes (Marb and Vortmeyer, 1988; Tsubaki and Tien, 1987). The well known processes using RFMBR are the IFP and the UOP continuous catalyst regeneration (CCR) reformer.

In an RFMBR, the catalyst moves vertically downwards through the reactor by gravity, while the reacting gas flows horizontally across the bed towards the center pipe. The catalyst flow rate in a moving bed reactor is very low compared to a fluidized reactor.

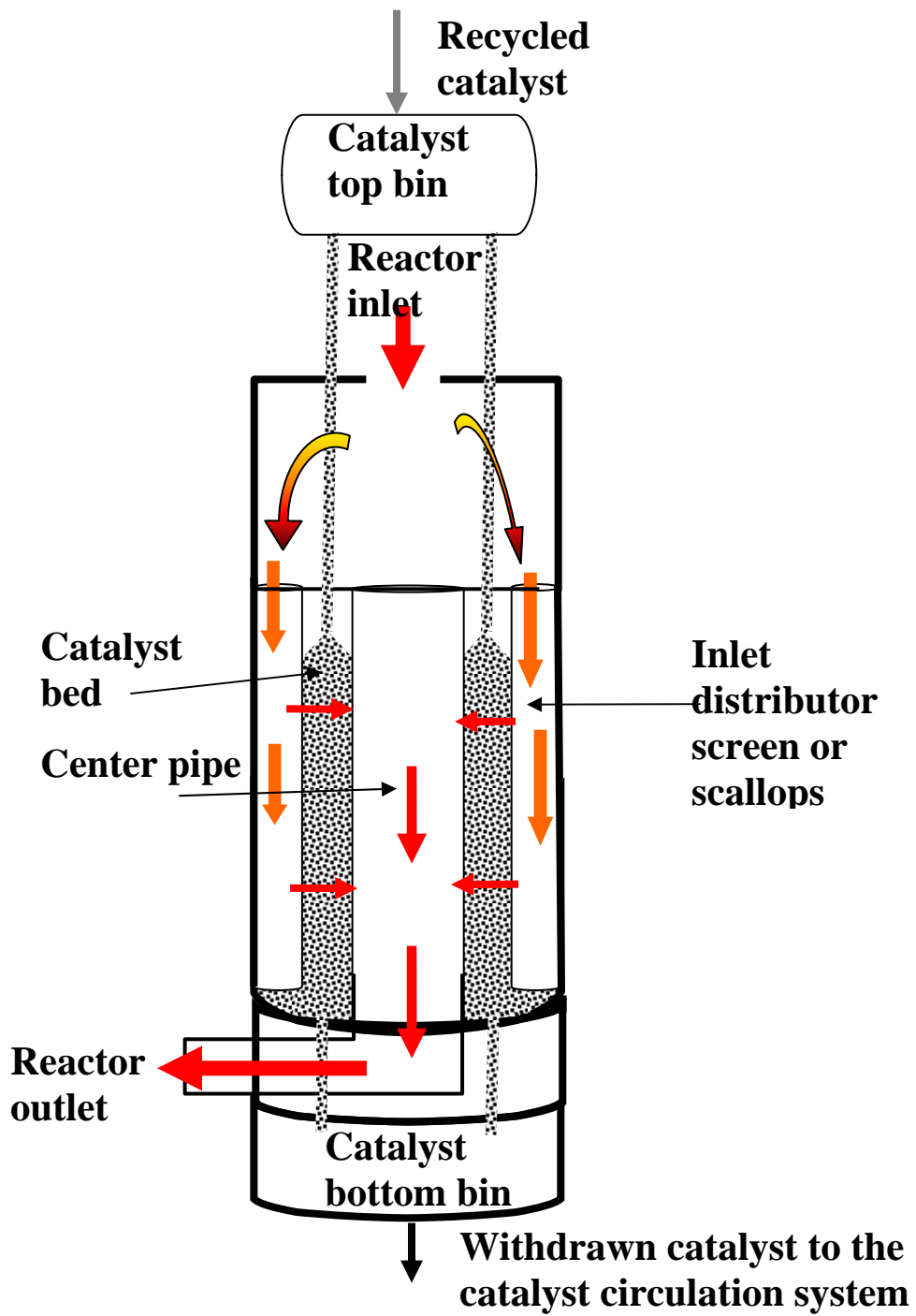


Figure 1.3: A radial flow moving bed reactor (RFMBR).

The catalyst flow in a fluidized catalytic cracking FCC unit is measured in tons per hour, while in CCR reformer it is measured in a few hundred or a few thousand pounds per hour (Little, 1985). The catalyst velocity is of the order of a few millimeter per second.

Many of the new catalytic processes are designed with a radial flow reactor type. This is because it can allow the processing of high feed rates with less reactor pressure drop and it also allow the regeneration the catalyst without shutting down the whole process. Despite its advantages, a radial flow reactor suffers from two problems. The first one is the poor flow distribution inside the reactor. The second one is the pinning phenomena. The poor flow distribution can occur in an RFBR or an RFMBR. The pinning phenomena, which is described in the next section is limited to an RFMBR.

1.2.2 Pinning

Gravity is the driving force for the solid particles movement through the RFMBR. Pressure is the driving force for the gas flow from the distributor header to the center pipe. When the pressure gradient along the gas flow direction is sufficiently large, it will cause a holdup of solid particles against the center pipe. At this stage the drag force exerted by the gas stream is greater than the gravitational force on the solid and hence the action of gravity is not enough to cause the solid particle to move down. A portion of, or the whole solid bed can be pinned depending on the magnitude of the pressure drop across the reactor (Pilcher and Bridgwater, 1990). Figure 1.4 illustrates some forms of the catalyst bed movement inside an RFMBR.

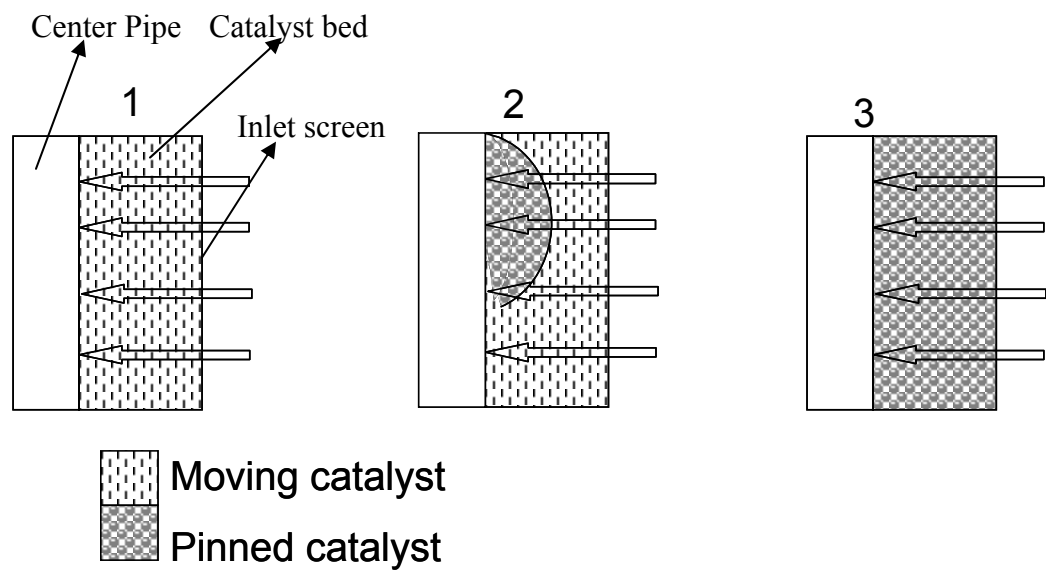


Figure 1.4: Forms of the catalyst bed movement: (1) Totally moving bed, (2) Partially pinned bed, (3) Totally pinned bed.

The main cause of pinning is the high gas flow rate to the reactor. If pinning occurs, it will cause maldistribution inside the reactor which will lead to low reactor performance. In any CCR process, pinning is a major concern, because the pinned catalyst can become highly coked and may then flow to the regeneration system. The highly coked catalyst may contain coke higher than the design limitation for the regeneration system. If the highly coked catalyst burns in the regeneration system it will cause equipment damage. Due to that pinning is the first limitation to be evaluated before increasing the feed rate above the design value for the CCR process.

In this research the radial flow reactor flow distribution and pinning phenomena are investigated using computational fluid dynamics (CFD).

1.3 Computational Fluid Dynamics CFD

Computational Fluid Dynamics (CFD) analyses systems involving fluid flow, heat transfer and associated phenomena such as chemical reactions, by means of a computer-based simulation. The technique is very powerful and spans a wide range of industrial and non-industrial areas of application e.g.; aerodynamics of aircraft and vehicles, combustion in internal combustion (IC) engines and gas turbines, cooling of equipment including micro circuits, chemical engineering processes including mixing, separation and polymer molding, heating/ventilation, environment engineering, blood flows through arteries and veins (Versteeg and Malalasekera, 1995).

The use of CFD to predict internal and external flows increased dramatically in the past decade, due to availability of high performance computing hardware together with efficient solution algorithms. CFD is increasingly becoming a vital

component in the design of industrial products and processes. Some of the unique advantages of CFD over experiment based approaches to fluid systems design includes:

- Substantial reduction of lead times and costs of new designs.
- Ability to study systems where controlled experiments are difficult or impossible to perform (e.g. very large systems).
- Ability to study systems under hazardous conditions at and beyond their performance limits (e.g. safety studies and accident scenarios).
- Practically unlimited level of detail of results. Full values of fields of velocity, pressure and all solved for variables are available.

However, there are no sure guarantees for the accuracy of a simulation, so results of CFD models need to be validated. CFD gives a better insight into the fluid flow phenomena. A numerical solution is never 100% accurate but with sufficient mesh refinement the accuracy of the results is likely to become adequate. Experimental data of similar scope should be generated. Sometimes facilities to perform experimental work may not exist. So one has to rely on (i) previous experience (ii) comparisons with analytical solutions of similar but simpler flows and (iii) comparisons with high quality data from closely related problems reported in the literature.

Currently the CFD market is dominated by a number of codes namely, FLUENT, PHOENICS, CFX, FEMLAB and STAR-CD. These are based on a finite volume method. In this study FLUENT 6.1.22 is used. All packages contain three main elements: (i) a pre-processor, (ii) a solver and (iii) a post-processor. A brief

description of functions of each of these elements within the context of a CFD code is given here.

Pre-Processor

The user activities at the pre-processing stage involve:

- Definition of the geometry of the region of interest: the computational domain.
- Grid generation - the sub-division of the domain into a number of smaller, non-overlapping sub-domains: a grid (or mesh) of cells (or control volumes or elements).
- Selection of the physical and chemical phenomena that need to be modeled.
- Definition of fluid properties.
- Specification of appropriate boundary conditions at cells which coincide with or touch the domain boundary.

The solution to a flow problem (velocity, pressure, temperature etc.) is defined at nodes inside each cell. The accuracy of a CFD solution is governed by the number of cells in the grid. In general the larger the number of cells the better the solution accuracy. Optimal meshes are often non-uniform. These meshes are finer in areas where large variations occur from point to point and are coarser in regions with relatively little change. FLUENT has the capability of adaptive meshing.

Solver

There are three distinct streams of numerical solution techniques: finite difference, finite element and spectral methods. Finite volume method is an example of spectral

methods. In brief, the numerical methods that form the basis of the solver perform the following steps:

- Approximation of the unknown flow variables by means of simple functions.
- Discretisation by substitution of the approximations into the governing flow equations and subsequent mathematical manipulations.
- Solution of the algebraic equations.

The main differences among the three separate streams are associated with the way in which the flow variables are approximated and with the discretization processes.

Post-Processor

Like pre-processing, a huge amount of development work has recently taken place in the post-processing field. Owing to the increased popularity of engineering workstations, many of which have outstanding graphics capabilities, the leading CFD packages are now equipped with versatile data visualization tools.

CHAPTER 2

LITERATURE REVIEW

2.1 Radial Flow Fixed Bed Reactors (RFBR)

The radial flow fixed bed reactor was originally used in the catalytic synthesis of ammonia. Since then, it has been used for catalytic reforming, desulphurization, and nitric oxide conversion. Earlier analytical work on RFBRs concentrated on the effects of radial flow direction on reaction conversion with the assumption of perfect radial flow profile inside the reactor.

Radial flow reactors can be classified into a z-flow type or a π -flow type depending on the axial directions of the flow in the distributing channel and center pipe. Moreover, radial flow reactor can be also classified into centripetal (CP) or centrifugal (CF) flow types depending on the reactor radial flow direction. In the CP-flow type, the gas is fed to the distributing channel and travels radially from the outer screen to the center pipe. In the CF-flow configuration the gas is fed to the center pipe and travels radially from the center pipe to the outer screen. Therefore, four flow configurations are possible for a radial flow reactor. They are classified as CP-z, CP- π , CF-z and CF- π configurations as shown in Figure 2.1.

The first published analysis of an RFBR was for ammonia synthesis reactor in 1968 by Raskin (Chang and Calo, 1981). Earlier works performed by Hlavacek and Kubicek (1972) and Calo (1978), have shown that at a perfect radial flow distribution the direction of radial flow (CP or CF) has an effect on the reaction conversion.

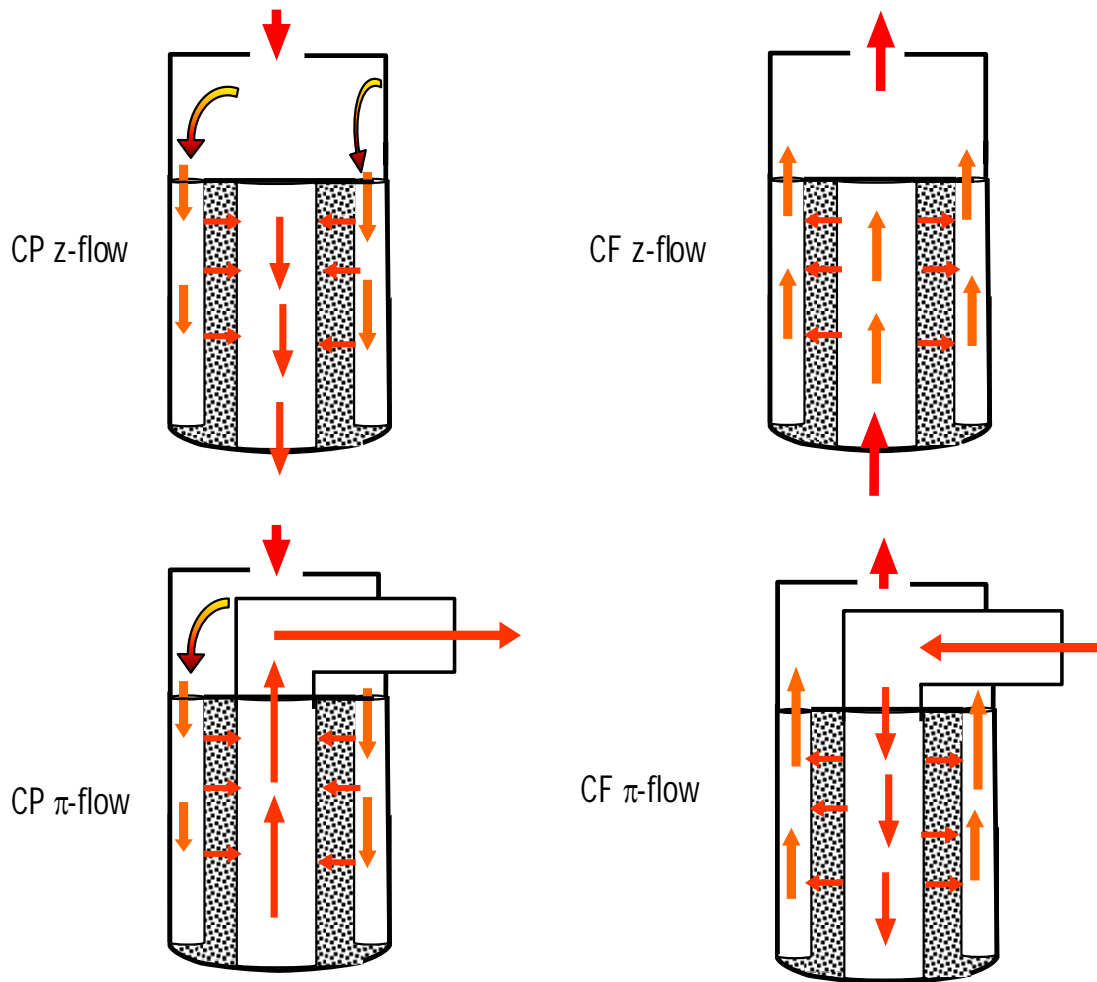


Figure 2.1: The four possible flow configurations for an RFBR.

This effect is due to the chemical reaction mechanism (Chang and Calo, 1981). Genkin *et al.* (1973) performed theoretical and experimental investigations to determine the flow distribution inside CF-z and CF- π radial reactor types. A significant maldistribution was reported. The gas distribution inside the reactor was found to be a function of the center pipe porosity and the ratio of the cross-sectional area of the center pipe to that of the annular channel.

Ponzi and Kaye (1979) performed analytical investigations to determine the effects of radial flow maldistribution and flow direction on the reactor performance. They were the first to show that a maldistribution in the radial flow profile inside the reactor has more influence on the reactor performance than the flow direction.

Chang and Calo (1981) also performed analytical investigations to determine the effects of radial flow maldistribution and flow direction. They studied all four reactor configurations shown in Figure 2.1. Chang and Calo (1981) concluded that the optimum flow profile in an RFBR can be achieved by adjusting the reactor dimensions so that the radial pressure drop remains independent of the axial coordinate.

Chang *et al.* (1983) established a design criterion to achieve optimum flow profile in an RFBR. They used asymptotic methods to obtain analytical solutions of RFBR previous models. They used the independency of the radial pressure drop of the axial coordinate as the base to determine the design criterion. They investigated the CP and CF π -flow configurations only, because the opposed flow configuration of π -flow maintains the independency of the radial pressure drop of the axial coordinate.

The established design criterion is limited for small values of reactor parameters such as center pipe diameter and catalyst bed thickness.

An operating test on an RFBR in three commercial reforming units to investigate the axial flow distribution was performed by Lobanov and Skipin (1987). All the reactors were CP z-flow type. It was concluded from that work that a relatively uniform flow distribution existed only at the lower part of the catalyst bed. However a significant amount of the upper part of the catalyst bed was not fully utilized. Such a scenario can be well explained by the findings of the present study.

Low utilization of the upper part of the catalyst bed reduces the reactor performance. Based on previous investigations of RFBR, Lobanov and Skipin (1987) suggested changing the flow direction from CP to CF to eliminate this phenomenon. Another method to eliminate this phenomenon is to minimize the bed porosity by using tight packing of the catalyst. This method was described by Nooy (1984).

Song *et al.* (1993) performed theoretical and experimental investigations of the axial flow distribution in an RFBR without reaction. Their study was applied for all four reactor configurations shown in Figure 2.1. The ratio of the cross-sectional area of the center pipe to that of the annular channel was less than one. It was found that the CF π -flow configuration has the most uniform axial flow over the other configurations at the same conditions.

Heggs *et al.* (1994) performed a numerical investigation for all four configurations. The ratio of the cross-sectional area of the center pipe to that of the annular channel was greater than one. It was concluded that the CP π flow configuration gives the best flow distribution. Heggs *et al.* (1995) extended their

previous model to predict the flow profiles for a multi-layered radial flow air filter. A good agreement was found between the model predictions and the experimental results.

Bolton *et al.* (2002) performed CFD and experimental evaluation to determine the flow distribution in an RFBR of novel design. The objectives of that study were to illustrate the use of an electrical tomography technique for flow visualization and to confirm CFD predictions. The velocity profiles by CFD and a tomography method showed qualitative agreement.

Mu *et al.* (2003) developed a two-dimensional hydrodynamic mathematical model for a CP- π configuration RFMBR. In the model the bed was considered as a stationary bed. The model predictions were validated against published experimental results for an RFMBR. A good agreement was found which indicates a similarity of the gas flow profiles of an RFBR and an RFMBR. This is because the catalyst velocity in an RFMBR is very small, usually less than 1 mm/s. At such a low velocity, the bed porosity of an RFBR is almost the same as that of an RFMBR. This similarity of the gas flow profiles of an RFBR and an RFMBR was proved by the experimental work of Song *et al.* (1994). However this similarity will cease to exist if the pinning phenomena is initiated in an RFMBR (Song *et al.*, 1994).

2.2 Radial Flow Moving Bed Reactors RFMBR

A radial flow moving bed reactor is a class of moving bed cross flow configurations. In such a configuration, the pinning phenomena can occur. There are only a few papers available on moving beds cross flow. The first apparent mention of pinning

phenomena in the open literature is the brief discussion by Bridgwater in 1981 and Ginestra and Jackson (1985).

Ginestra and Jackson (1985) performed a preliminary experimental and theoretical investigation of pinning in a system with simplified rectangular geometry. They selected the rectangular geometry because it would exhibit the essentials of the pinning phenomena and is more accessible to observation than the realistic cylindrical configuration. The two-dimensional simple diagram of the geometry is in Figure 2.2. Ginestra and Jackson (1985) established the theory of the cavity growth which is described in the next paragraph and based on it they devolved a theoretical description of the pinning phenomena and compared it with the experimental observation.

For simplicity, the stream lines of air flow were assumed to be straight lines normal to the porous faces as in Figure 2.2. As the pressure drop Δp increases, the drag force exerted on the particles by air causes the normal stress N_1 between the particles and the upstream porous face to decrease with a corresponding increase in the normal stress N_2 at the downstream porous face. As Δp is increased to Δp_0 at which N_1 is reduced to zero, a thin cavity, free of solid material, would be expected to open between the particle bed and the upstream face. At this point some of the particles near the downstream face may not move due to the increase in N_2 . At a further increase in Δp to Δp_1 , the cavity adjacent to the upstream face might be increased until it ultimately spans the full width of the catalyst bed. At this point the bed may not move down and the bed will be said to be completely pinned.

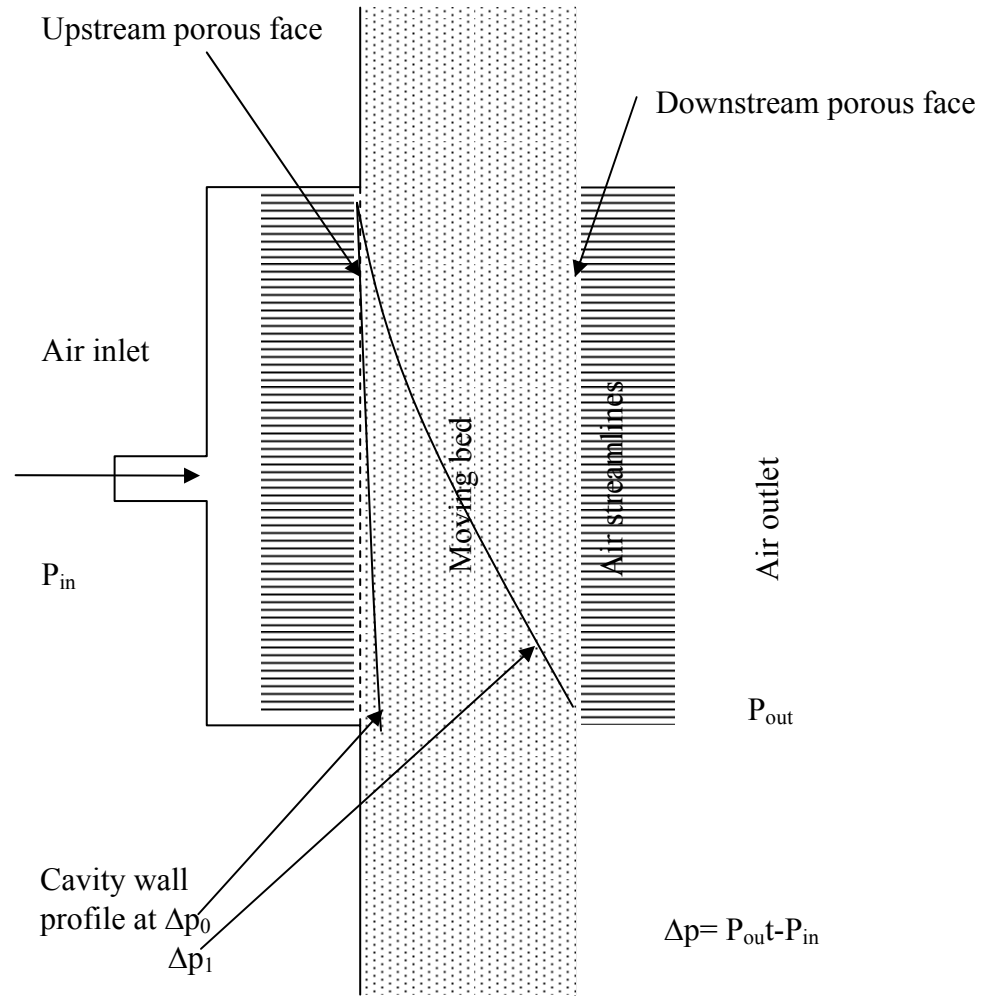


Figure 2.2: A schematic diagram of the geometry used by Ginestra and Jackson (1985).

Figure 2.2 shows the cavity wall profiles at the cavity initiation Δp_0 and at the complete pinning Δp_1 . Based on the process of cavity growth and the force balance on the bed with assuming that the flow is one-dimensional radial flow, Ginestra and Jackson (1985) developed theoretical analysis to predict Δp_0 required for the cavity initiation, Δp_1 for the complete pinning, and the cavity wall profile between Δp_0 and Δp_1 . Between cavity initiation and complete pinning, partial pinning may exist. This theory is not capable to quantitatively predict the partial pinning.

It is not significant to quantify whatever occurs after the cavity initiation. Cavity initiation is the main concern for operating the RFMBR, because when it occurs it will cause flow maldistribution and low reactor performance. In addition to that, partial pinning should be always avoided even for a small amount of particles, especially if the particles are sent to a continuous regeneration system. Because pinned particles may contain high coke ranging between 10-30 wt%, depending on the pinning time. If they become free to move to the regeneration system which is normally designed for a maximum of 7 wt%, they may burn and consequently damage the regeneration equipment.

An RFMBR is normally operated at a certain margin above the cavity initiation. Quantifying the cavity initiation will help in making the RFMBR operation to be neither conservative nor risky.

Ginestra and Jackson (1985) conducted an experimental study for the same rectangular geometry to validate the theoretical analysis. The cavity growth process was qualitatively similar to that predicted theoretically. Figure 2.3 shows the theoretical and the experimental cavity growth process. In the experimental study,

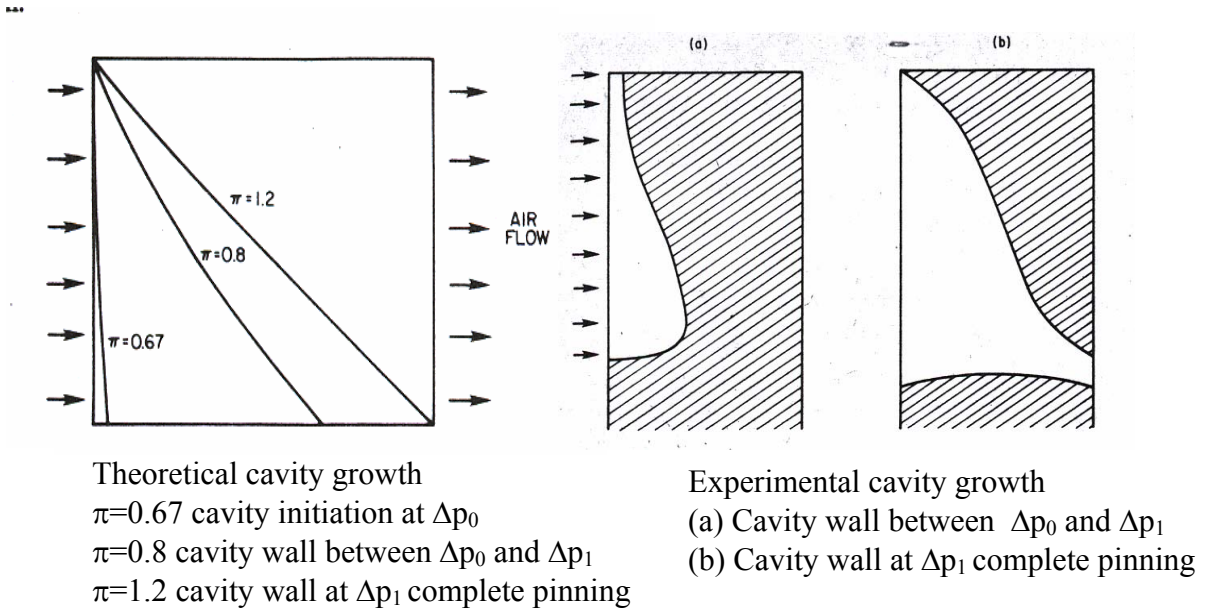


Figure 2.3: Theoretical and experimental cavity wall profiles by Ginestra and Jackson (1985), where π is a dimensionless pressure drop factor.

cavity growth process was observed by photographing through a transparent wall of the bed. They observed good agreement between the theoretical and experimental cavity wall profiles at complete pinning.

Doyle *et al.* (1986) generalized the cavity growth theory by Ginestra and Jackson (1985) to theoretically describe the pinning phenomena in a simple RFMBR configuration which is shown in Figure 2.4. The reactor is z-flow type. They applied the theoretical analysis to CP and CF z-flow configurations.

It was found that the CP flow type is preferable, since a large gas flow can be achieved before pinning. They performed an experimental study for the same geometry and the results were in good qualitative agreement. Doyle *et al.* (1986) concluded that the CP flow type can sustain more pressure drop before pinning than the CF flow type.

Although the geometries used by Ginestra and Jackson (1985) and Doyle *et al.* (1986) are simple, they give a good idea of the pinning mechanics. Both works are based on the cavity growth which initiates first at the upstream porous and then propagates to the downstream porous face as the pressure drop increases. The cavity growth theory that was used by Ginestra and Jackson (1985) and Doyle *et al.* (1986) may be applicable for a bed with small thickness and uniform flow distribution. However for large bed and not completely uniform flow the situation will be different. The cavity may initiate within the bed particles depending on the location of the highest drag force exerted by the gas. Therefore it may be better to solve the flow profile inside an RFMBR simultaneously with a pinning model.

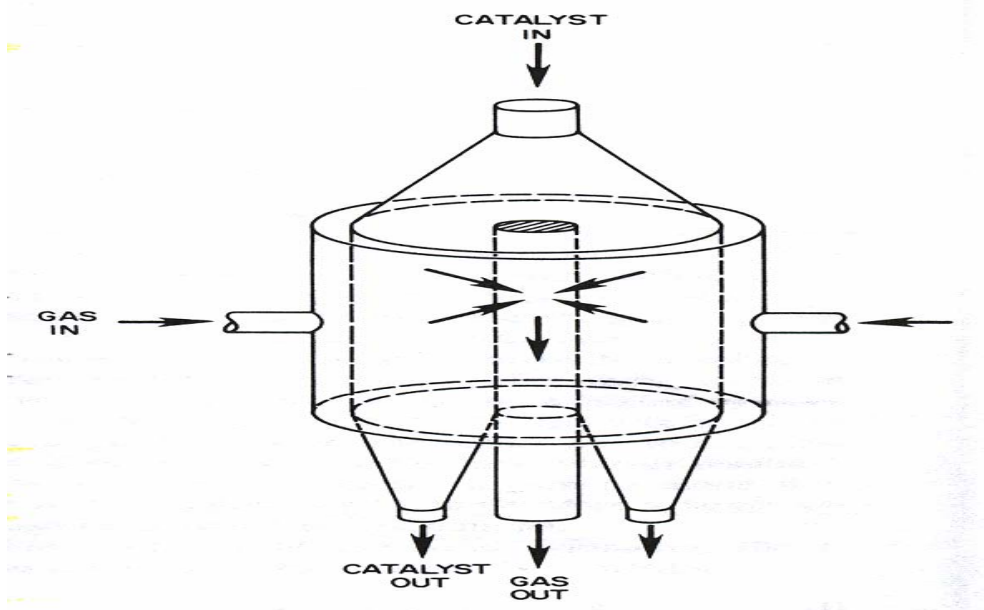


Figure 2.4: The RFMBR used by Doyle *et al.* (1986).

Tsubaki and Tien (1987) performed analytical study for solid movement in cross flow moving bed filters similar to the configuration in Figure 2.2. The analysis was done by obtaining the stress distribution throughout the solid phase. It was found that the solid velocity profile depends on the gas pressure drop and the frictional stress between the particles and between the particle and the surface of the filters. The results were found to agree reasonably well with available experimental data.

Pilcher and Bridwater (1990) experimentally studied the pinning in a rectangular moving bed reactor similar to the configuration in Figure 2.2. They investigated the effects of the shape and the size of the solid particles and the distance separating the upstream and downstream porous faces. They observed the same cavity growth process that was observed by Ginestra and Jackson (1985) and Doyle *et al.* (1986). Pilcher and Bridwater (1990) experimental set-up was more advanced than that of Ginestra and Jackson (1985) and Doyle *et al.* (1986). This allowed them to record the cavity initiation and the partial pinning, see Figure 1.4 (2), where the cavity encompasses a part of the bed width and not all of it.

It was concluded from that study that the pressure drop required for the cavity initiation is independent of the equipment size. This conclusion contradicts Ginestra *et al.* (1985) and Doyle *et al.* (1986) theoretical analysis. Also it was concluded that the cavity initiation, cavity wall profile and complete pinning depend on the shape and the size of the solid particles.

Song *et al.* (1993) performed an experimental study of the effects of the gas flow rate on an RFMBR operation. They found that at high gas flow rate, the drag

force exerted on the particles enhances friction between the particles and the downstream wall which is sufficient to prevent bed motion.

Song *et al.* (1994) performed theoretical and experimental study for pinning phenomena in an RFMBR. Good agreement was found between the theoretical and experimental results. Experimental results of the bed pressure drop for the fixed bed and moving bed modes indicates the similarity of the flow profiles of RFBR and RFMBR prior the initiation of the pinning phenomena. The pinning phenomena was also found to be a function of reactor geometry.

2.3 Reforming Moving Bed Reactors

There is little information in the open literature about the pinning phenomena in the reforming reactor. Vora and Scott (1989) proposed a procedure to immobilize the pinning that may exist in the first reactor. The procedure is applicable for a reactor system with separate hydrogen feed to each reactor. The procedure is as follow:

- Reduce the first reactor temperature which will lower the hydrocarbon conversion.
- Reduce the hydrogen feed to the first reactor until unpinning the catalyst.
- Increase the catalyst circulation rate.
- Increase the second reactor hydrogen feed.
- Increase the second reactor temperature to restore the hydrocarbon conversion that was lowered for the first step.

Jinfu *et al.* (1997) performed an analytical study for the gas distribution in a moving bed reforming reactor. Their study explored the influence of the reactor

structure parameter and the operating conditions on the uniformity of the gas distribution in the reforming reactor.

Gautam *et al.* (1999) proposed R-160 series catalyst for the reforming units which are limited in capacity by pinning but not by the regeneration capacity. These catalysts have higher density which gives greater resistance against pinning.

2.4 Summary of Literature Review

The survey of literature shows that the previous analytical and numerical models of flow in an RFBR are limited and rather simplified. None of these models was full three-dimensional and none of them took the change in the flow area of the fixed bed as the flow moves towards the center pipe or away from it. The literature survey also showed that no full three-dimensional CFD model of flow in an RFBR has yet been reported. In this study, such a 3-D CFD model is reported.

2.5 Objectives of the Current Study

From the previous work, it is shown that flow distribution has a major effect on the operations of an RFBR and an RFMBR. The objectives of this work are to:

- Carry out a detailed CFD investigation of an RFBR.
- Validate the CFD model of an RFBR against some published data.
- Use the flow distribution results of an RFBR to get insights into the pinning phenomena.
- Perform parametric runs to show the impact of important factors on the operation of an RFBR. These factors include center pipe porosity,

bed void fraction and ratio of center pipe cross sectional area to that of the annular channel.

- Simulate an RFMBR to study pinning phenomena.
- Validate the results of an RFMBR against some published data.
- Construct experimental set-up to study pinning phenomena.
- Perform experimental study of pinning phenomena using different inlet configurations and different solid.

CHAPTER 3

MATHEMATICAL FORMULATION

3.1 Radial Flow Fixed Bed Reactors RFBR

The flow in an RFBR reactor is classified as a single phase flow. Simulation of an RFBR is carried out under no reaction, incompressible, isothermal and steady state conditions. These assumptions are the same as those used in Mu *et al.* (2003) model which was used to design commercial reactors. The governing equations for the gas flow in an RFBR are the mass and momentum conservation equations.

The conservation of mass (continuity equation) equation can be written as:

$$\nabla \cdot \vec{v} = 0 \quad (3-1)$$

The conservation of momentum equation is:

$$\rho(\vec{v} \cdot \nabla \vec{v}) = -\nabla p + \mu \nabla^2 \vec{v} + \rho \vec{g} + \vec{S} \quad (3-2)$$

where v is the velocity, ρ is the density, p is the pressure, μ is the viscosity and g is acceleration due to gravity. The term S contains other model-dependent source terms. In this work two models are used porous-media and porous-jump. The porous-media model is used for the catalyst bed and the porous-jump model is used for the center pipe and annulus perforated plates.

At the catalyst bed S can be written as:

$$\vec{S} = -\left(\frac{\mu}{\delta} v + C_2 \frac{1}{2} \rho |v| v\right) \quad (3-3)$$

where δ is the permeability and C_2 is the inertial resistance factor. From the Ergun equation, which is a semi-empirical correlation applicable over a wide range of Reynolds numbers and for many types of packing, δ and C_2 can be represented by:

$$\delta = \frac{d_p^2}{150} \frac{\varepsilon^3}{(1-\varepsilon)^2} \quad (3.4)$$

$$C_2 = \frac{3.5}{d_p} \frac{(1-\varepsilon)}{\varepsilon^3} \quad (3.5)$$

where ε is the bed porosity and d_p is the catalyst particle average diameter. In this model the bed porosity and catalyst diameter were assumed to be 0.35 and 1.8 mm, respectively.

The porous-jump is a simplification of the porous media model where the flow is assumed to be one dimensional, perpendicular to the porous section of the plate. Since the velocity is high through the perforated plate the inertial term is the dominating one. Due to the high velocity, the permeability term can be neglected, and the source term at the center pipe and annular perforated plates becomes:

$$S = -\left(C_2 \frac{1}{2} \rho |v_i| v_i \right) \quad (3.6)$$

where i is the normal coordinate (x, y or z) to the perforated plate. C_2 for the perforated plate is determined from the equation of flow through square-edged holes on an equilateral triangular spacing.

$$C_2 = \frac{1}{C^2} \frac{(A_p / A_f)^2 - 1}{thick} \quad (3.7)$$

where C is the orifice discharge coefficient. In this work C is 0.62. This value is generally used for most of the perforated plates (Perry and Green, 1997). A_p is the

total area of the plate and A_f is free area or total area of the holes. *thick* is the plate thickness.

Initial Conditions

Prior to the start of iteratively solving the equations, the velocity and pressure values throughout the computational domain are arbitrarily set. In this case the initial velocity was 0 m/s and the initial gauge pressure was 0 Pa.

Boundary Conditions

- **Reactor inlet:** A uniform inlet velocity condition is used. It equals the inlet flow rate divided by the cross sectional area of the reactor inlet.
- **Reactor outlet:** An outflow boundary condition is used. The outflow velocity and pressure are updated in a manner that is consistent with a fully-developed flow assumption.
- **Reactor walls:** A no-slip condition is used.
- **Reactor bed:** A porous media condition is used. Knowing ε and d_p , bed resistances are calculated from Equations 3.4 and 3.5.
- **Reactor perforated plates:** A porous-jump condition is used. Knowing the plate porosity, the plate resistance is calculated from Equation 3.7

3.2 Radial Flow Moving Bed Reactors (RFMBR)

A moving bed reactor is a two-phase reactor. To model this reactor a multiphase model is required. In general there are two modeling approaches for multiphase flows: the Eulerian multiphase model and the Lagrangian multiphase model. The

Eulerian model is applicable when the dispersed second phase occupies a high volume fraction and the Lagrangian model is applicable when the dispersed second phase occupies a low volume fraction. Since the catalyst (solid phase) occupies a high volume fraction of the moving bed reactor the Eulerian model will be used in this work.

3.2.1 The Eulerian model

In the Eulerian model the different phases are treated mathematically as interpenetrating continua. Since the volume of a phase cannot be occupied by the other phases, the concept of phase volume fraction is introduced. These volume fractions are assumed to be continuous functions of space and time and their sum is equal to one. Conservation equations for each phase are derived to obtain a set of equations, which have similar structure for all phases. These equations are closed by providing constitutive relations that are obtained from empirical information, or, in the case of granular flows, by the application of the kinetic theory, in this case it is known as Eulerian Granular Model.

3.2.2 The Eulerian Granular Model (EGM)

The EGM treats the solid as a pseudo-fluid. The gas and solid are assumed to be continuous and fully interpenetrating in each control volume, so the conservative equations of mass and momentum originally derived from single-phase flow can be extended to describe the hydrodynamics of the gas-solid two-phase flow (Yang *et al.*, 2003). The conservative equations for the solid phase are based on the kinetic theory for granular flow which is an analogy to the kinetic theory for dense gases. From the

kinetic theory for granular flow three parameters were developed: the granular temperature, the coefficient of restitution and the radial distribution function. From these parameters, models for solid pressure and viscosity were developed. In the next five subsections the equations for unsteady state, without reaction, incompressible and isothermal conditions, are listed.

3.2.3 The Conservation Equations

- The volume fraction equation

The volume fractions of all phases must sum to one:

$$\alpha_g + \alpha_s = 1 \quad (3-8)$$

- The continuity equations

Gas phase:
$$\frac{\partial}{\partial t}(\alpha_g) + \nabla \cdot (\alpha_g \vec{v}_g) = 0 \quad (3-9)$$

Because of the complex physics involved in the gas-solid flow and to prevent unstable calculation, an unsteady condition is always used (Wachem and Almstedt 2003; Syamlal *et al.* 1993; Cammarata *et al.* 2003).

Solid phase:
$$\frac{\partial}{\partial t}(\alpha_s) + \nabla \cdot (\alpha_s \vec{v}_s) = 0 \quad (3-10)$$

- The Momentum Equations (Fluent, 1998):

Gas phase:

$$\rho_g \frac{\partial}{\partial t}(\alpha_g \vec{v}_g) + \rho_g \nabla \cdot (\alpha_g \vec{v}_g \vec{v}_g) = -\alpha_g \nabla p + \nabla \cdot \bar{\bar{\tau}}_g + \alpha_g \rho_g \vec{g} + \vec{F}_{sg} + \vec{S} \quad (3-11)$$

The second term on the left represents the net rate of momentum transfer by convection. The first term on the right represents the pressure force, the second term represents the viscous forces, the third term represents the gravitational force and the

fourth term represents the interaction forces between the gas phase and the solid phase. In this work only the drag force will be included since it is the main cause for the pinning phenomena. S represent the effect of the perforated plate, (see the boundary condition for the moving bed model).

Solid phase:

$$\rho_s \frac{\partial}{\partial t} (\alpha_s \vec{v}_s) + \rho_s \nabla \cdot (\alpha_s \vec{v}_s \vec{v}_s) = -\alpha_s \nabla p - \nabla P_s + \nabla \cdot \bar{\bar{\tau}}_s + \alpha_s \rho_s \vec{g} - \vec{F}_{sg} \quad (3-12)$$

In the above equations the subscripts (g) and (s) stand respectively for gas and solid phases, α is the volume fraction, P_s is the solid pressure, $\bar{\bar{\tau}}$ is the stress tensor, and F_{sg} is the drag force between the gas phase and the solid phase.

3.2.4 The Solid Pressure Equation

The terms in the solid momentum equation represent the same forces as in the gas equation. The solid momentum equation contains an extra term which is the solid pressure. The solid pressure term is added for the correction of the solid volume fraction. It prevents the void fraction from becoming less than the packed bed void fraction. Un-proper correction for the solid volume fraction could lead to numerical instability for EGM (Syamlal *et al.* 1993 and Cammarata *et al.* 2003). The solid pressure model used in this work which is developed from the kinetic theory is shown below (Fluent, 1998):

$$P_s = \alpha_s \rho_s \Theta_s + 2\rho_s (1 + e_s) \alpha_s^2 g_o \Theta_s \quad (3-13)$$

where e_s is the coefficient of restitution for particle collisions which needs to be specified during the model setup, g_o is the radial distribution function and Θ_s is the granular temperature which is described in the next section.

The solid pressure is composed of a kinetic term and a second term due to particle collisions. The function g_o is a distribution function that governs the transition from the “compressible” condition with $\alpha_s < \alpha_{s,\max}$, where the spacing between the solid particles can continue to decrease, to the “incompressible” condition with $\alpha_s = \alpha_{s,\max}$, where no further decrease in the spacing can occur. $\alpha_{s,\max}$ is the maximum packing limit achievable by the solid particles and this depends on the properties of the solid particles.

$$g_o = \left[1 - \left(\frac{\alpha_s}{\alpha_{s,\max}} \right)^{\frac{1}{3}} \right]^{-1} \quad (3-14)$$

3.2.5 The Granular Temperature

Since EGM is based on a direct analogy between the fluctuation of solid particles and the fluctuation of gas molecules due to local temperature, hence, the granular temperature has been used to describe the fluctuation energy of solid particles. Granular temperature is an essential ingredient in the solid pressure and solid viscosity formulation and hence needs to be computed as a part of the CFD calculation.

The granular temperature for the solid phase is proportional to the kinetic energy of the random motion of the particles. The granular energy transport equation derived from kinetic theory takes the form (Ding and Gidaspow, 1990):

$$\frac{3}{2} \left[\frac{\partial}{\partial t} \rho_s \alpha_s \Theta_s + \nabla \cdot \rho_s \alpha_s \bar{v}_s \Theta_s \right] = \left(-P_s \bar{I} + \bar{\tau}_s \right) : \nabla \bar{v}_s + \nabla \cdot \left(k_{\Theta_s} \nabla \Theta_s \right) - \gamma_{\Theta_s} + \Phi_{gs} \quad (3-15)$$

The first term on the right represents the generation of energy by the solid stress tensor, the second term represents the diffusion contribution, the third term represents the collisional dissipation of energy and the last term represents the energy exchange between the gas phase and the solid phase.

By neglecting convection and diffusion contributions in equation 3-15, Syamlal *et al.* (1993) obtained the algebraic relation below for the granular temperature:

$$\Theta_s = \left\{ \frac{-K_{1m} \alpha_s \text{tr}(\bar{D}_s) + \sqrt{K_{1m}^2 \text{tr}^2(\bar{D}_s) \alpha_s^2 + 4K_{4m} \alpha_s [K_{2m} \text{tr}^2(\bar{D}_s) + 2K_{3m} \text{tr}(\bar{D}_s^2)]}}{2\alpha_s K_{4m}} \right\}^2 \quad (3-16)$$

where

$$K_{1m} = 2(1 + e_s) \rho_s g_o \quad (3-17)$$

$$K_{2m} = \frac{4d_p \rho_s (1 + e_s) \alpha_s g_o}{3\sqrt{\pi}} - \frac{2}{3} K_{3m} \quad (3-18)$$

$$K_{3m} = \frac{d_p \rho_s}{2} \left\{ \frac{\sqrt{\pi}}{3(3 - e_s)} \left[1 + 0.4(1 + e_s)(3e_s - 1) \alpha_s g_o \right] + \frac{8\alpha_s g_o (1 + e_s)}{5\sqrt{\pi}} \right\} \quad (3-19)$$

$$K_{4m} = \frac{12(1 - e_s^2) \rho_s g_o}{d_p \sqrt{\pi}} \quad (3-20)$$

$$\bar{D}_s = \frac{1}{2} [\nabla \vec{v}_s + (\nabla \vec{v}_s)^T] \quad (3-21)$$

3.2.6 The Stress Tensor

The stress tensor for the gas and the solid phases is expressed as (Fluent, 1998):

$$\bar{\tau}_i = \alpha_i \mu_i [(\nabla \vec{v}_i + \nabla \vec{v}_i^T) - \frac{2}{3} (\nabla \cdot \vec{v}_i) \bar{\mathbf{I}}] \quad (3-22)$$

where i stands for gas or solid phases, μ is the viscosity $\bar{\mathbf{I}}$ is the unit tensor, and the second term on the right hand side is the effect of volume dilation. Solid viscosity is obtained from the kinetic theory as described below (Fluent, 1998):

$$\mu_s = \mu_{s,col} + \mu_{s,kin} + \mu_{s,fr} \quad (3-23)$$

The solid shear viscosity is composed of collisional, kinetic, and frictional parts. The collisional part of the shear viscosity is modeled as:

$$\mu_{s,col} = \frac{4}{5} \alpha_s \rho_s d_p g_o (1 + e_s) \left(\frac{\Theta_s}{\pi} \right)^{1/2} \quad (3-24)$$

The kinetic viscosity $\mu_{s,kin}$ has two models, one is from Syamlal *et al.* (1993):

$$\mu_{s,kin} = \frac{\alpha_s d_p \rho_s \sqrt{\Theta_s \pi}}{6(3 - e_s)} \left[1 + \frac{2}{5} (1 + e_s) (3e_s - 1) \alpha_s g_o \right] \quad (3-25)$$

and the other is from Gidaspow *et al.* (1992):

$$\mu_{s,kin} = \frac{10\rho_s d_p \sqrt{\Theta_s \pi}}{96\alpha_s (1+e_s) g_o} \left[1 + \frac{4}{5} g_o \alpha_s (1+e_s) \right]^2 \quad (3-26)$$

The frictional viscosity has the following expression:

$$\mu_{s,fr} = \frac{P_s \sin \Phi}{2\sqrt{I_{2D}}} \quad (3-27)$$

where P_s is the solids pressure, Φ is the angle of internal friction which needs to be specified during the model setup, and I_{2D} is the second invariant of the deviatoric stress tensor.

In a dense flow at low shear, where the secondary volume fraction for a solid phase nears the packing limit, the generation of stress is mainly due to friction between particles.

3.2.7 The Drag Force

The drag force between the gas phase and the solid phase F_{sg} is given by:

$$\vec{F}_{sg} = K_{sg} (\vec{v}_s - \vec{v}_g) \quad (3-28)$$

where K_{sg} is the fluid-solid exchange coefficient.

There are three models for K_{sg} :

- The first one is the Syamlal and O'Brien (1989) model:

$$K_{sg} = \frac{3\alpha_s \alpha_g \rho_g}{4v_{r,s}^2 d_p} C_D \left(\frac{Re_s}{v_{r,s}} \right) |\vec{v}_s - \vec{v}_g| \quad (3-29)$$

where $v_{r,s}$ is the terminal velocity correlation for the solid phase:

$$\nu_{r,s} = 0.5 \left(A - 0.06 \text{Re}_s + \sqrt{(0.06 \text{Re}_s)^2 + 0.12 \text{Re}_s (2B - A) + A^2} \right) \quad (3-30)$$

where

$$A = \alpha_g^{4.14} \quad (3-31)$$

$$B = 0.8 \alpha_g^{1.28} \text{ for } \alpha_g \leq 0.85 \text{ and} \quad (3-32)$$

$$B = \alpha_g^{2.65} \text{ for } \alpha_g > 0.85 \quad (3-33)$$

The relative Reynolds number of the solid phase is given by:

$$\text{Re}_s = \frac{\rho_g d_p |\vec{v}_s - \vec{v}_g|}{\mu_g} \quad (3-34)$$

The drag function is given by:

$$C_D = \left(0.63 + \frac{4.8}{\sqrt{\text{Re}_s / \nu_{r,s}}} \right)^2 \quad (3-35)$$

This model is appropriate when the kinetic viscosity is modeled by Equation 3-25.

- The second model is the Wen and Yu (1966) model:

$$K_{sg} = \frac{3}{4} C_D \frac{\alpha_s \alpha_g \rho_g |\vec{v}_s - \vec{v}_g|}{d_p} \alpha^{-2.65} \quad (3-36)$$

where

$$C_D = \frac{24}{\alpha_g \text{Re}_s} \left[1 + 0.15 (\alpha_g \text{Re}_s)^{0.687} \right] \quad (3-37)$$

Re_s is defined by Equation 3-34. This model is appropriate for dilute systems.

- The third model is the Gidaspow *et al.*(1992) model:

The Gidaspow's model is a combination of the Wen and Yu (1966) model and the Ergun (1952) equation.

In this study, when $\alpha_g > 0.8$, the Wen and Yu model will be used. However, when $\alpha_g \leq 0.8$:

$$K_{sg} = 150 \frac{\alpha_s (1 - \alpha_g) \mu_g}{\alpha_g d_p^2} + 1.75 \frac{\rho_g \alpha_s |\vec{v}_s - \vec{v}_g|}{d_p} \quad (3-38)$$

This model is recommended for high solid volume fraction. In modeling the moving bed reactor Gidaspow's model will be used.

3.2.8 Modeling of Turbulence

In comparison with single-phase flows, the number of terms to be modeled in the momentum equations in multiphase flows is large, and this makes the modeling of turbulence in multiphase simulations extremely complex. Only the κ - ε model is available with EGM. There are three methods based on κ - ε model for modeling turbulence: the mixture turbulence model, the dispersed turbulence model and the turbulence model for each phase.

3.2.9 Initial and Boundary Conditions

Initial Conditions

Prior to the start of iteratively solving the equations, the velocity, volume fraction and pressure values throughout the computational domain are arbitrarily set. In this case the initial gas and solid velocity was 0 m/s and the initial gauge pressure was 0 Pa. Also the bed section was initialized with 0.5 solid volume fraction.

Boundary Conditions (see Figure 3.1)

- **Gas inlet:** A uniform inlet velocity condition is used. It equals the inlet flow rate divided by the cross sectional area of the reactor inlet.
- **Gas outlet:** An atmospheric pressure outlet condition is used.
- **Bed top and bottom:** A pressure condition is used. The pressure is assumed to be atmospheric to make the solid down movement under the gravitational force only.
- **Reactor walls:** A no-slip condition is used for gas and solid.
- **Perforated plates:** A porous media condition is used. Knowing ε and d_p , bed resistances are calculated from Equations 3.4 and 3.5. The solid volume fraction is fixed to be zero at the perforated plate. Therefore solid only exists in the bed section.

Since a porous-jump model is not available in the EGM, a perforated plate is represented by a thin solid bed. Using a thin solid bed to represent the perforated plate required fine meshing and so increases the number of the cells. This makes the EGM limited to a small and 2-D geometry.

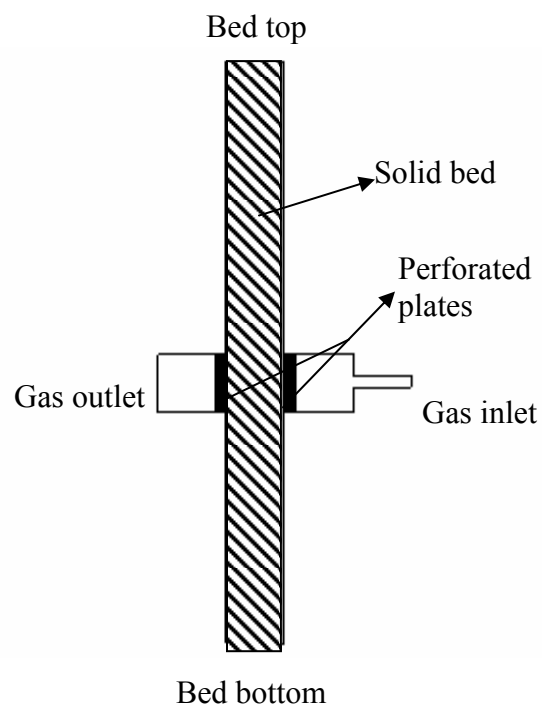


Figure 3.1: A schematic diagram of the RFMBR.

3.3 The Solution Methodology

A good understanding of the numerical solution algorithm is required for CFD modeling. Three mathematical concepts are useful in determining the success of such algorithms: convergence, consistency and stability. **Convergence** is the property of a numerical method to produce a solution which approaches the exact solution as the grid spacing, control volume size or element size is reduced to zero. **Consistent** numerical schemes produce systems of algebraic equations which can be demonstrated to be equivalent to the original governing equation as the grid spacing tends to zero. **Stability** is associated with damping of errors as the numerical method proceeds. Convergence is usually very difficult to establish theoretically and in practice we use Lax's equivalence theorem. This theorem states that for linear problems a necessary and sufficient condition for convergence is that the method is both consistent and stable.

In CFD methods the governing equations are non-linear. In such problems consistency and stability are necessary conditions for convergence, but not sufficient. In this case three crucial properties are: conservativeness, boundedness and transportiveness. FLUENT is used in this study for the numerical simulations. It is based on a finite volume method. The finite volume approach guarantees local conservation of a fluid property ϕ for each control volume. Numerical schemes which possess the **conservativeness** property also ensure global conservation of the fluid property for the entire domain. The **boundedness** property is akin to stability and requires that in a linear problem without sources the solution is bounded by the maximum and minimum boundary values of the flow variable. Although flow

problems are non-linear it is important to study the boundedness of a finite volume scheme for a closely related, but linear, problem.

All flow processes contain effects due to convection and diffusion. In diffusive phenomena, such as heat conduction, a change of temperature at one location affects the temperature in more or less equal measure in all directions around it. Convective phenomena involve influencing exclusively in the flow direction so that a point only experiences effects due to changes at upstream locations. Finite volume schemes with the **transportiveness** property must account for the directionality of influencing in terms of the relative strength of diffusion to convection. Conservativeness, boundedness and transportiveness are now commonly accepted as alternatives for the more mathematically rigorous concepts of convergence, consistency and stability.

To solve the Navier-Stokes Equations, a linkage between velocity and pressure is required. The difficulty in calculating the velocity field lies in the unknown pressure field. The pressure gradient forms a part of the source term for a momentum equation. Yet there is no obvious equation for obtaining pressure. It is true that for a given pressure field, there is no particular difficulty in solving the momentum equations. But the way to determine the pressure field seems rather obscure. The choice of algorithms is a critical issue for solving the system of transport equations involving several dependent variables.

Pressure-velocity coupling is achieved by discretization of the continuity equation to derive an equation for pressure from the discrete continuity equation. Pressure velocity coupling is required only for the segregated solver

(FLUENT/UNS). One needs not to specify it for the coupled solvers (RAMPANT). FLUENT provides the option to choose among three pressure-velocity coupling algorithms: SIMPLE, SIMPLEC, and PISO. The semi-implicit method for pressure-linked equations (SIMPLE) algorithm is described very precisely by Patankar (1980). The above three mentioned algorithms have also been described by Versteeg & Malalasekera (1995) both for transient and steady flows. Fluent manuals (1998) provide good explanation of the abovementioned algorithms.

In FLUENT, both the standard SIMPLE algorithm and the SIMPLEC (SIMPLE-Consistent) algorithm are available. SIMPLE is the default, but many problems will benefit from the use of SIMPLEC, particularly because of the increased under-relaxation that can be applied. The Pressure-Implicit with Splitting of Operators (PISO) pressure-velocity coupling scheme, part of the SIMPLE family of algorithms, is based on the higher degree of the approximate relation between the corrections for pressure and velocity.

For relatively uncomplicated problems (laminar flows with no additional models activated) in which convergence is limited by the pressure-velocity coupling, a converged solution can often be obtained more quickly using SIMPLEC. With SIMPLEC, the pressure-correction under-relaxation factor is generally set to 1.0, which aids in convergence speed-up. In some problems, however, increasing the pressure-correction under-relaxation to 1.0 can lead to instability. For such cases, a more conservative under-relaxation value or the SIMPLE algorithm will be needed. For complicated flows involving turbulence and/or additional physical models, SIMPLEC will improve convergence only if it is being limited by the pressure-

velocity coupling. Often it will be one of the additional modeling parameters that limit convergence; in this case, SIMPLE and SIMPLEC will give similar convergence rates.

3.4 The Grid System

FLUENT can use grids comprised of triangular or quadrilateral cells (or a combination of the two) in 2D, and tetrahedral, hexahedral, pyramid, or wedge cells (or a combination of these) in 3D. The choice of which mesh type to use will depend on the application. When choosing the mesh type, one should consider the following issues:

- Set-up time
- Computational expense
- Numerical diffusion

For discretization scheme in CFD, generally a staggered grid system is used. In this system, the scalar quantities are computed at the center of every grid cell, while the vector quantities are computed at the center of the faces. A recent study by Meier *et al.* (1999) has indicated that staggered grid based methods reach grid independent solutions earlier than co-located grids though the convergence behavior is more or less the same for both types of grids. A computational domain accurately representing the domain of the vessel is needed. The co-ordinate system and the meshing technique will be chosen depending on the complexity of geometry.

3.5 Solver Types

There are two choices of numerical methods provided by Fluent:

- Segregated solver ("FLUENT/UNS")
- Coupled solver ("RAMPANT")

Using either method FLUENT will solve the governing integral equations for the conservation of mass and momentum, and (when appropriate) for energy and other scalars such as turbulence and chemical species. In both cases a control-volume-based technique is used that consists of:

1. Division of the domain into discrete control volumes thus creating a computational grid.
2. Integration of the governing equations on the individual control volumes to construct algebraic equations for the discrete dependent variables ("unknowns") such as velocities, pressure, temperature, and other conserved scalars.
3. Linearization of the discretized equations and solution of the resultant linear equation system to yield updated values of the dependent variables.

The two numerical methods employ a similar discretization process (finite-volume), but the approach used to linearize and solve the discretized equations is different.

3.5.1 The Segregated Solution Method

Using this approach, the governing equations are solved sequentially (i.e., segregated from one another). Because the governing equations are non-linear (and coupled), several iterations of the solution loop must be performed before a converged solution is obtained. Every iteration consists of the steps illustrated in Figure 3.2.

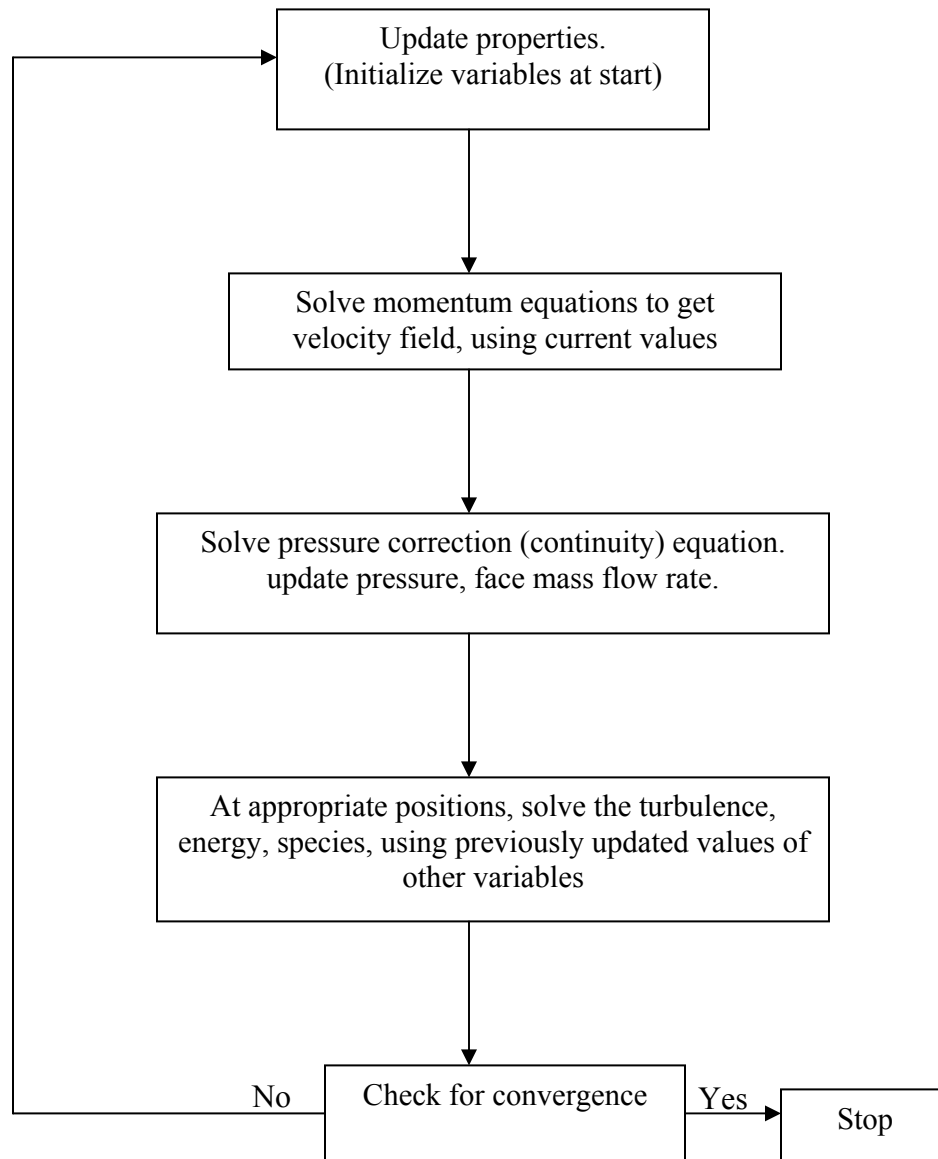


Figure 3.2: Overview of the segregated solution method.

3.5.2. The Coupled Solution Method

Using this approach the governing equations of continuity, momentum, and (where appropriate) energy and species transport are solved simultaneously (i.e., coupled together). Governing equations for additional scalars will be solved sequentially (i.e., segregated from one another and from the coupled set) using the procedure described for the segregated solver in Segregated Solution Method. Because the governing equations are non-linear (and coupled), several iterations of the solution loop must be performed before a converged solution is obtained. Each iteration consists of the steps illustrated in Figure 3.3 and outlined below:

3.6 Multiphase Solution Method

For Eulerian multiphase calculations, Fluent uses the Phase Coupled SIMPLE (PC-SIMPLE) algorithm for the pressure-velocity coupling (Vasquez and Ivanov, 2000). PC-SIMPLE is an extension of the SIMPLE algorithm to multiphase flows. The velocities are solved coupled by phases, but in a segregated fashion. The block algebraic multigrid scheme used by the coupled solver described in Weiss *et al.* (1990) is used to solve a vector equation formed by the velocity components of all phases simultaneously. Then, a pressure correction equation is built based on total volume continuity rather than mass continuity. Pressure and velocities are then corrected so as to satisfy the continuity constraint.

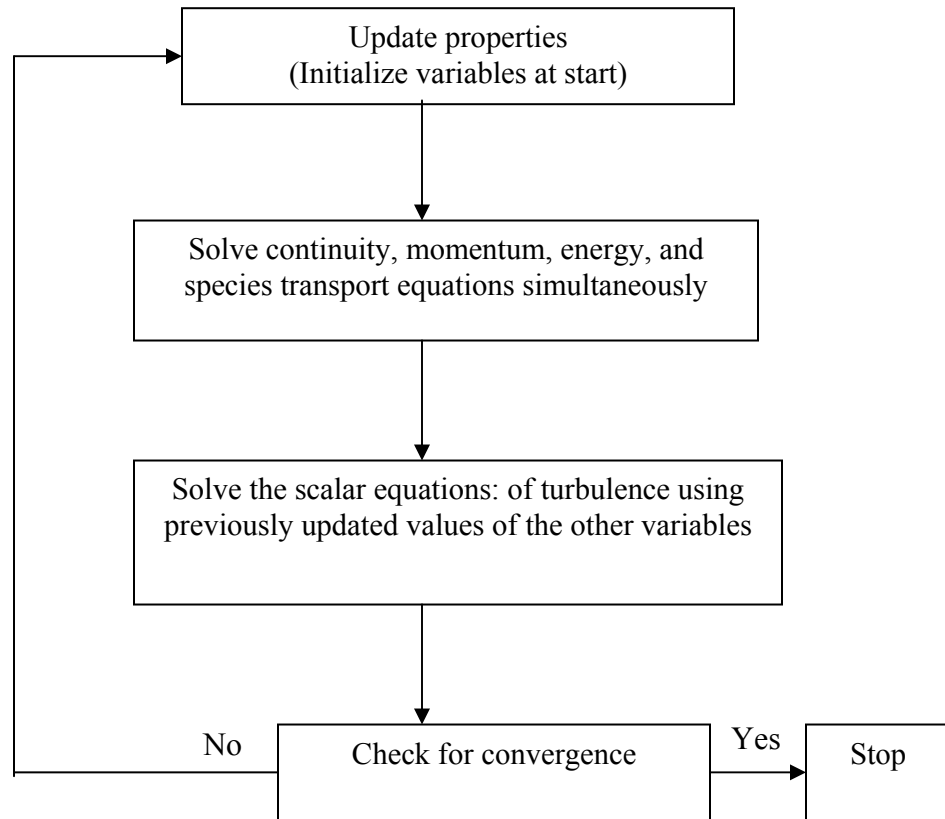


Figure 3.3: Overview of the coupled solution method.

CHAPTER 4

SIMULATION OF FLOW IN A RADIAL FLOW FIXED BED REACTOR (RFBR)

4.1 Introduction

One objective of the present work is to simulate the flow in a radial fixed bed reactor (RFBR). A detailed knowledge of the flow profile will help in analyzing the pinning phenomena in a moving bed reactor. Since the particle downward velocity is very low ($v < 1\text{mm/s}$), the flow profiles of the moving bed and fixed bed are almost the same. There is no significant difference between the pressure drop of the moving and fixed bed reactors prior to the initiation of the pinning (Song *et al.*,1994).

A schematic diagram of the radial flow reactor simulated in the present study is shown in Figure 4.1. The reactor consists of two perforated cylinders and a reactor wall. The gas stream enters the annular channel where it is distributed through the perforated plate. It then flows radially across the particle bed towards the center pipe. The driving force of the flow across the bed is the radial pressure drop between the annular channel and the center pipe.

4.2 Reactor Dimensions and Operating Conditions

The reactor dimensions and operating conditions used in this study are the same as those used by Song *et al.* (1993, 1994). These dimensions and operating conditions are shown in Tables 4.1 and 4.2. Figure 4.1 represents the conventional configuration, which is the CP-z configuration. The flow in the other three configurations

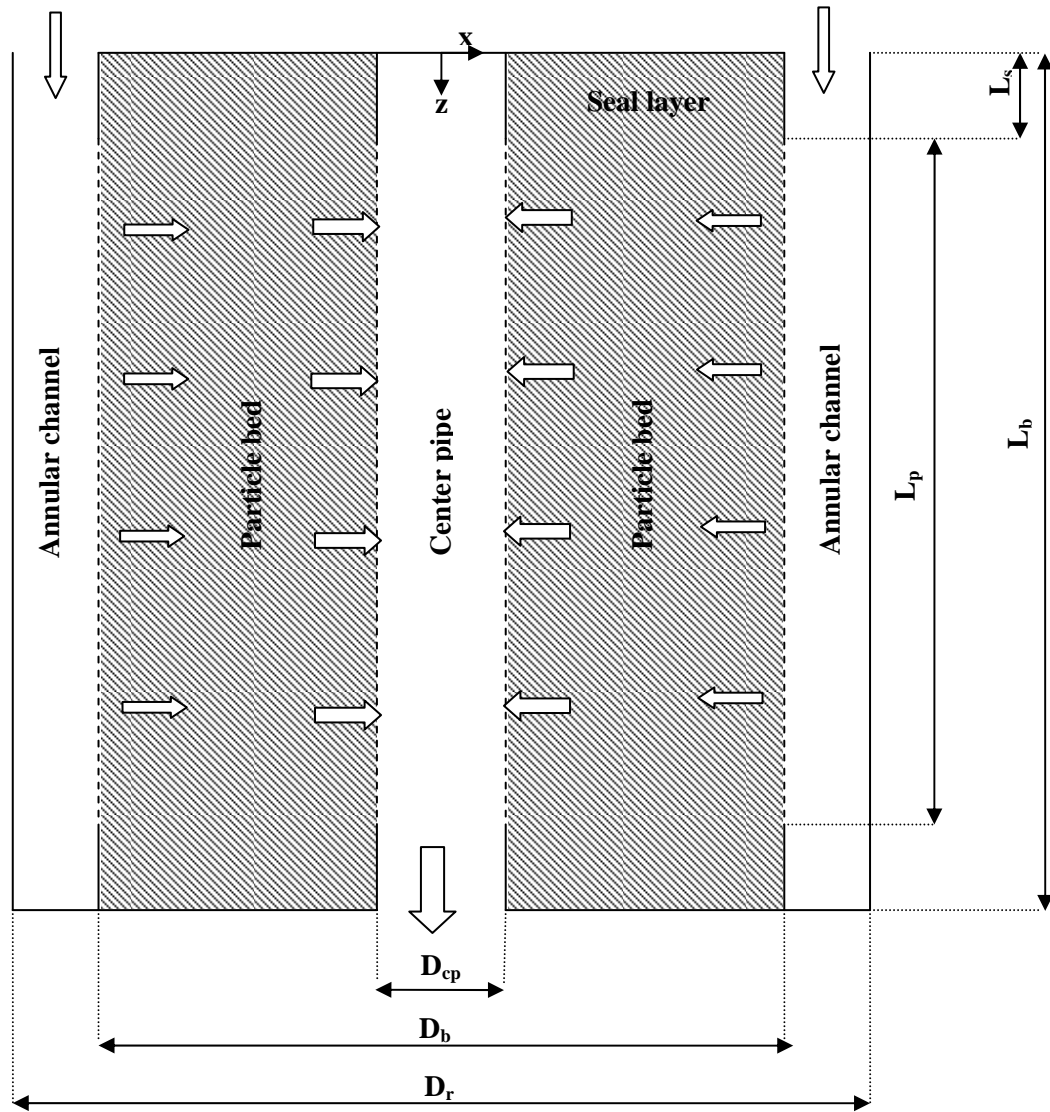


Figure 4.1: A schematic diagram of a radial flow reactor, where L_s , L_p and L_b are the lengths of the seal layer, the perforation section and the bed, respectively, D_{cp} and D_r are the diameters of the center pipe and the reactor, respectively and D_b is the outer bed diameter.

was also simulated. The RFBR model consists of three different sections, an annular channel, a bed section and a center pipe channel. All of them have the same length but different width. The lengths and diameters of these three sections are given in Table 4.1.

Table 4.1: Reactor dimensions.

Dimension*	L_s	L_p	L_b	D_{cp}	D_b	D_r
Value (mm)	160	1680	2000	130	410	500

*see Figure 4.1

Table 4.2: Boundary conditions.

Boundary Condition	Inlet flow rate (m^3/h)	Bed porosity	Center pipe porosity	Annular channel Porosity
Value	200	0.35	0.012	0.3

A three dimensional numerical model is constructed using the information in Figure 4.1 and Table 4.1. The geometry is meshed using an unstructured tetrahedral mesh. A mesh size of 18 mm was used and the total number of cells obtained is 535573 cells. Figure 4.2 shows the grid of the top part of the model.

4.2.1 Simulation Results

Fluent was used to solve the governing equations of the model. The model was isothermal at a temperature of 300 K. Air was the feed material and the bed particle

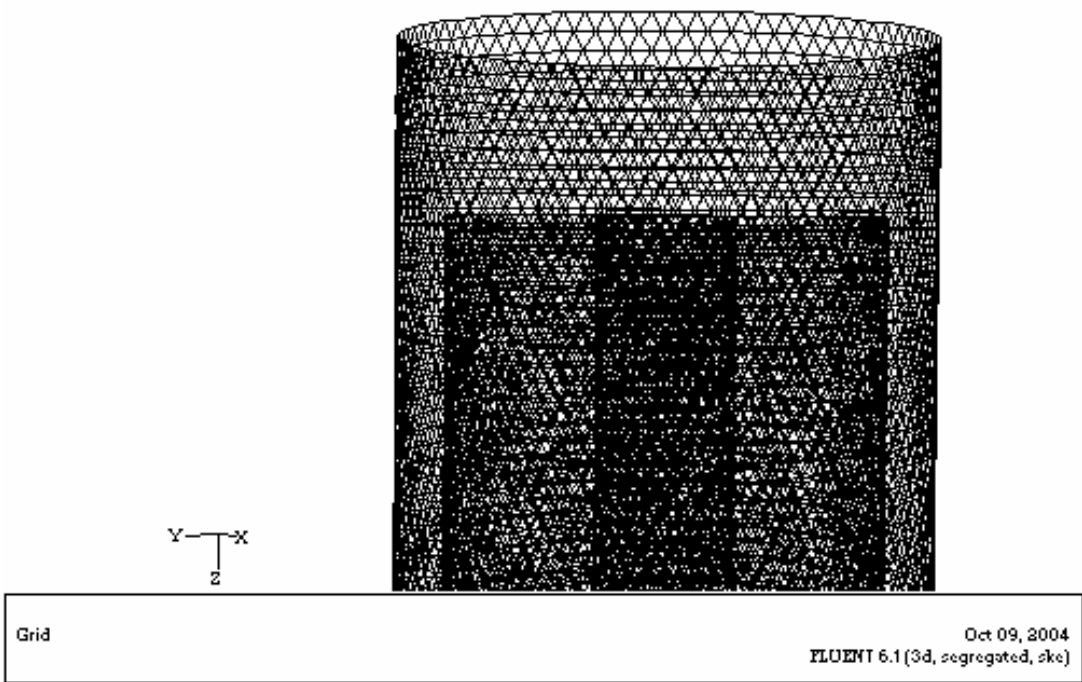


Figure 4.2: The grid for the radial flow reactor.

diameter was 1.8 mm. Using the boundary conditions in Table 4.2, typical results of the model shown in Figures 4.3-4.7 were generated.

Figure 4.3 shows the velocity profile in the annular channel. Gas with a velocity of 0.86 m/s enters the annular channel from the top. The velocity remains the same until the starting of the perforated wall. As the gas flows down the annular channel, it loses mass through the perforated wall, therefore the velocity decreases along the annular channel. This annular velocity reaches zero at the bottom seal section. From the annular channel gas travels radially through the catalyst bed.

Figure 4.4 shows the radial pressure gradient and the radial velocity profile inside the RFBR. At the bed the cross sectional area (CSA) open to flow increases, therefore, the lowest velocity exists there compared to the annular channel and center pipe. This can be seen in Figures 4.4 and 4.5. Due to the effect of the catalyst bed and the reduction in the CSA of the flow, the velocity increases towards the center pipe as shown in Figure 4.6. The highest velocity in the catalyst bed is at the center pipe perforated wall. This high velocity is a concern for the moving bed reactor, since it may pin some of the catalyst against the center pipe perforated wall. The gas stream is collected in the center pipe along the bed length. The center pipe velocity increases axially as shown in Figure 4.7. Figures 4.3-4.7 show a typical flow profile for an RFBR. However before a detailed analysis is done, the numerical model will be tested to establish that the results are independent of the grid interval size.

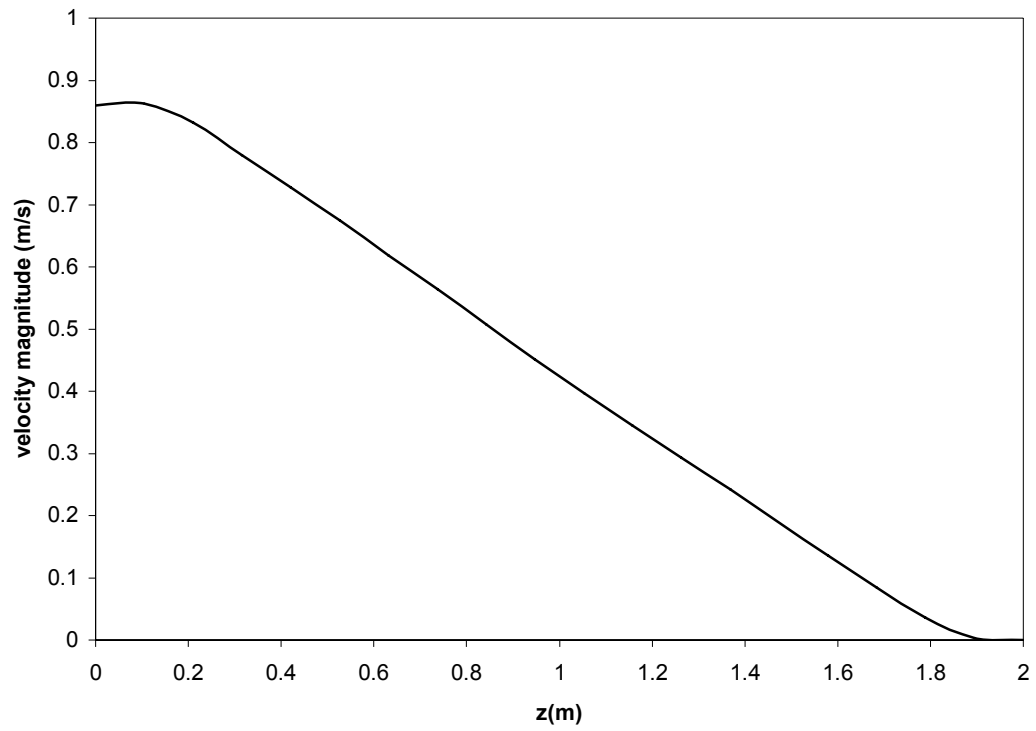
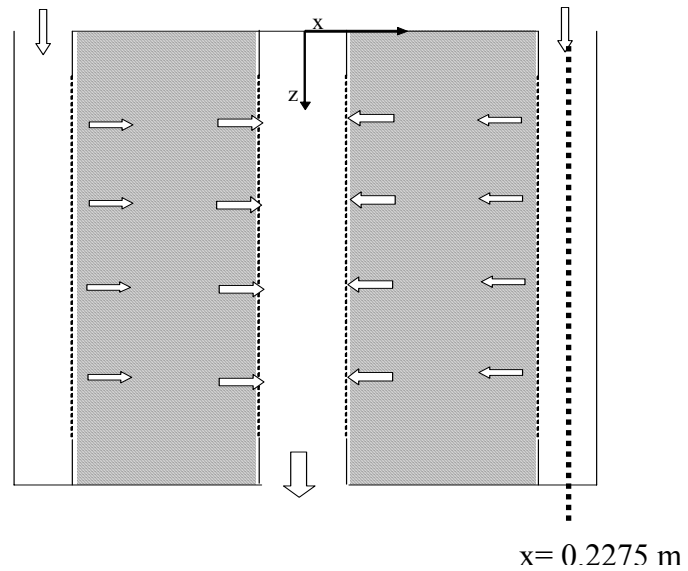
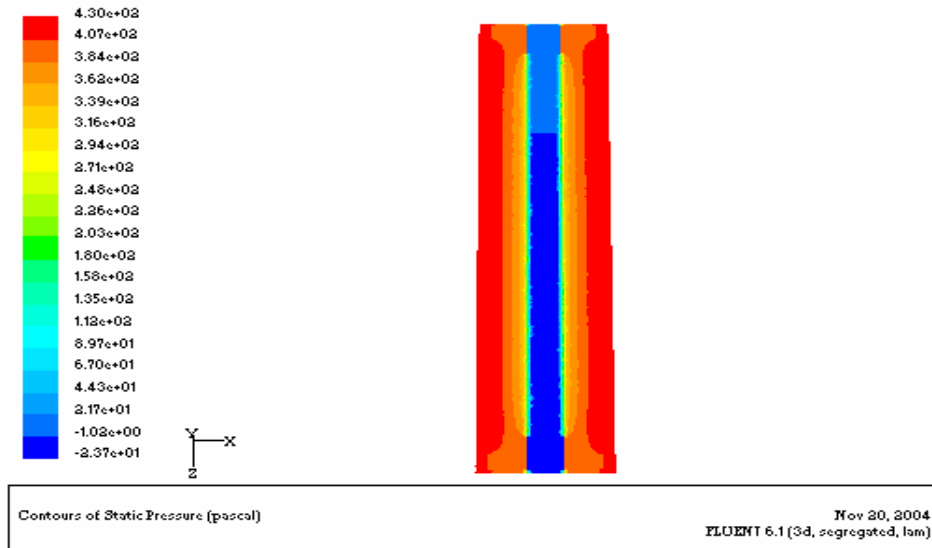
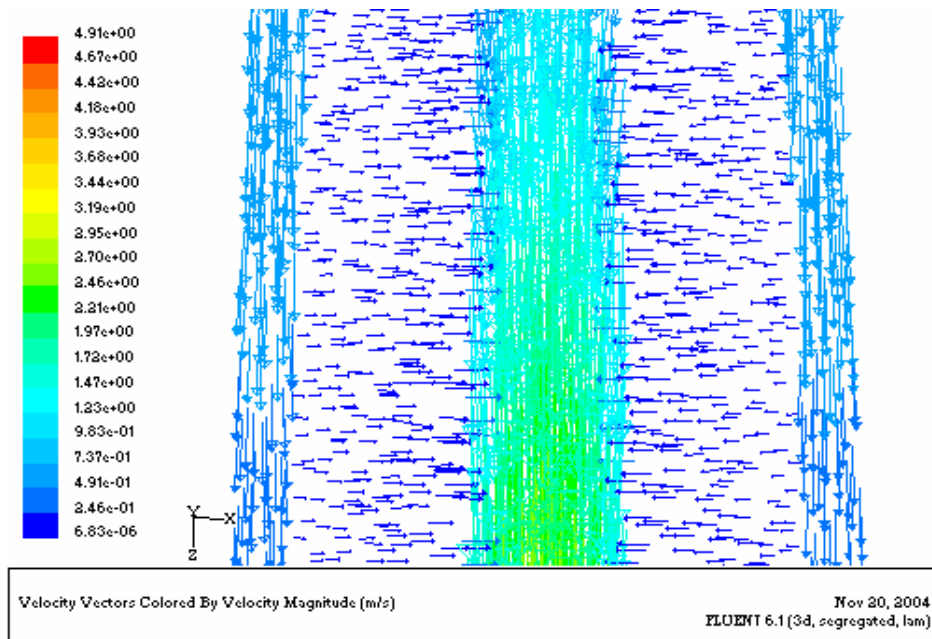


Figure 4.3: A profile of the annular channel velocity in an x - z plane along a line passing through the center of the annulus.



(a)



(b)

Figure 4.4: (a) Static pressure contours in a vertical centered plane (x-z plane), (b) magnified velocity vectors in a vertical centered plane (x-z plane).

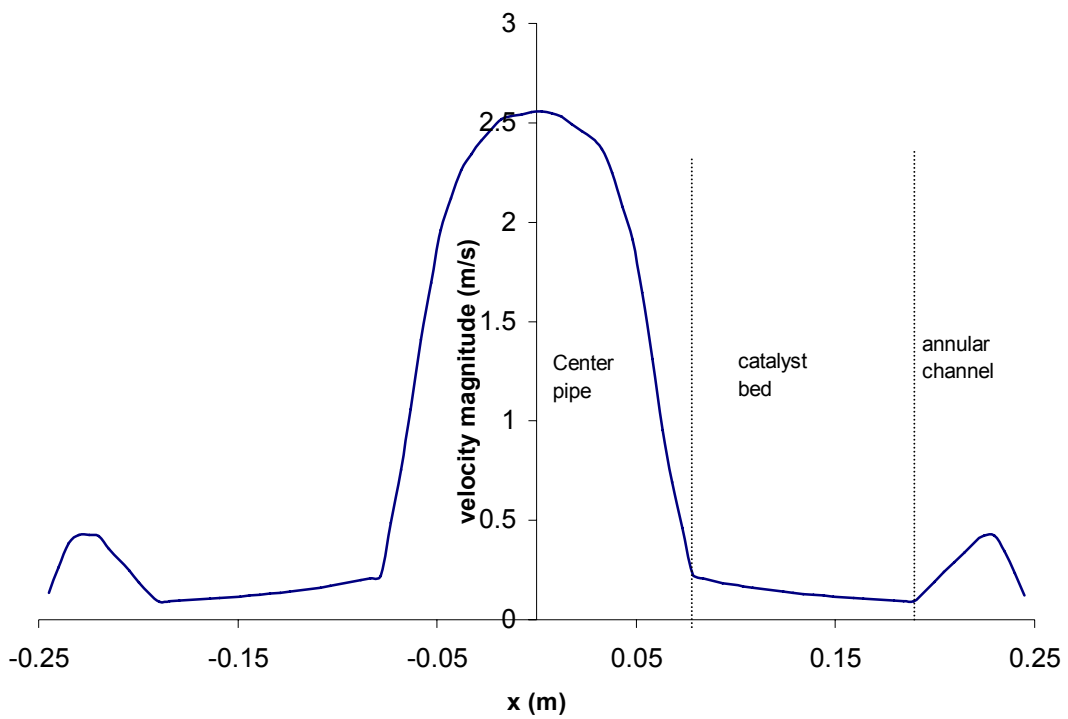
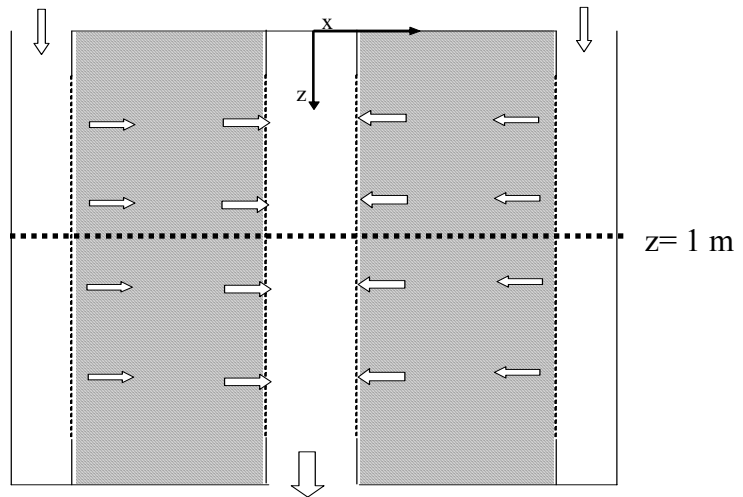


Figure 4.5: Velocity profile along the reactor diameter, at the center of the bed $z=1$ m.

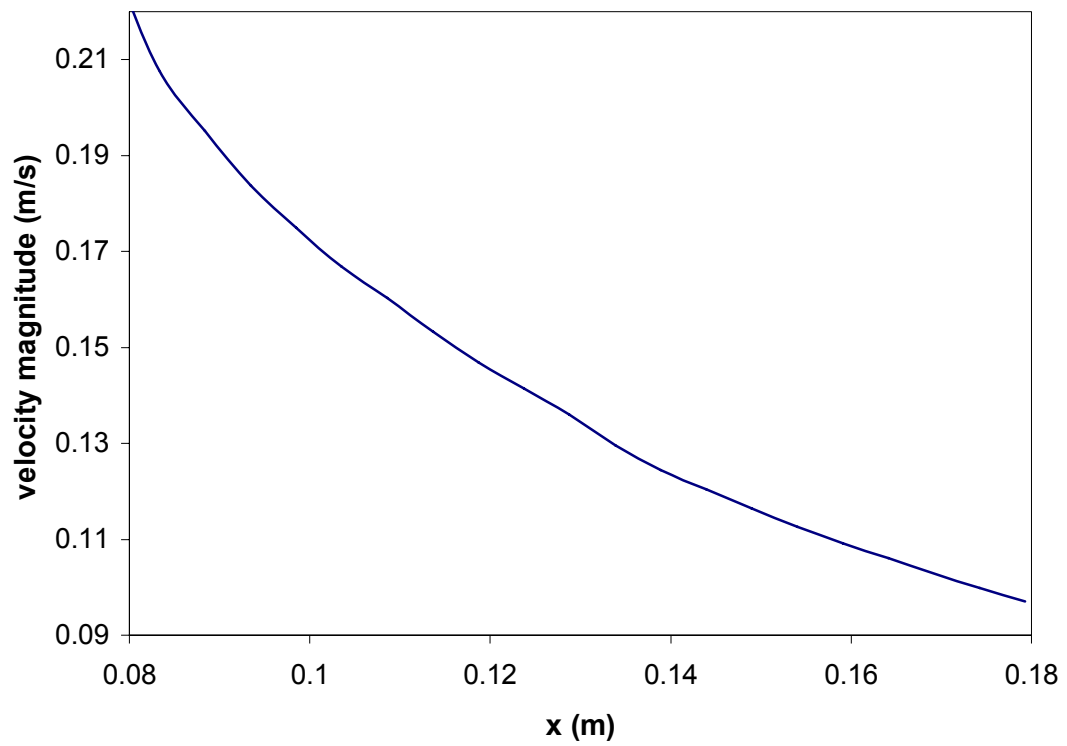
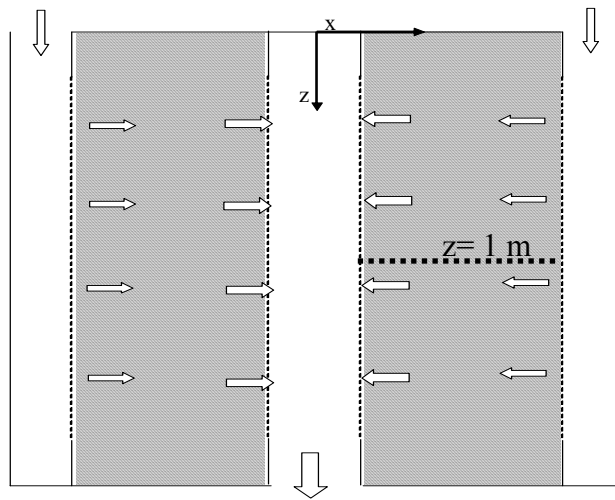


Figure 4.6: Velocity profile along catalyst bed section, at the center of the bed $z=1 \text{ m}$.

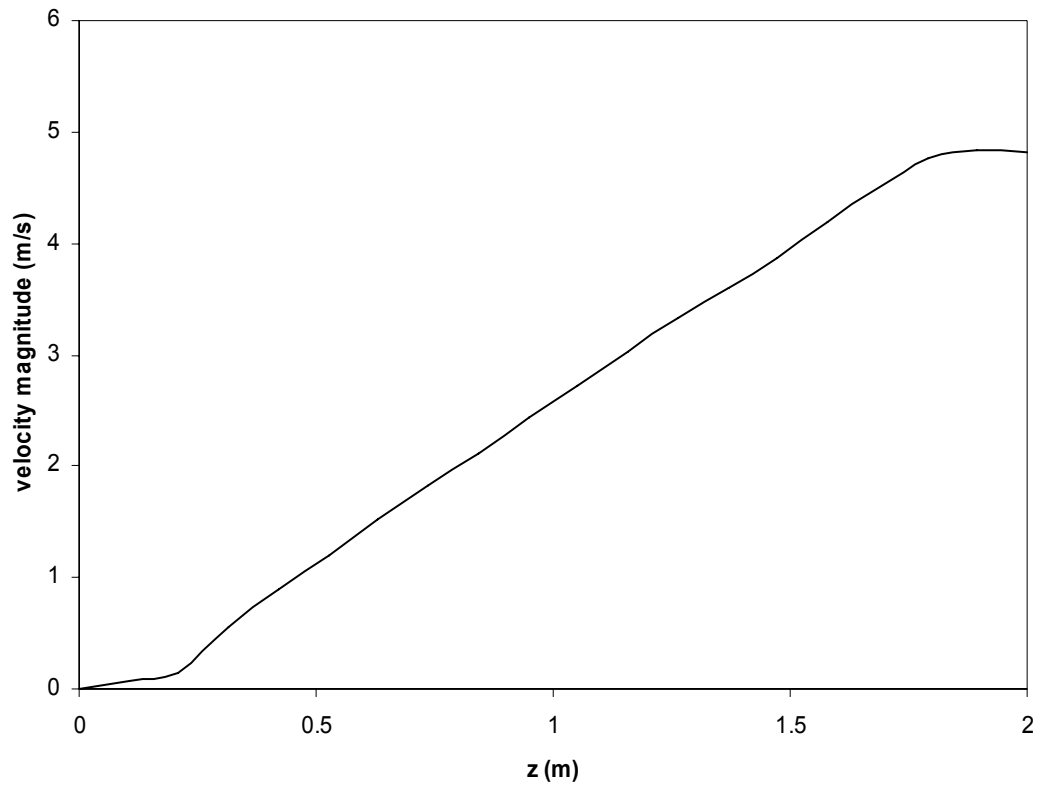
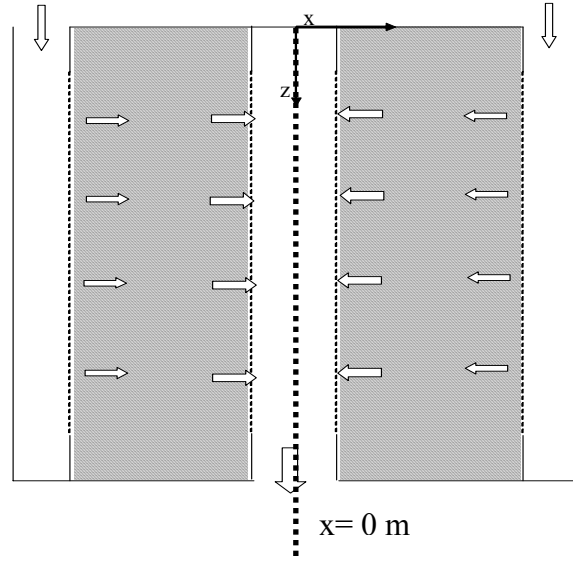


Figure 4.7: A profile of the velocity in the center pipe along the bed length, at the center of an x-z plane of the channel.

4.2.3 Effects of the Mesh Size

In general using a small mesh size may lead to a more accurate solution. However, using a small mesh size is limited by the computational power and memory, and consequently the time required to reach a converged solution. On the other hand, using a large mesh size may lead to an incorrect solution. To optimize the availability of computational resources and make the solution independent of the mesh size, grid independency tests were performed. This was done by starting with a large mesh size and then decreasing the mesh size until there is no significant variation in the results.

The RFBR model consists of three different sections, an annular channel, a bed section and a center pipe channel. All of them have the same length but different widths. The annular channel has the smallest width which makes it control the mesh size. The widths of the annular channel, bed section and center pipe channel are 45, 140 and 130 mm respectively. In the grid independency study, five mesh sizes of 25, 22, 20, 18 and 15 mm were used. The corresponding total number of computational cells was 167480, 295723, 359206, 535573 and 825846 cells respectively.

Figures 4.8 to 4.14 illustrate the effect of the mesh size on the results. Since each section of the RFBR has different flow profile, a through grid independency analysis was done. Figure 4.8 shows that all mesh sizes give the same velocity profile across the reactor radial direction. There is no significant difference in the results especially at the bed section since it has the largest gap and lowest velocity. However Figures 4.9 and 4.10 show that using mesh sizes of 25, 22 or 20 mm leads to fluctuations in the velocity and pressure profiles in the annular channel since it has the lowest gap.

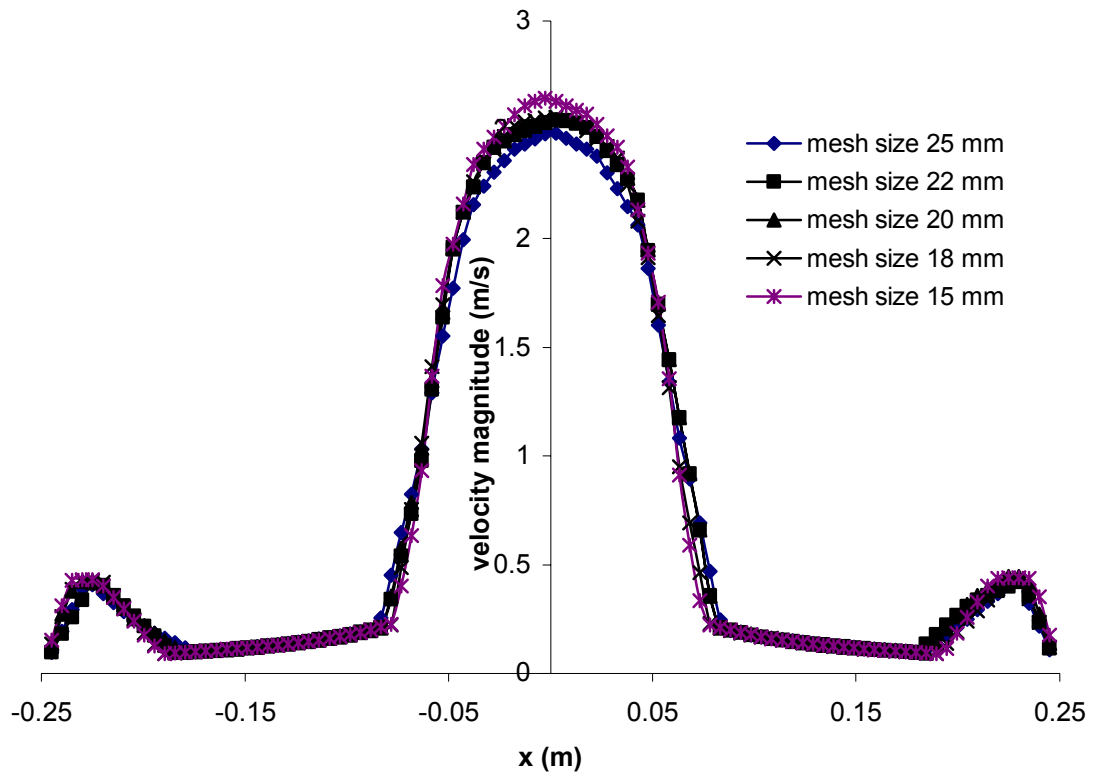
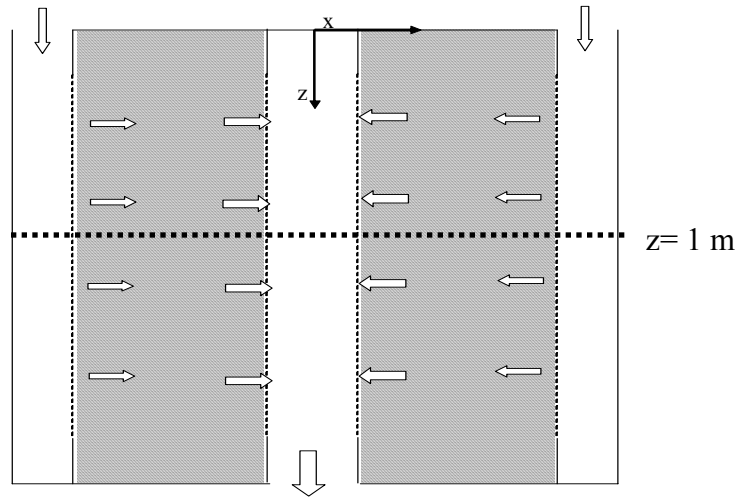


Figure 4.8: The velocity profile along the reactor diameter, at the center of the bed $z=1$ m, for five different mesh sizes.

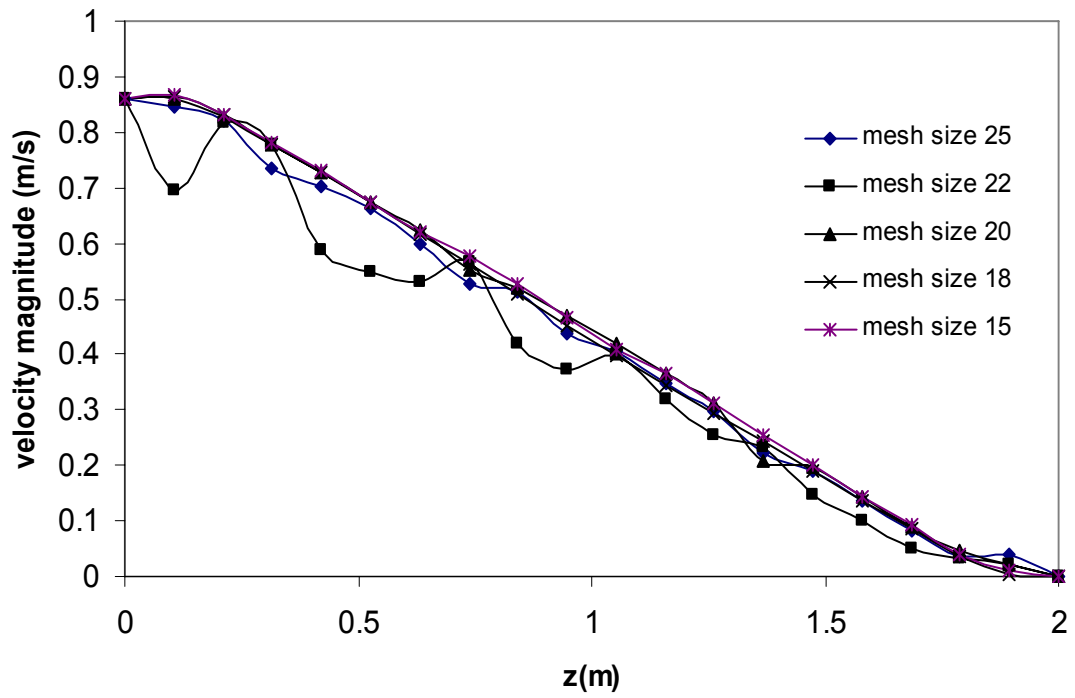
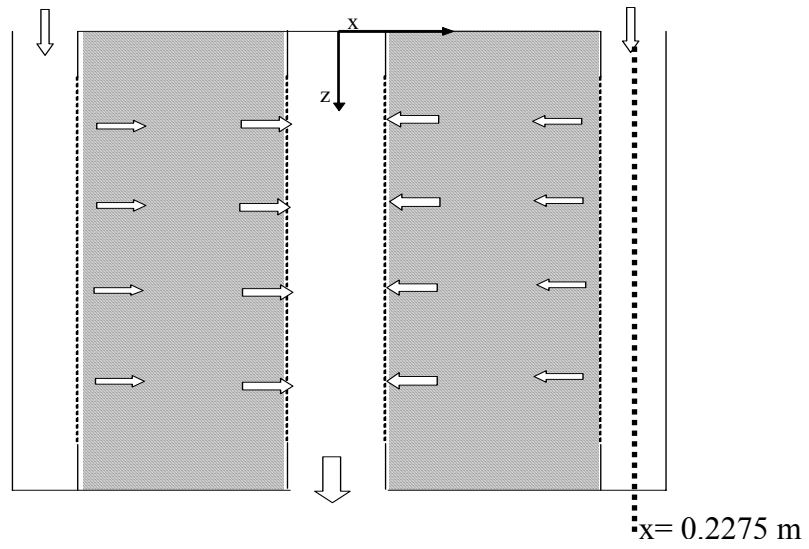


Figure 4.9: The annular channel velocity profile along the bed length, at the center of an x-z plane of the channel, for five different mesh sizes.

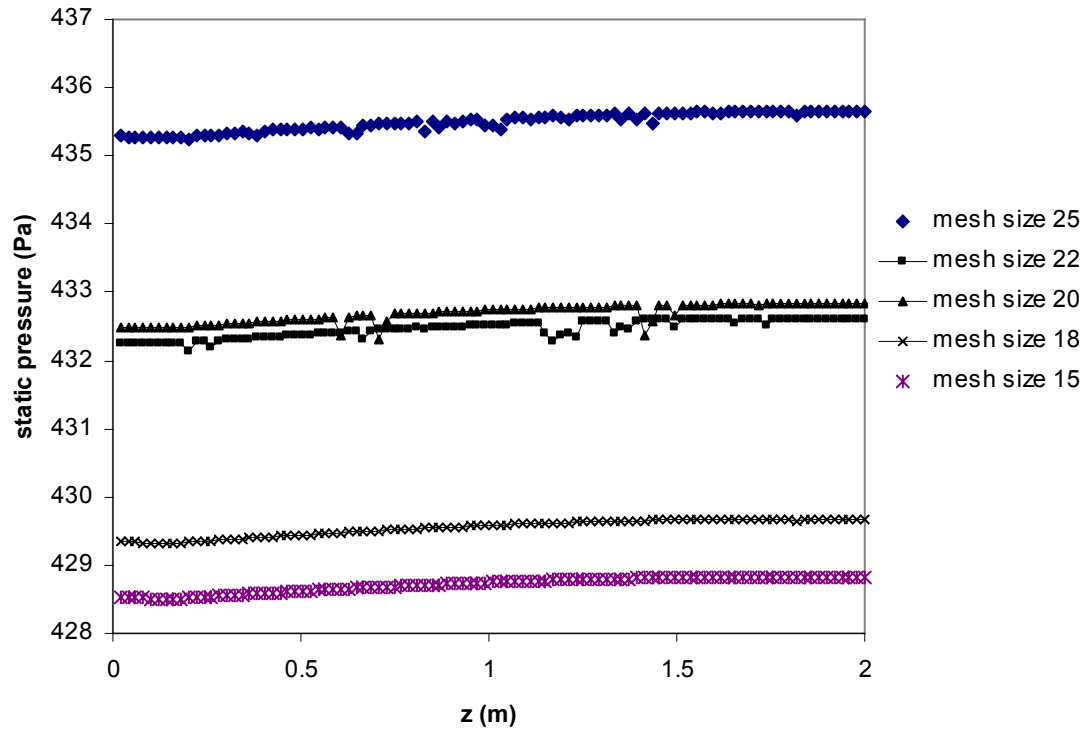
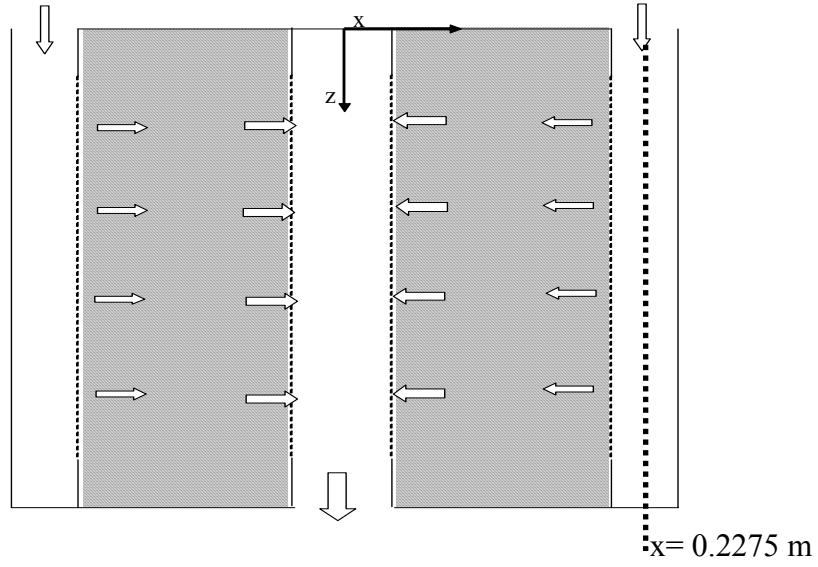


Figure 4.10: Axial profile of the static pressure in the annular channel, for five different mesh sizes.

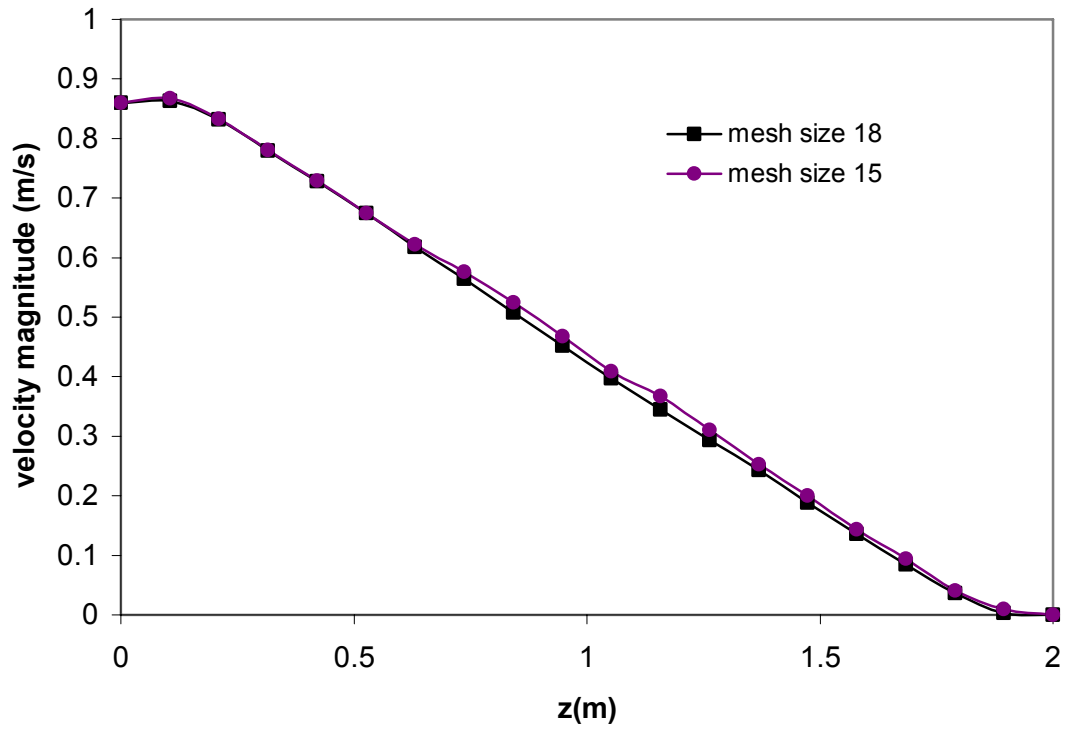
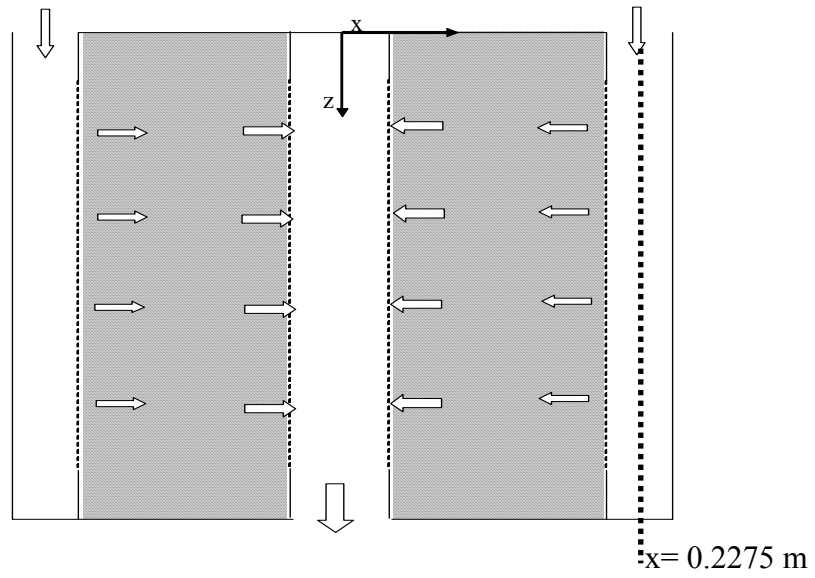


Figure 4.11: Annular channel velocity profile along the bed length, at the center of x - z plane of the channel, for mesh sizes 18 and 15 mm.

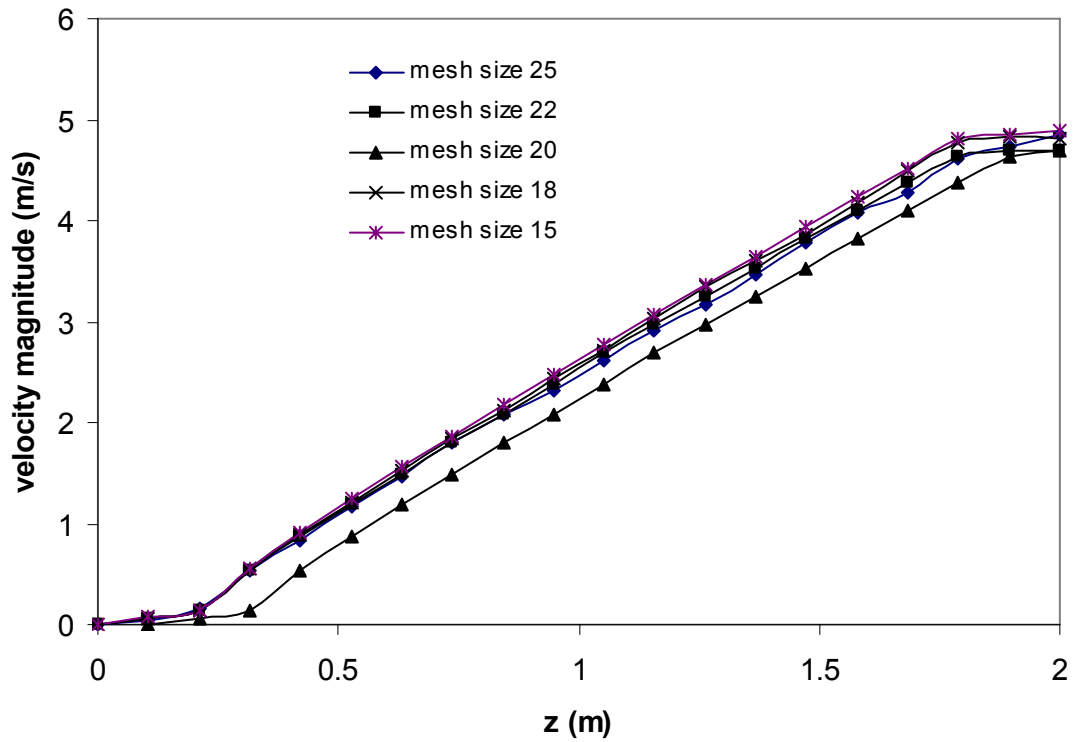
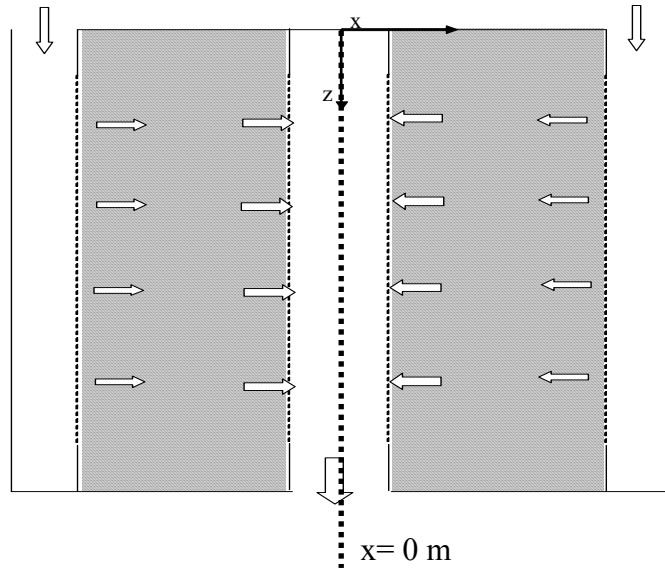


Figure 4.12: Center pipe velocity profile along the bed length, at the center of x-z plane of the channel, for five different mesh sizes.

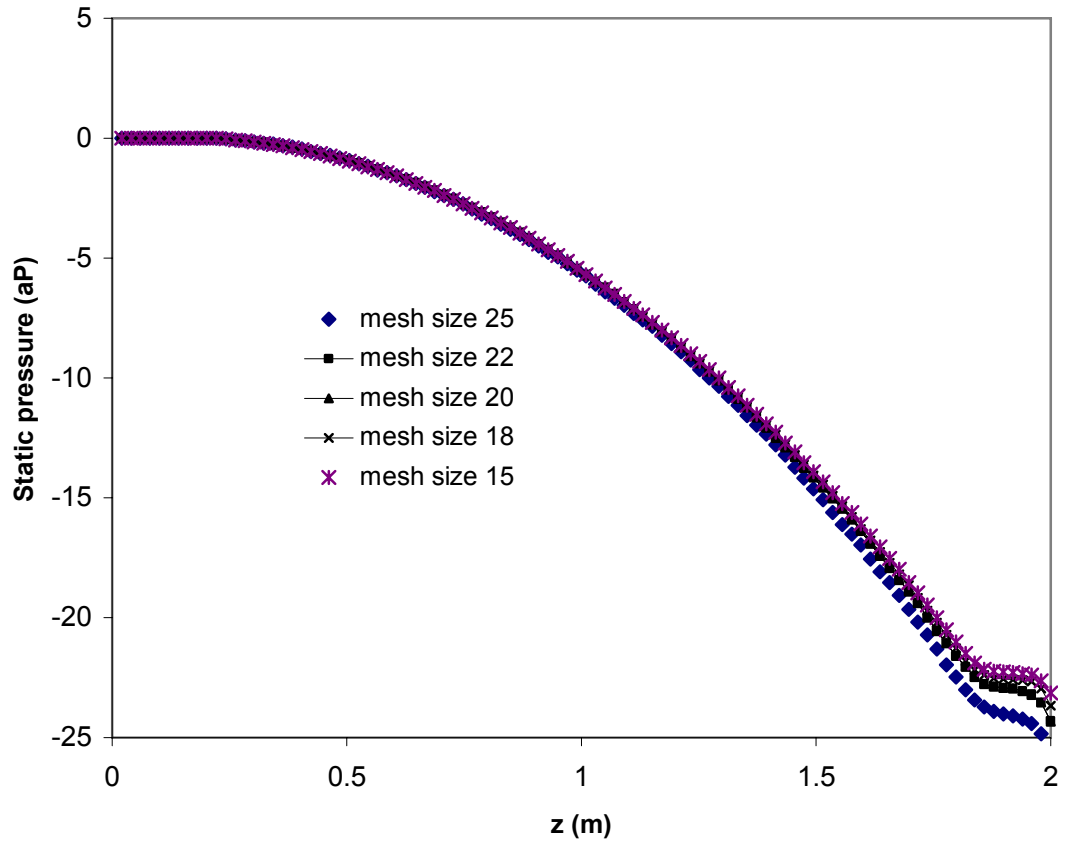
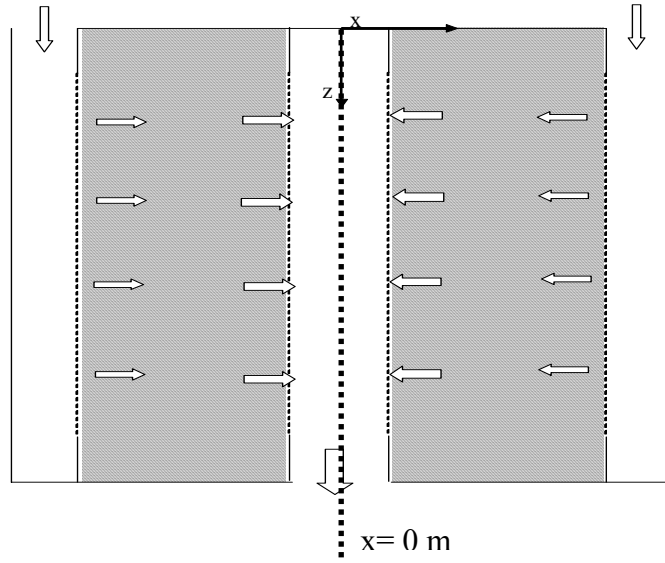


Figure 4.13: Axial profile of the static pressure in the center pipe, for five different mesh sizes.

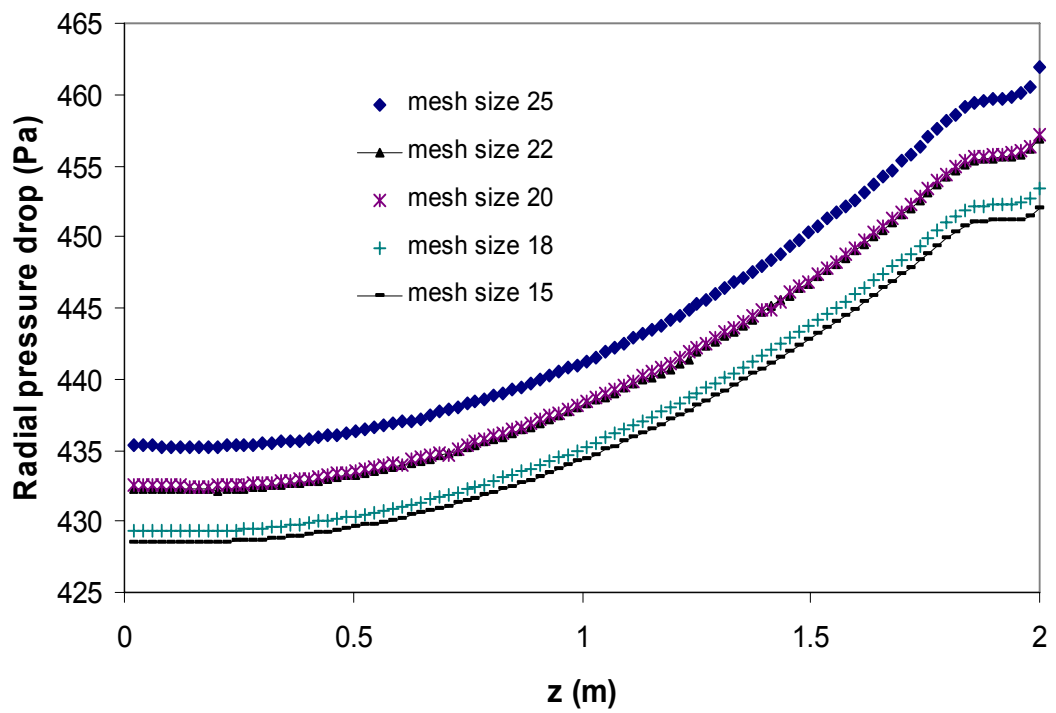
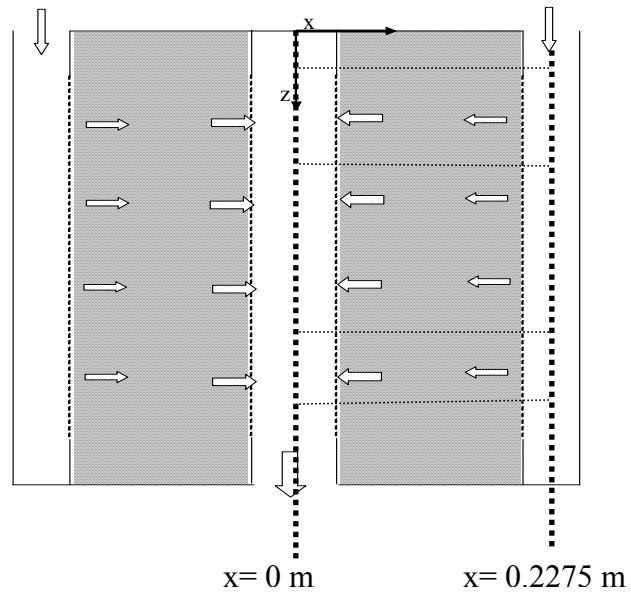


Figure 4.14: Radial pressure drop (the pressure difference between the center pipe and the annular channel) variation along bed length.

Figures 4.11-4.14 show that mesh sizes of 15 and 18 mm are the best to use. Since there is no significant difference in the results of mesh size 15 and 18 mm and to optimize the computational resources it was decided to use a mesh size 18 mm.

4.3 Analysis of the Flow Distribution in an RFBR

Figure 4.15 shows typical flow distributions in a radial flow reactor. In order to have a uniform flow distribution the gas mass flow should be divided equally over the catalyst bed height. If the mass flow is not equally divided some parts of the bed will be at minimum utilization as found by Lobanov and Skipin (1986).

The operating efficiency of a radial flow reactor largely depends on the gas stream distribution over the catalyst bed height. Non-uniform flow distribution over the bed height will affect the reaction conversion and selectivity and the temperature profile (Ponzi and Kaye, 1979; Lobanov and Skipin, 1986; Suter *et al.*, 1990). Consequently, in a catalytic process, a uniform flow distribution produces an even carbon concentration over the catalyst bed height. On the other hand, a non-uniform flow produces a non-uniform carbon concentration over the catalyst bed height. This influences the duration of the regeneration cycle for a RFBR process and disturbs the operation of the regeneration system in a RFMBR process. Moreover, in an RFMBR process the non-uniformity of the flow can contribute to the pinning phenomena since a higher radial velocity in some parts of the bed is produced.

When a non-uniform flow distribution occurs in a CP-z or a CP- π configuration, there is an increased probability of having pinned catalyst against the center pipe or initiating a cavity between the annular channel and the catalyst bed at the bottom and the top of the bed as shown in Figure 4.15b and 4.15c respectively.

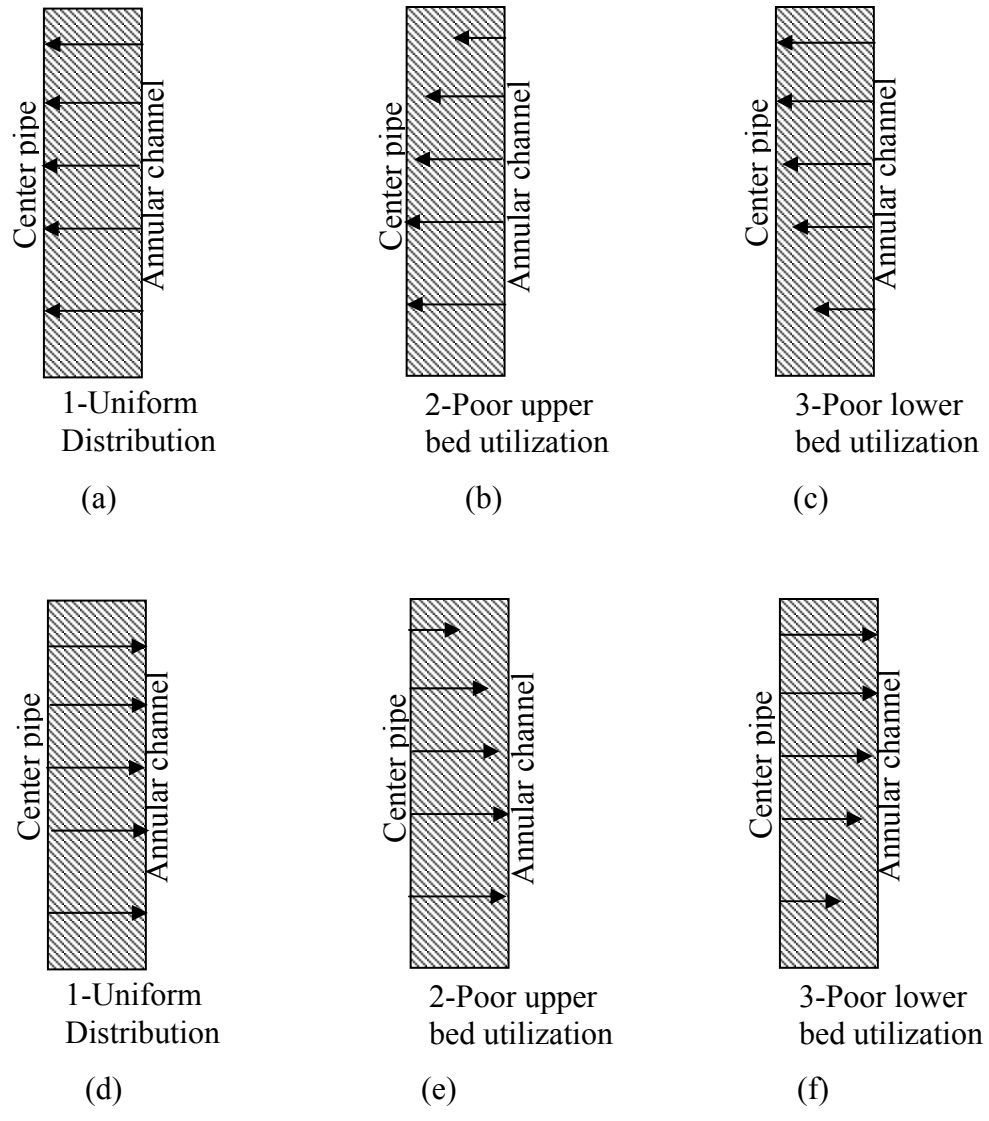


Figure 4.15: Typical flow distributions over the bed length in a radial flow reactor at the same feed flow rate for CP configurations (a-c) and for CF configurations (d-f). The arrow length represents the mass flow magnitude.

In the CF-z or CF- π configuration shown in Figure 4.15e-f, the same problem exists, but the pinning will be against the annular channel perforated wall and the cavity is between the center pipe and the catalyst bed. Since the fixed and moving beds almost have the same gas flow profile prior to the initiation of the pinning phenomena, analyzing the flow distribution in an RFBR can help in evaluating the pinning phenomena in a moving bed reactor.

Having an optimum or a poor utilization of the catalyst bed depends mainly on the pressure distribution inside the reactors. An important design criterion for the radial flow reactor is to have the radial pressure independent of the axial coordinate (Chang *et al.*, 1983). This criterion makes the gas stream equally divided over the catalyst volume as shown in Figure 4.14a for CP configurations and in Figure 4.14d for CF configurations. In other words, the uniformity criterion means achieving a uniform flow distribution in a radial flow reactor by having the pressure drop between the center pipe and the annular channel the same at any axial level.

4.3.1 Analysis the Annular Channel and Center Pipe Flow Profiles

Achieving uniform flow mainly depends on the pressure profiles in the annular channel and center pipe. Parallel pressure profiles for the two sections as in Figure 4.16 will lead to uniform flow distribution over the bed height. This pressure profile is applicable for the π -flow configurations, where the flow in the annular channel is of opposite direction to that in the center pipe.

The flow can be discharged from the annular channel and collected in the center pipe as in CP-z and CP- π configurations, or discharged from center pipe and collected in the annular channel where as in CF-z and CF- π configurations.

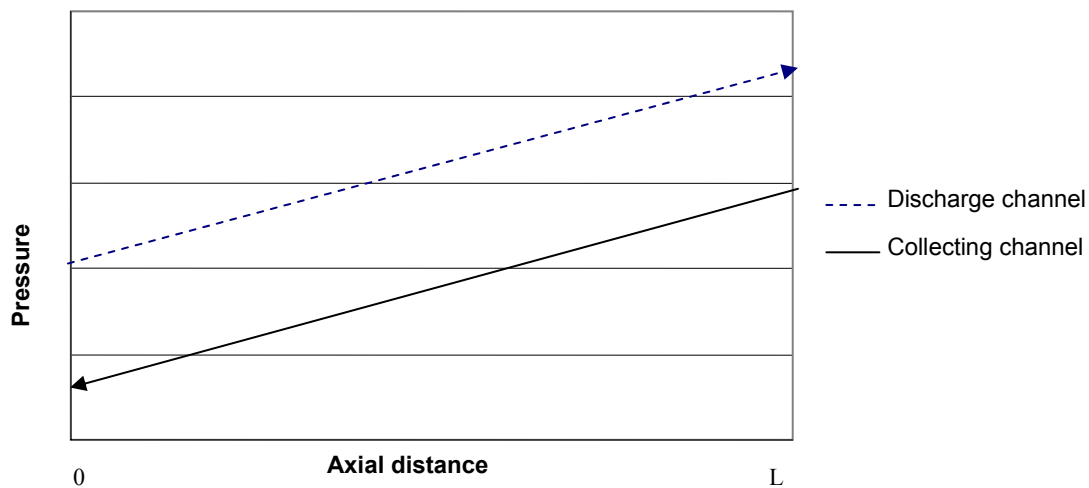
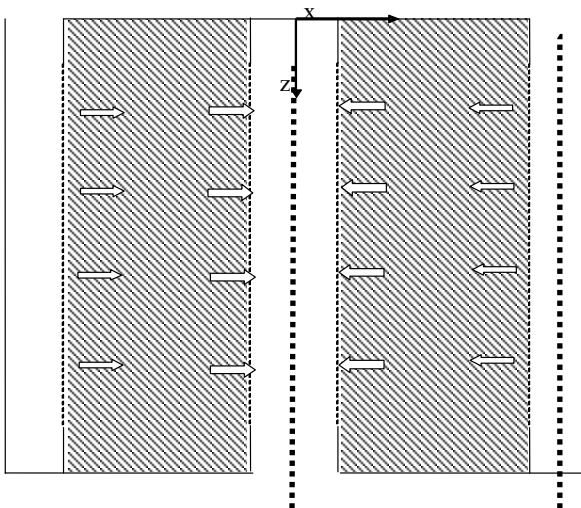


Figure 4.16: An illustration of the discharge and the collecting channels pressure profile that leads to a uniform flow distribution inside an RFBR.

In the discharge and collecting channels the gas flow rate varies axially as shown in Figures 4.3 (discharge channel) and 4.7 (collecting channel).

In previous theoretical and numerical studies, three flow equations were used to describe the flow profile in each channel. They are the Bernoulli's equation, the total energy equation and a modified momentum equation (Zuze *et al.*, 2003). Earlier investigations have shown that Bernoulli's equation gives a poor description of the motion of a gas stream with varying mass, such as in an RFBR (Genkin *et al.*, 1973). The energy equation which was used by Genkin *et al.* (1973) is too complex to be applied to a commercial reactor design. A modified momentum equation was used by Song *et al.* (1993) and Zuze *et al.* (2003). Application of the modified momentum equation depends on empirical coefficients. One of these coefficients is the momentum recovery factor which is shown in Equations 4-1 and 4-2. This factor depends on the equipment geometry and the energy change along the axial direction and can be determined experimentally (Song *et al.*, 1993). The empirical coefficients needed for using the modified momentum equation may not be available for all geometries and operating conditions. Also sometimes they cannot be determined, such as in an operated commercial reactor. Hence, using a modified momentum equation is limited by the availability of the empirical coefficients.

In this work full mass and momentum conservation equations in conjunction with porous media and porous jump models are used to describe the flow in the an RFBR. In addition, a three dimensional geometry is used to represent the effect of the cross-sectional flow area reduction toward the center pipe.

4.3.2 Predictions of the Annular and Center Pipe Pressure Profiles

The annular channel and the center pipe can be considered as perforated pipe distributors. In a perforated pipe distributor the total pressure drop is a combination of frictional pressure drop and pressure recovery due to kinetic energy or momentum changes caused by the varying mass flow as seen in Figures 4.3 (mass decreases in the annular channel) and 4.7 (mass increases in the center pipe). The equations below show the effects of friction and momentum recovery on the total pressure drop along a perforated pipe distributor (Perry and Green, 1997).

$$\Delta P = \left(\frac{4fL}{3D} - 2K \right) \frac{\rho V_i^2}{2} \quad (\text{discharging perforated pipe}) \quad (4-1)$$

$$\Delta P = \left(\frac{4fL}{3D} + 2K \right) \frac{\rho V_e^2}{2} \quad (\text{collecting perforated pipe}) \quad (4-2)$$

where ΔP is the net pressure drop over the length of the distributor, f is the fanning friction factor, D is the pipe diameter, V_i is the inlet velocity for the discharge pipe, V_e is the exit velocity for the collecting pipe and K is the momentum recovery factor that depends on the piping configuration.

The first term in Equations 4-1 and 4-2 is the frictional pressure drop and the second term is the inertial (momentum) pressure recovery. In the collecting pipe both frictional and inertial effects cause a pressure drop, since the mass flow increases downstream. Therefore the pressure always decreases along the length of the pipe.

In the discharge pipe the frictional and inertial effects oppose each other. Friction causes a pressure drop and since the mass flow decreases downstream the momentum recovery causes a pressure rise. Therefore the pressure may decrease or

increase along the pipe length depending on the dominating term. When the friction is the dominating term, the pressure will decrease along the pipe length. Friction can be the dominating term in long pipe and small diameter pipe as seen from Equation 4-1. When the momentum recovery is the dominating term, the pressure will increase along the pipe length. The momentum recovery can be the dominating term in a short pipe and a large diameter pipe as can be seen from Equation 4-1

At high flow rates the inertial effects may dominate the frictional effects in determining the pressure profile along the perforated pipe, unless the length between the pipe holes is large (Perry and Green, 1997). Therefore at a high flow rate and a small length between the pipe holes, which is true for the most of the application of the radial flow reactor, Equations 4-1 and 4-2 will be reduced to:

$$\Delta P = -2K \frac{\rho V_i^2}{2} \quad (\text{discharging perforated pipe}) \quad (4-3)$$

$$\Delta P = 2K \frac{\rho V_e^2}{2} \quad (\text{collecting perforated pipe}) \quad (4-4)$$

It can be concluded from Equations 4-3 and 4-4 that at a constant density the pressure profile in perforated pipe mainly depends on the momentum recovery factor and the flow rate. Although Equations 4-1- 4-4 are not used in the present CFD model, their concept is used to better understand and analyze the pressure profiles in the annular channel and the center pipe and to get a prediction for some parametric studies for any RFBR numerical model.

4.3.3 The Reactor Dimensions and Operating Conditions

The reactor dimensions and operating conditions used to study the flow distribution are the same as the ones shown in Tables 4.1 and 4.2, except that the center pipe porosity used in the flow distribution analysis is 0.05. At a low center pipe porosity there will be no significant flow maldistribution in all four configurations. Since a center pipe porosity of 0.012 is the lowest value used in this work and the most difficult one to obtain a converged solution for, it was used to select the proper mesh size.

Based on the reactor geometry and the operating conditions the Re for the annular channel, the center pipe and the bed section are 17,000, 37,000 and 15 respectively. Turbulent flow exists in the annular channel and the center pipe and laminar flow exists in the bed. Therefore the simulation is done with a turbulent model (k - ϵ) limited to the annular channel and center pipe.

4.3.4 Simulation Results for CP-z Configuration

Figures 4.17-4.20 show the flow profile for the CP-z configuration RFBR. Figure 4.17 shows the axial static pressure in the annular channel and center pipe. The pressure in the annular channel is almost constant due to the opposite effects of friction and momentum recovery. The annular channel pressure rise is less than 1 Pa. This indicates that both friction and momentum recovery effects are almost the same in magnitude but in opposite direction. In the center pipe (collecting channel) higher pressure drop occurs, since both friction and momentum recovery act in the same direction. After the perforated section where only friction contributes to the pressure drop, the pressure remains constant.

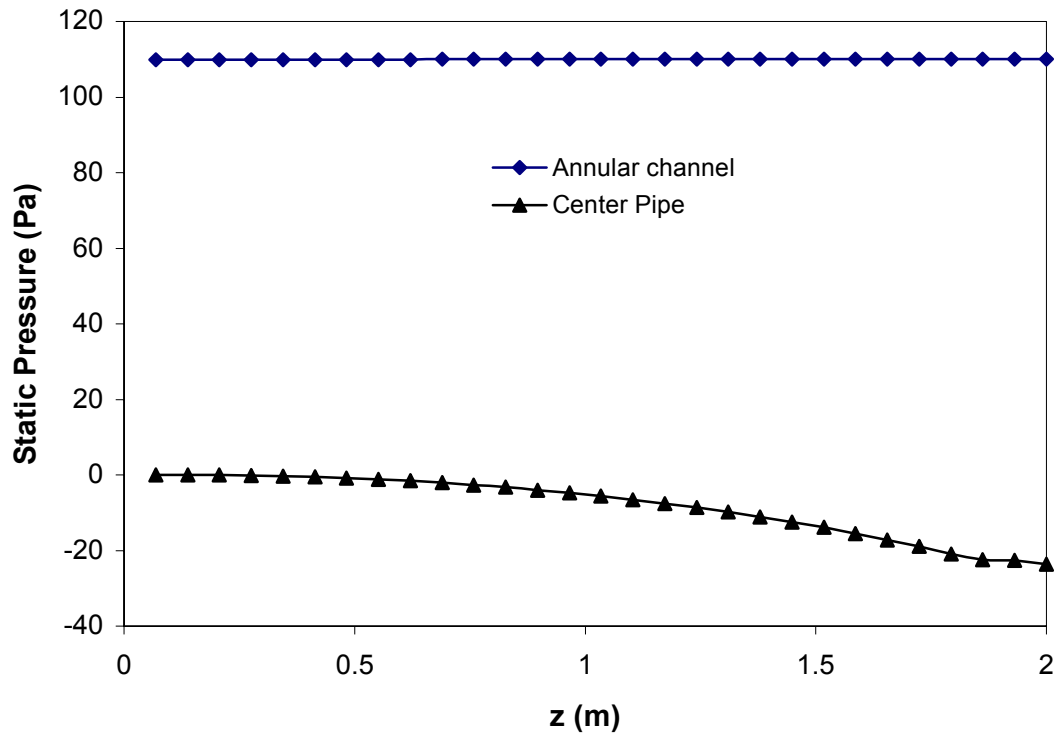
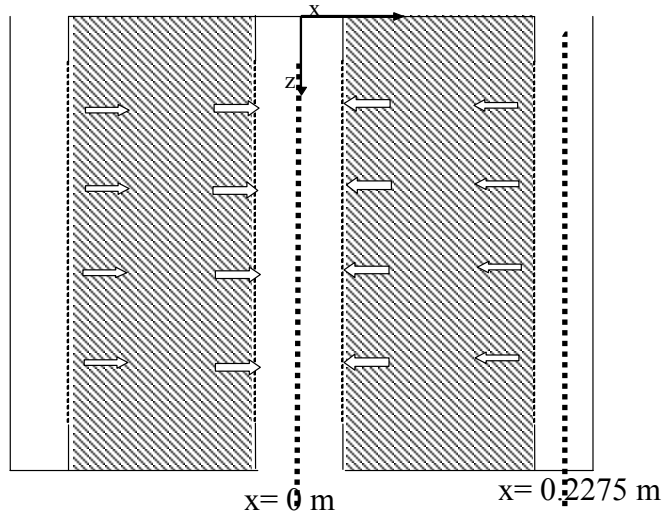


Figure 4.17: The axial static pressure profile in the annular channel and the center pipe of a CP-z RFBR.

This indicates that the friction has less effect on the center pipe pressure drop. This high pressure drop affects the flow distribution inside the reactor. Since the pressure difference between the annular channel and the center pipe is very high at the bottom of the bed, the mass flow will be higher at the bottom which leads to poor utilization of the upper section of the bed. Figure 4.18 shows that the bed radial velocity at the bottom is higher than that at the top. The flow distribution in this case is the same as that shown in Figure 4.15b. To solve this problem, the pressure drop in the center pipe should be lowered and this can be done by increasing its diameter. This will reduce the velocity inside the pipe and lower the effect of both friction and momentum recovery as can be seen from Equation 4-2.

Figure 4.19 shows a plot of the velocity along the axial direction in the annular channel and center pipe. The annular channel velocity starts with no change in the top seal section and then it decreases to zero at the end of the perforated section. The velocity in the center pipe starts to increase at the beginning of the perforated section and it continues to increase up to the end of perforated section.

Figure 4-20 shows the axial velocity along the reactor radial direction. A symmetrical profile is found. This is because of a uniform inlet distribution. This profile may be impacted by the orientation of the reactor inlet section above the bed. A parabolic profile in the center pipe is caused by the pushing act of the radial forces. A flat peak on the annular channel profile is caused by the pulling act of the radial forces. No axial velocity in the bed section which is a desired condition to eliminate the maldistribution in the radial flow reactor.

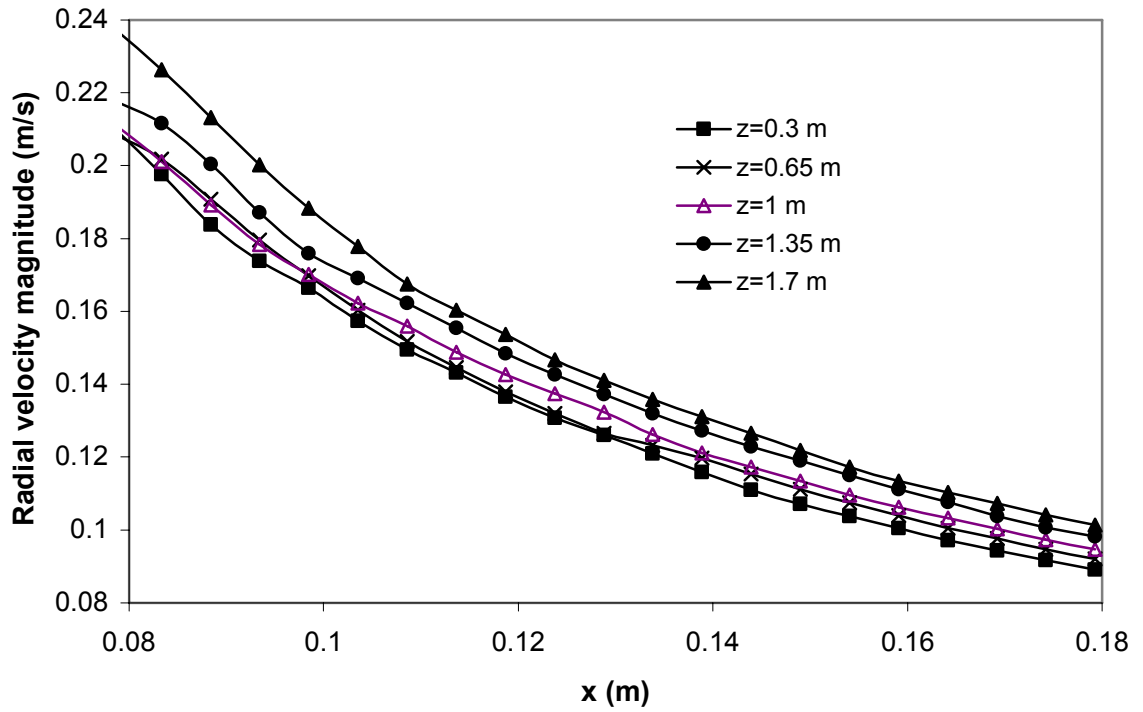
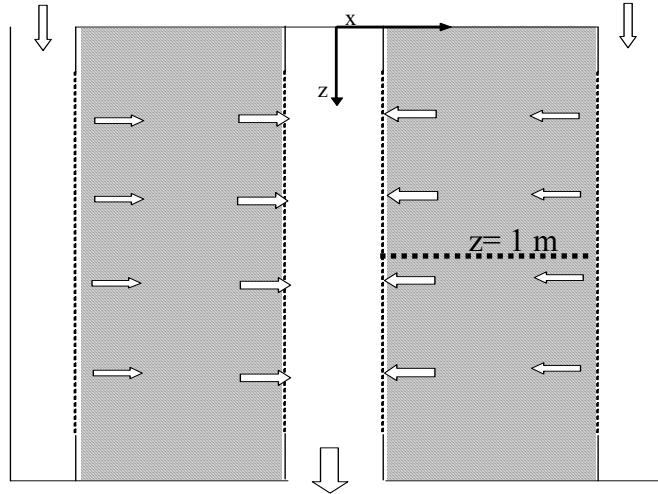


Figure 4.18: CP-z type bed radial velocity profiles along the bed length, at x-z plane of the bed.

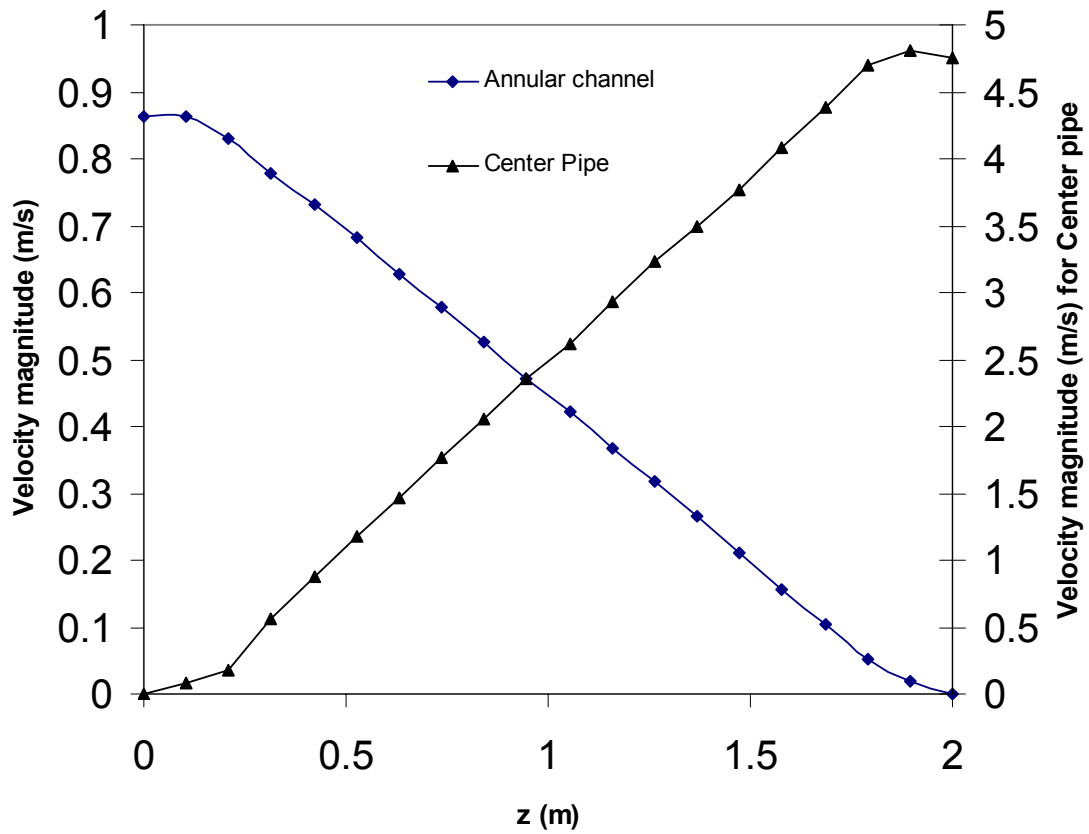
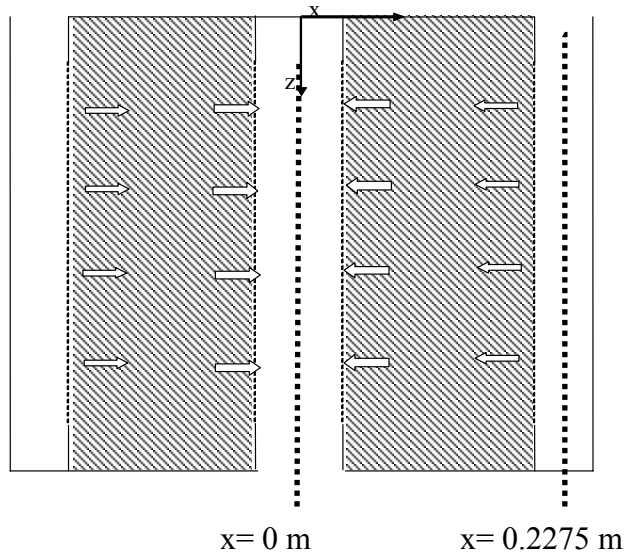


Figure 4.19: CP-z type annular channel and center pipe velocity profiles, at the center of x-z plane of the channels.

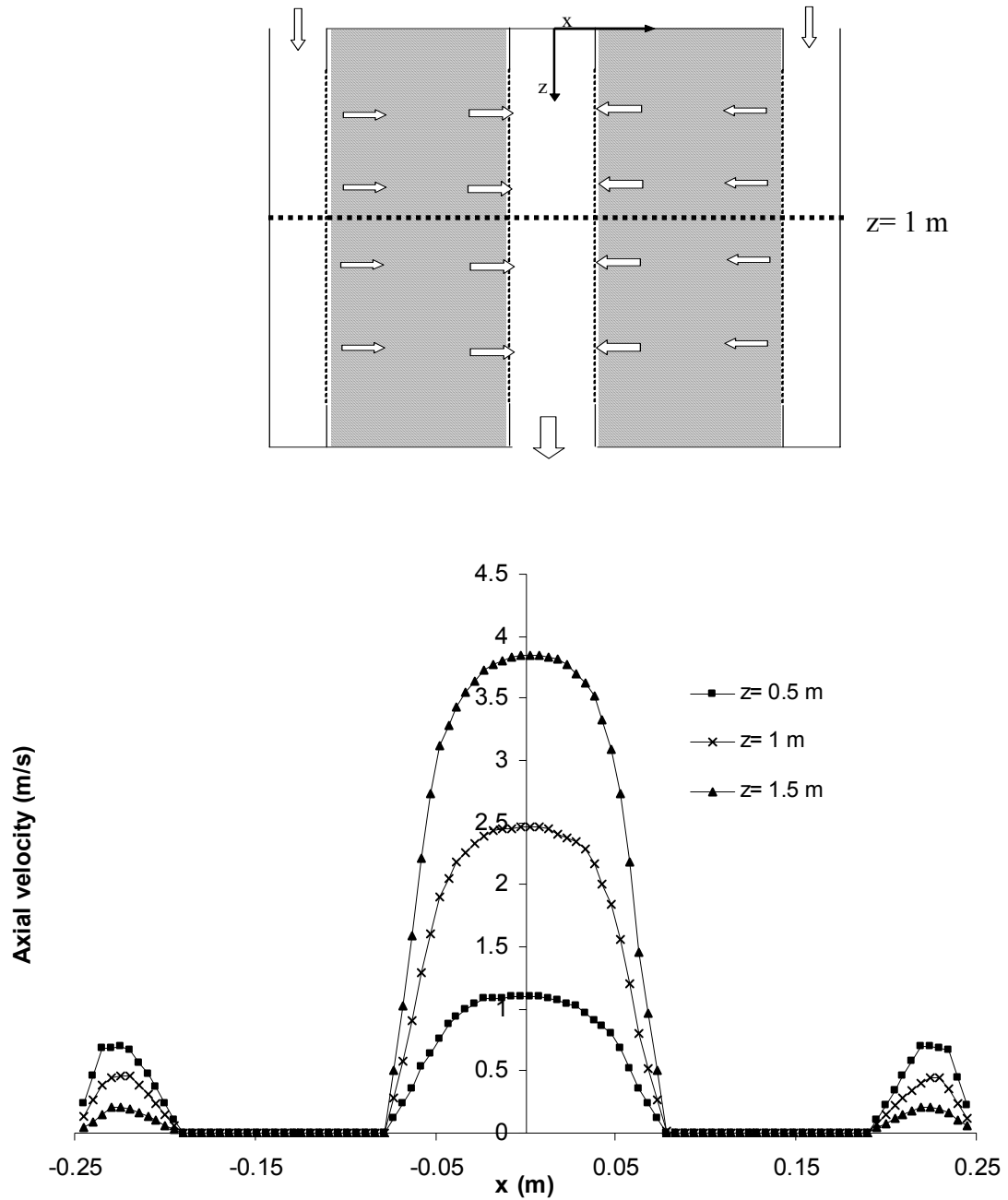


Figure 4.20: A CP-z type axial velocity profile along the reactor radial direction at different axial levels.

4.3.5 Simulation Results for CP- π Configuration

Figures 4.21-4.24 show the flow profiles for the CP- π configuration RFBR. Figure 4.21 shows the pressure profiles in the annular channel and the center pipe. The CP- π annular pressure profile is identical to that of a CP-z configuration. The center pipe pressure profile is also identical to that of a CP-z configuration, except that it is reversed. The highest difference between the annular channel and the center pipe pressures occurs at the top of the bed. Since the pressure difference between the annular channel and the center pipe is very high at the top of the bed, the mass flow will be higher at the top which leads to poor utilization of the lower section of the bed. Figure 4.22 shows the variation of the radial velocity along the bed length. Higher velocity exists at the top than at the bottom of the bed. The flow distribution in this case is the same as that shown in Figure 4.15c.

Figure 4.23 shows the annular channel and the center pipe velocity along the axial direction. Figure 4.24 shows the axial velocity along the reactor radial direction. They are similar to the profiles in a CP-z configuration, except that the flow in center pipe is reversed.

4.3.6 Simulation Results for CF- π Configuration

Figures 4.25-4.28 show the flow profile for the CF- π configuration RFBR. Figure 4.25 shows the axial static pressure in the annular channel and center pipe. In this case the center pipe is the discharge channel and the annular channel is the collecting channel. A significant pressure rise occurs in the center pipe, which indicates that the inertial effect is dominating the frictional effect. The pressure drop in the annular channel is not significant.

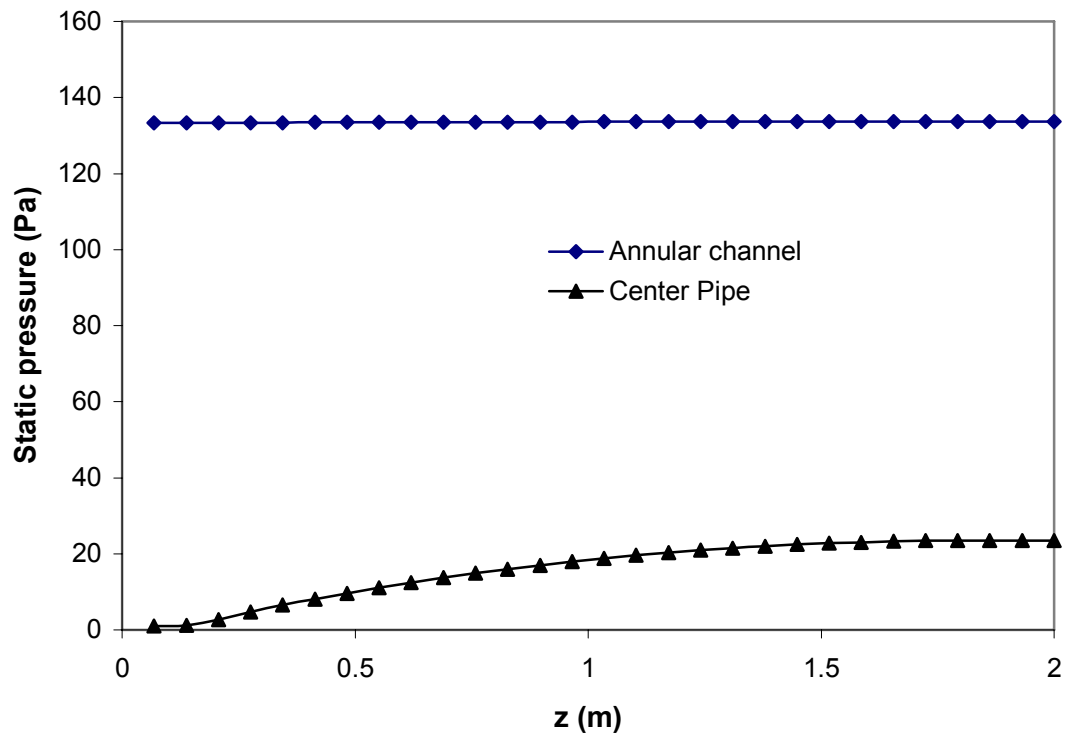
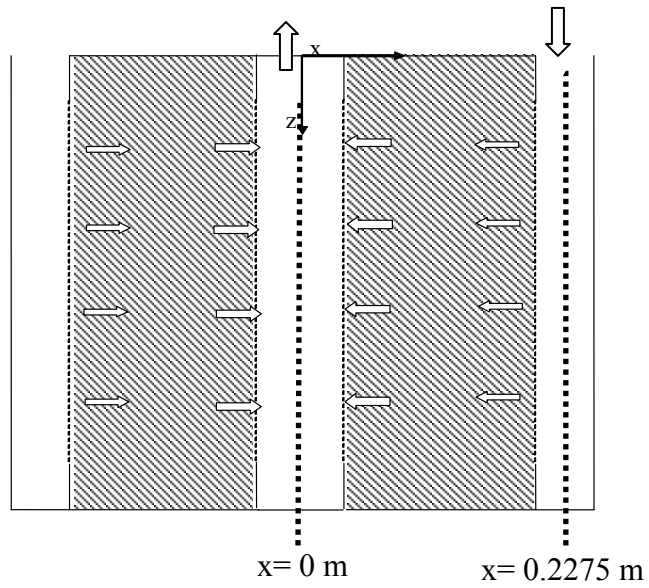


Figure 4.21: The axial static pressure profile in the annular channel and the center pipe of a CP- π RFBR.

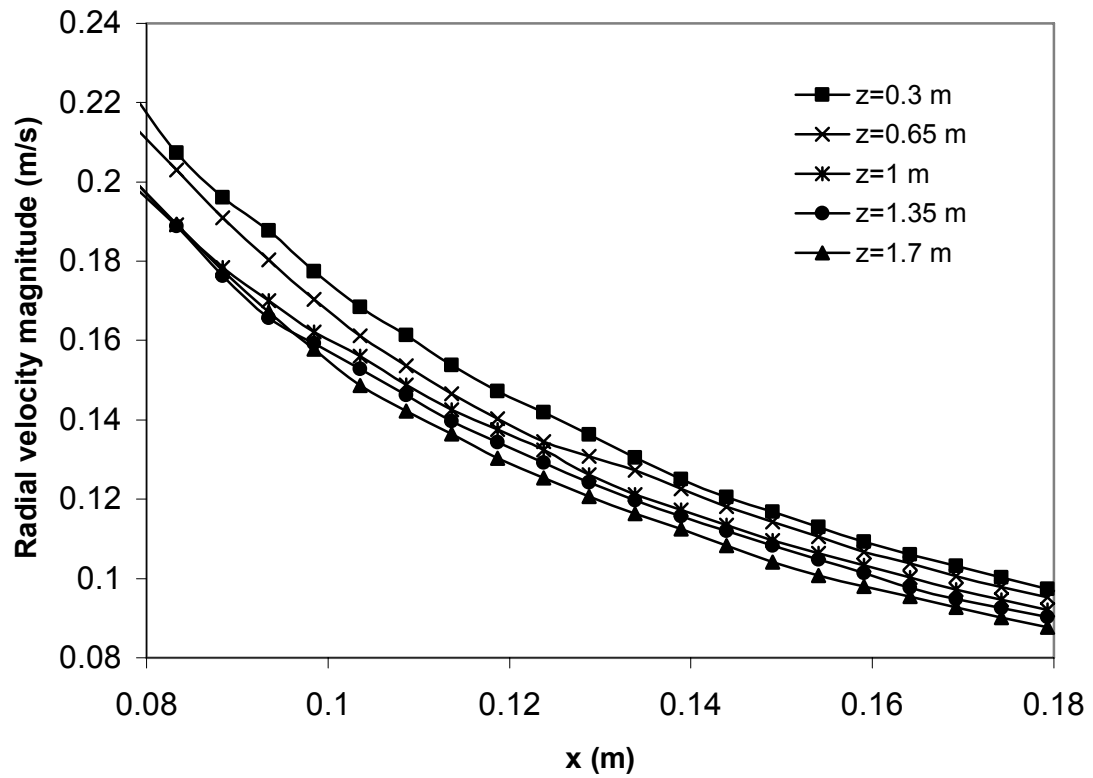
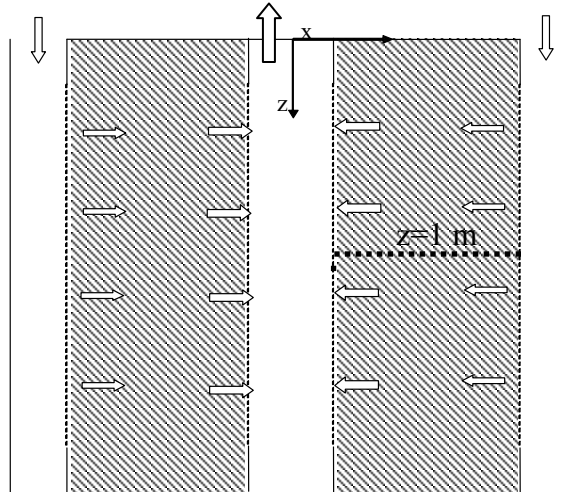


Figure 4.22: CP- π type bed radial velocity profiles along the bed length, at x-z plane of the bed.

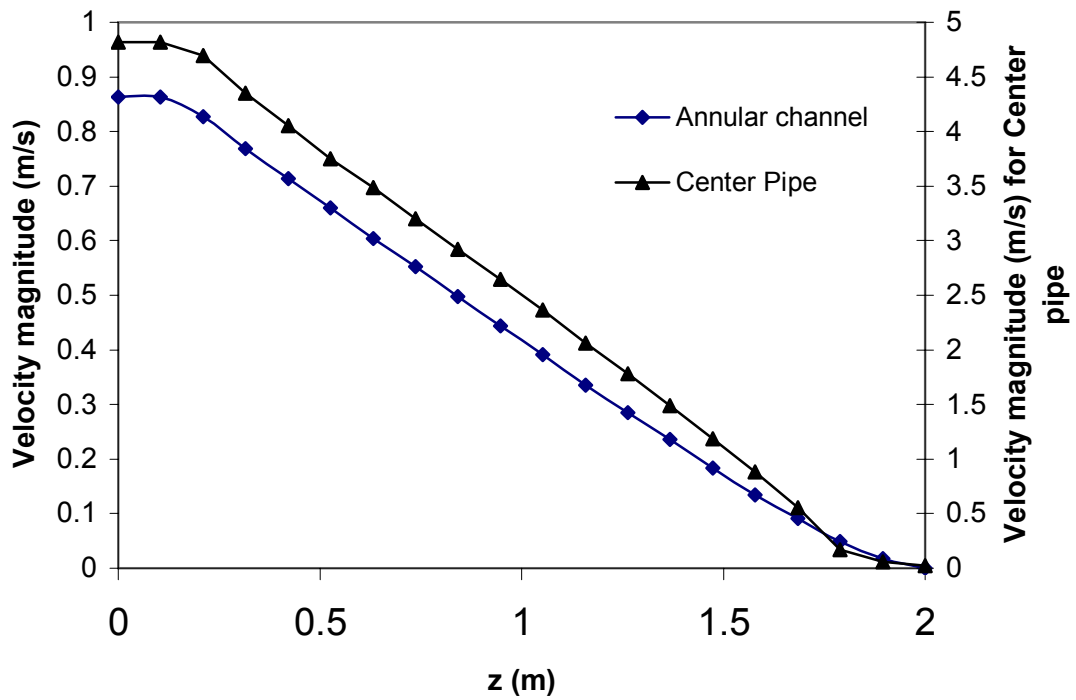
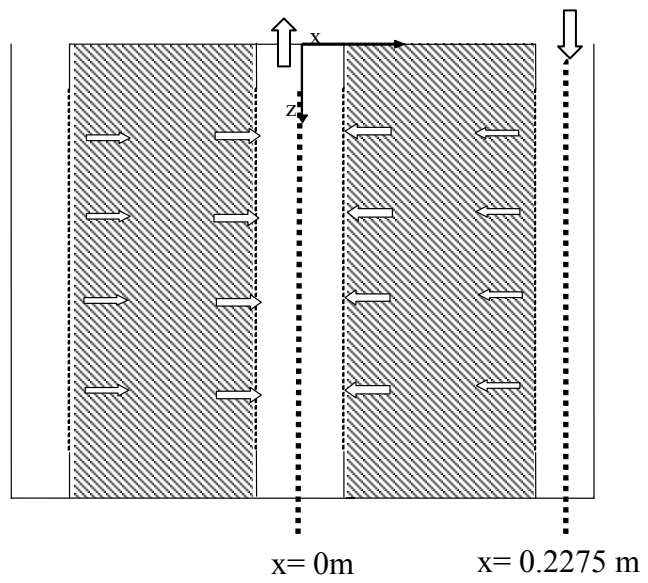


Figure 4.23: CP- π type annular channel and center pipe velocity profiles, at the center of the x-z plane of the channels.

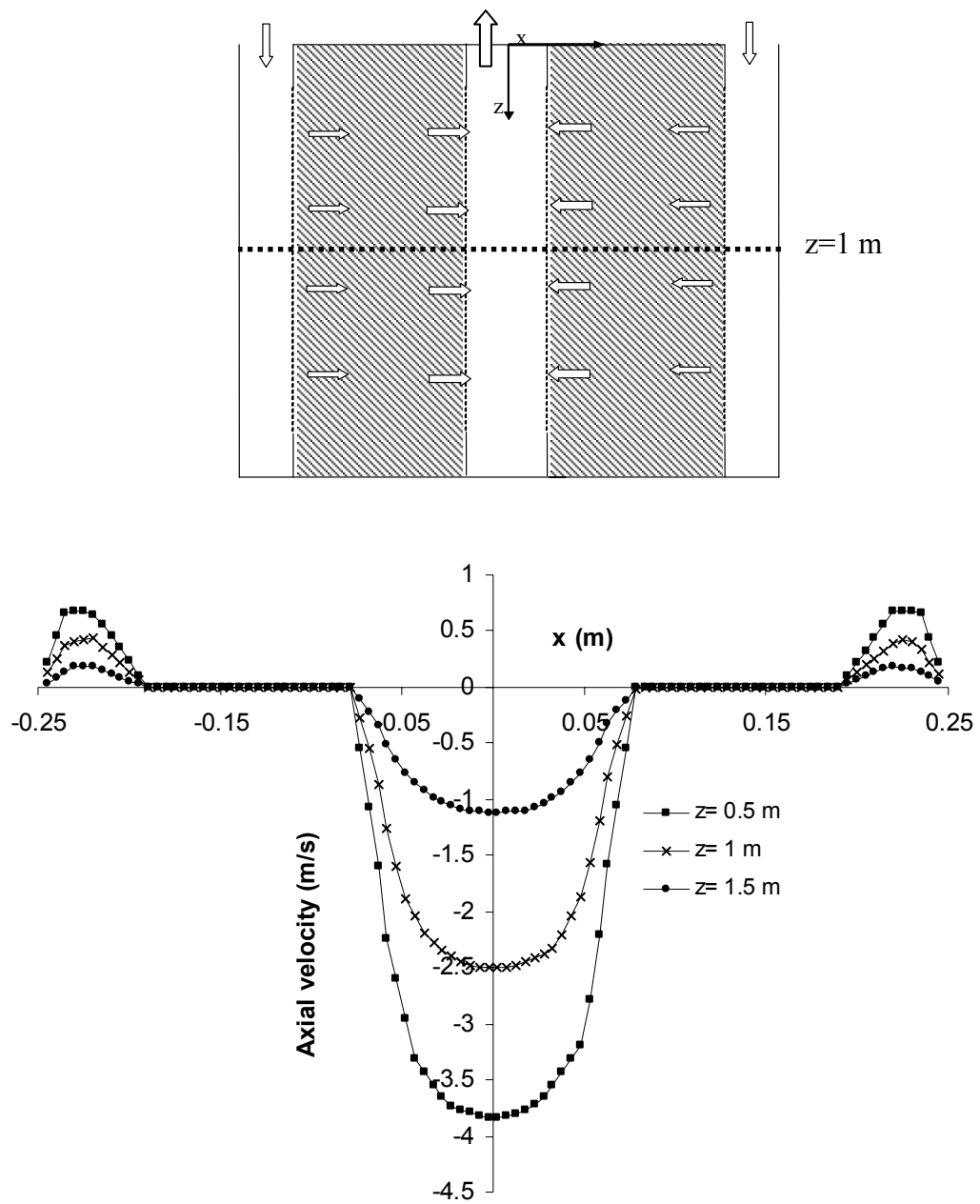


Figure 4.24: CP- π type axial velocity profile along the reactor radial direction.

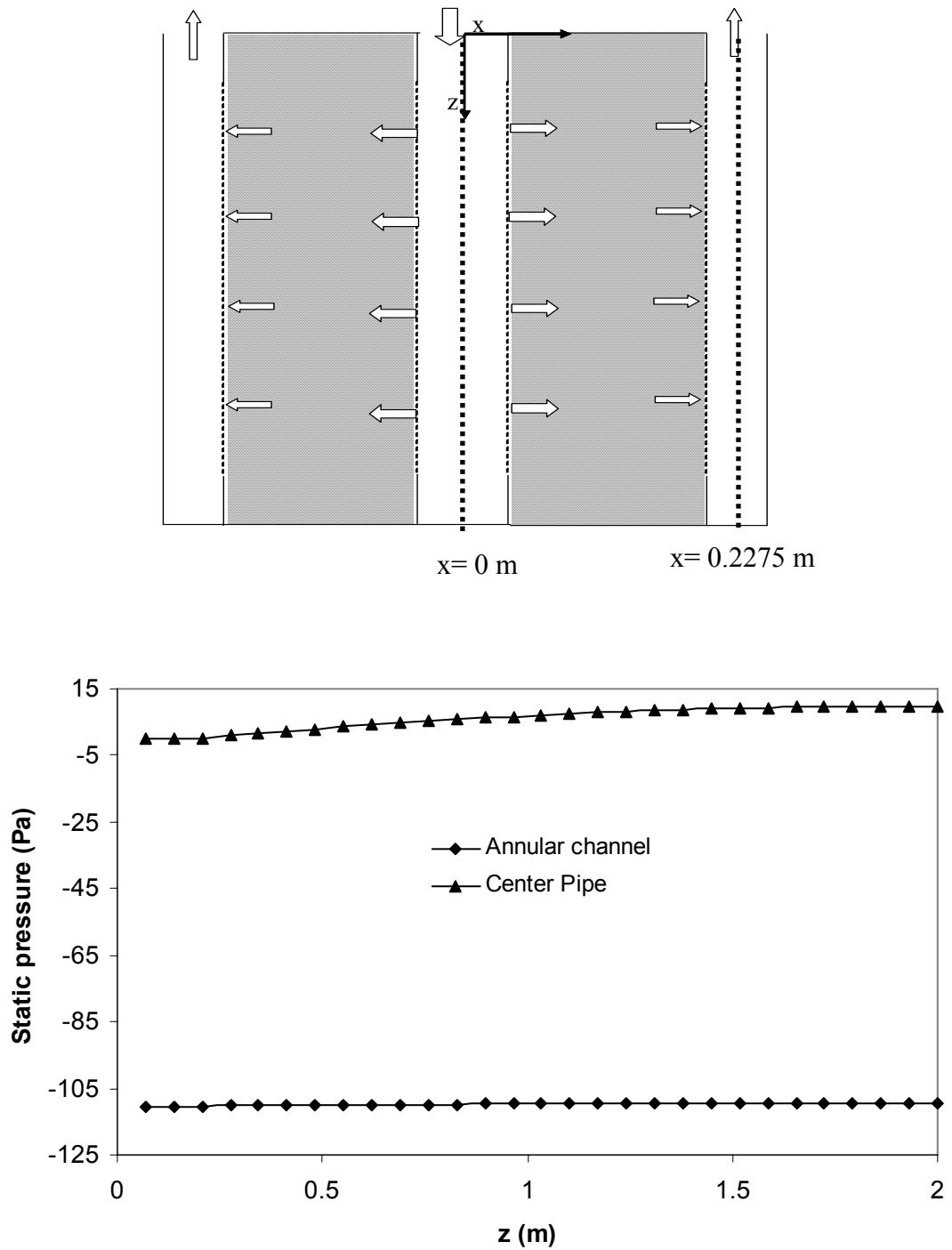


Figure 4.25: The axial static pressure profile in the annular channel and the center pipe of a CF- π RFBR.

The difference between the pressure profiles for CF and CP configurations can be explained using Equations 4-3 and 4-4. Since the cross-sectional area of the annulus is five times that for the center pipe, the velocity in the annulus is much lower than that in the center pipe. Hence the pressure rise in the annular channel for the CP configuration is much lower than the pressure rise in the center pipe for the CF configuration. Also the pressure drop in the annular channel for a CF configuration is much lower than the pressure drop in the center pipe for a CP configuration.

Figure 4.25 shows also that the pressure difference between the annulus and the center pipe is higher at the reactor bottom. Despite that the annulus and the center pipe pressure profiles are closer to a parallel profile than that for CP configurations. As a result of that, the CF- π configuration has a small difference between the radial velocity along the bed length as shown in Figure 4.26.

Figure 4.27 shows the annular channel and center pipe velocity profile along the axial direction. The center pipe velocity starts with no change in the top seal section and then it decreases to zero at the end of the perforated section. The velocity in the annular channel starts to increase at the beginning of the perforated section and it continues to increase up to the end of perforated section. Both profiles have the same slope which indicates better flow distribution.

Figure 4-28 shows the axial velocity profile along the reactor radial direction. This profile is opposite to that of a CP configuration. A flat velocity profile in the center pipe is caused by the pulling act of the radial forces. An almost sharp peak in the annular channel profile is caused by the pushing act of the radial forces.

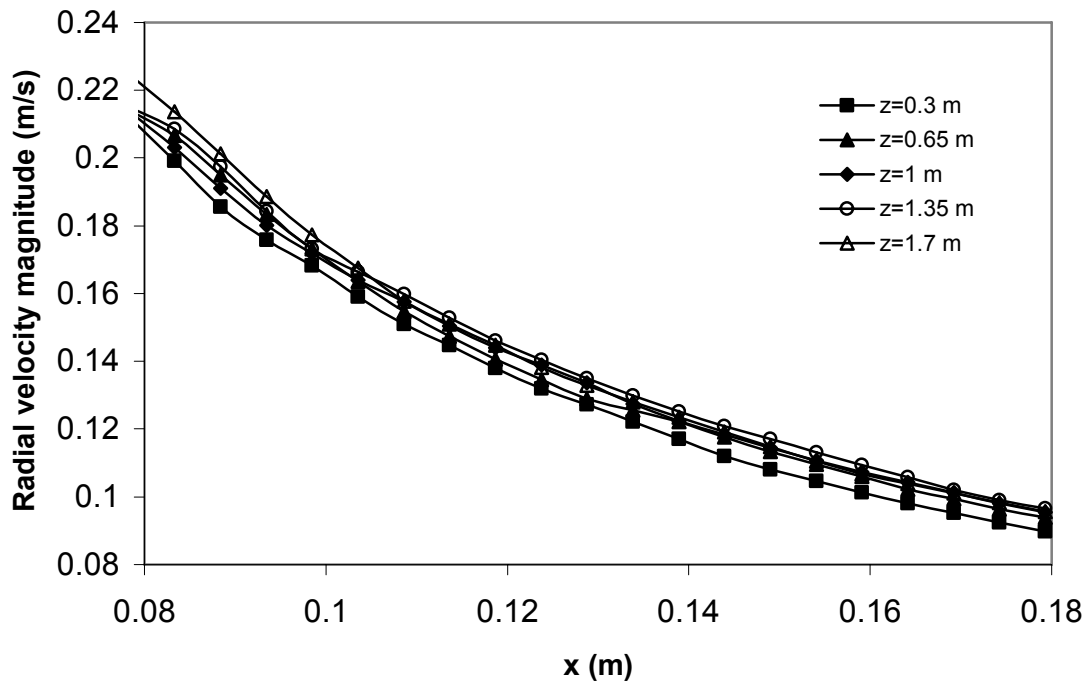
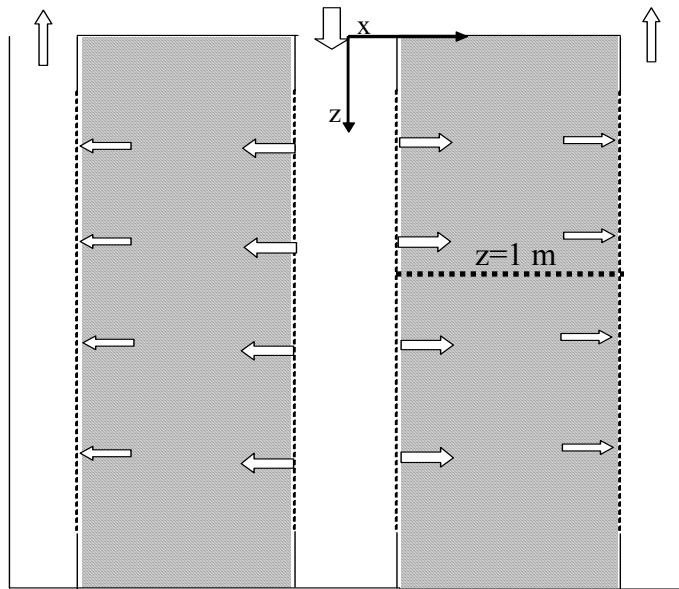


Figure 4.26: CF- π type bed radial velocity profiles along the bed length, in an x-z plane of the bed.

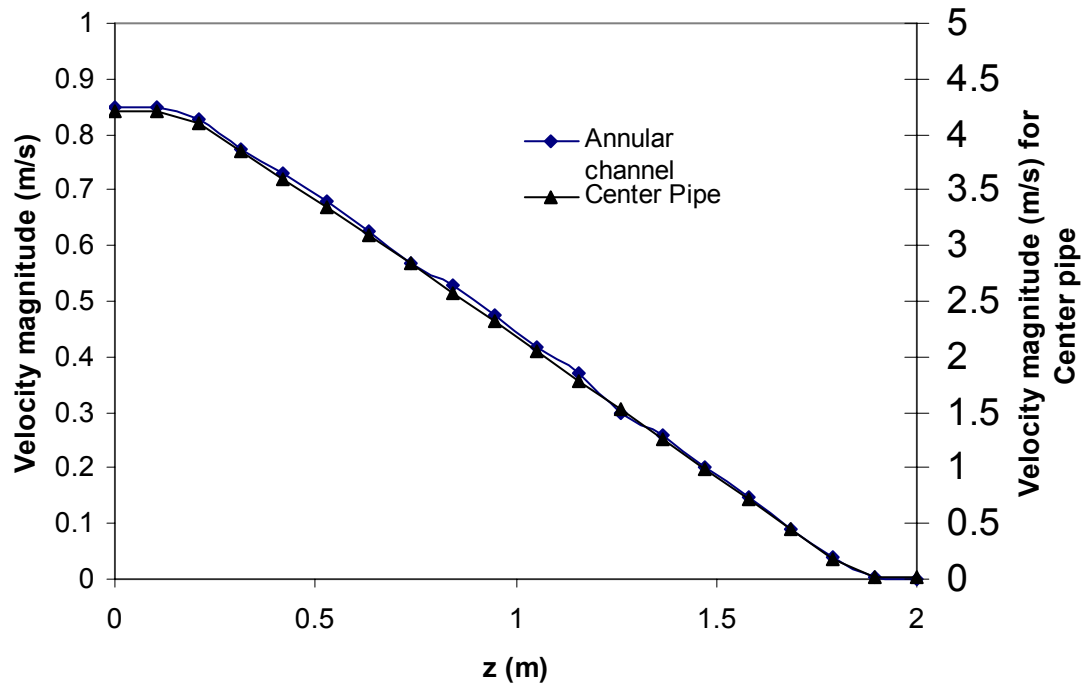
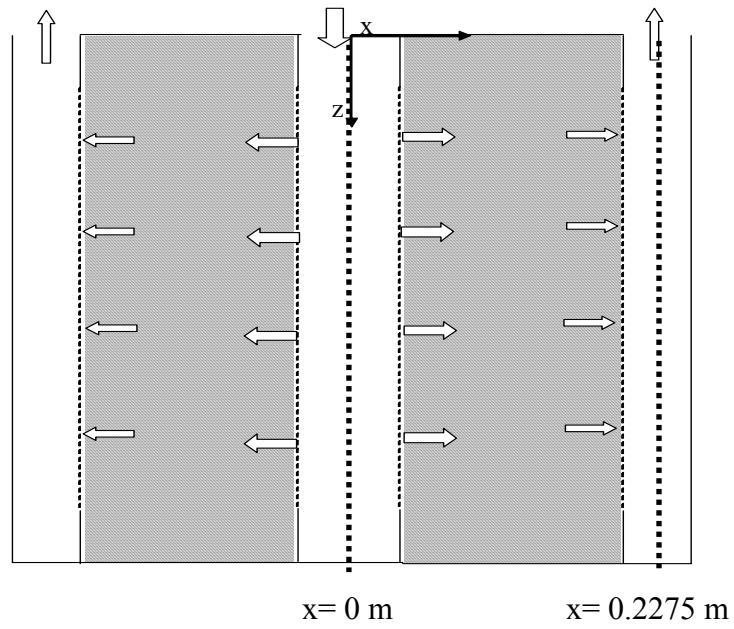


Figure 4.27: CF- π type annular channel and center pipe velocity profiles, at the center of an x-z plane of the channels.

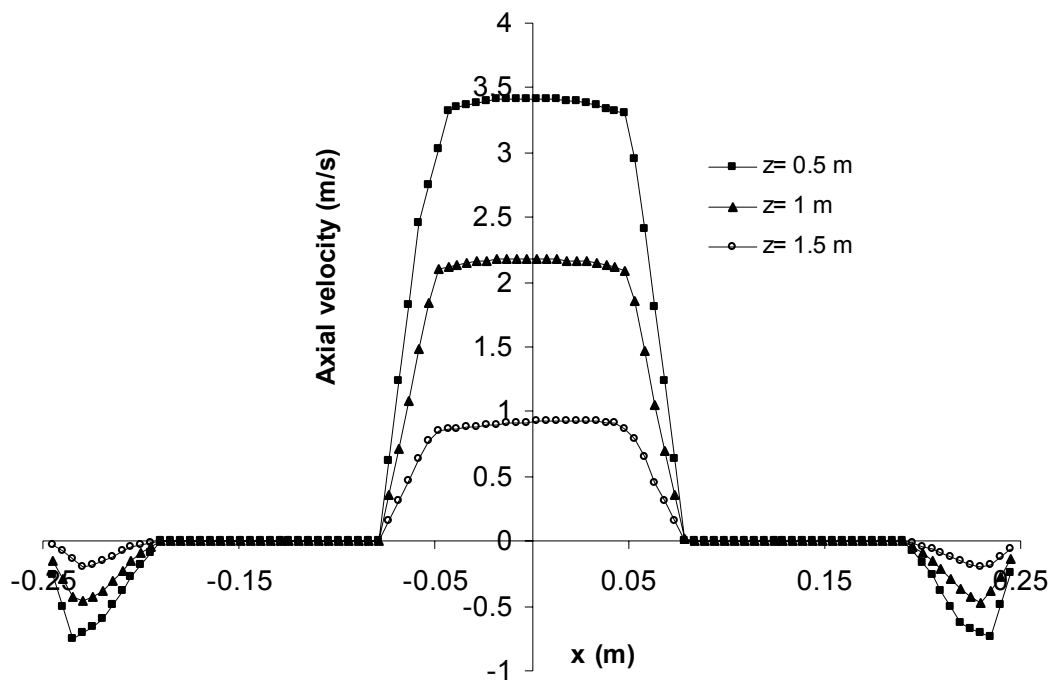
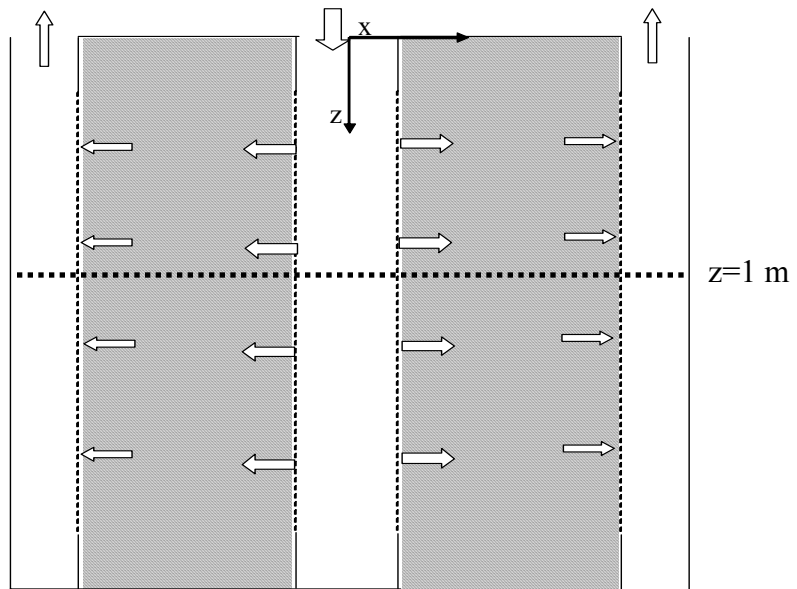


Figure 4.28: CF- π type axial velocity profile along the reactor radial direction.

No significant axial velocity is observed in the bed section which is a desired condition to eliminate the maldistribution in the radial flow reactor.

4.3.7 Simulation Results for CF-z Configuration

Figures 4.29-4.32 show the flow profiles of a CF-z configuration RFBR. The profiles are similar to those of a CF- π configuration except that the center pipe and the annular channel have the same flow direction. This is shown in Figure 4.31. Figures 4.29 and 4.30 are almost identical to the plots in Figures 4.25 and 4.26. The CF-z and CF- π configurations give also identical results for the axial velocity profile shown in Figures 4.28 and 4.32, except that the flow in the annular channel is reversed.

4.3.8. Uniformity Analysis for the Four Configurations

From the previous results it was seen that each configuration of a radial flow reactor gives a different flow profile. One important notice was that the radial velocities in CF configurations are much closer to each other than that for CP configuration as shown in Figures 4.18, 4.22, 4.26 and 4.30. This difference in the radial velocity profiles is due to the unique radial pressure drop in each configuration. In this analysis, the uniformity criterion suggested by Chang *et al.*, (1983) is used. In a uniform flow distribution, the pressure drop between the annular channel and center pipe is the same along the bed height. Figure 4.33 shows the radial pressure drop along the bed height for the four configurations. In all four configurations, the radial pressure drop profile shows dependency on the axial position, which is a deviation from uniformity.

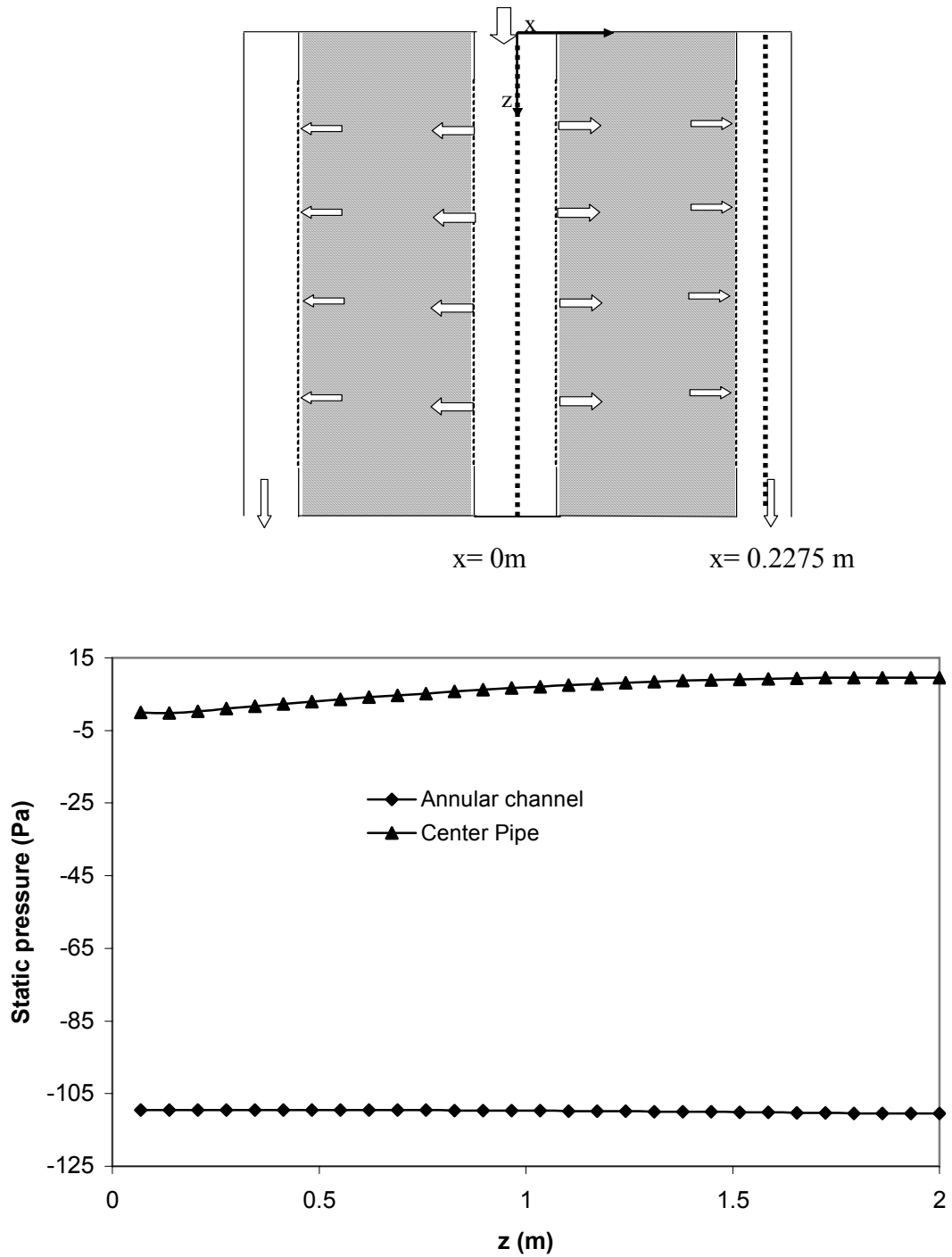


Figure 4.29: The axial static pressure profile in the annular channel and the center pipe of a CF-z RFBR.

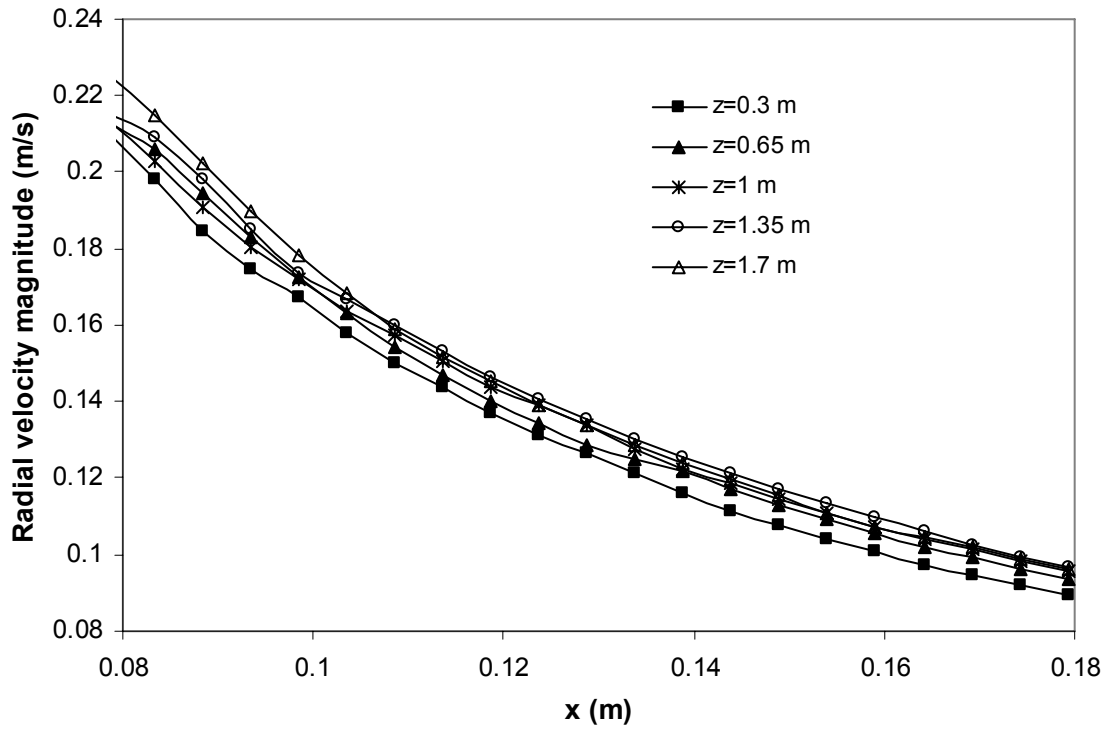
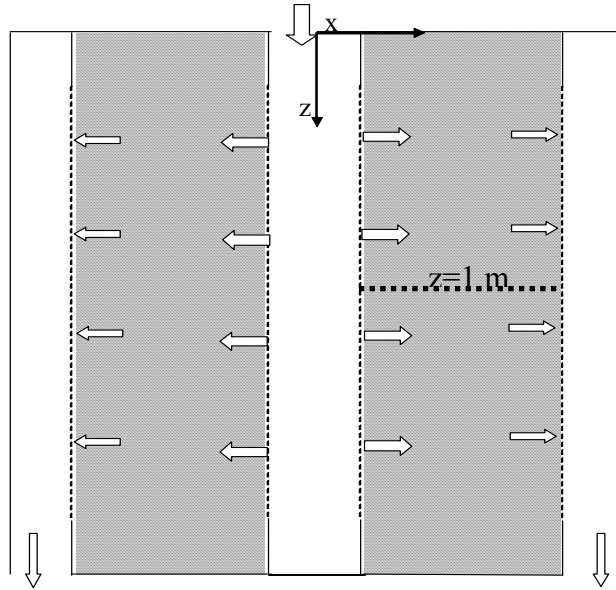


Figure 4.30: CF-z type bed radial velocity profiles along the bed length, at an x - z plane of the bed.

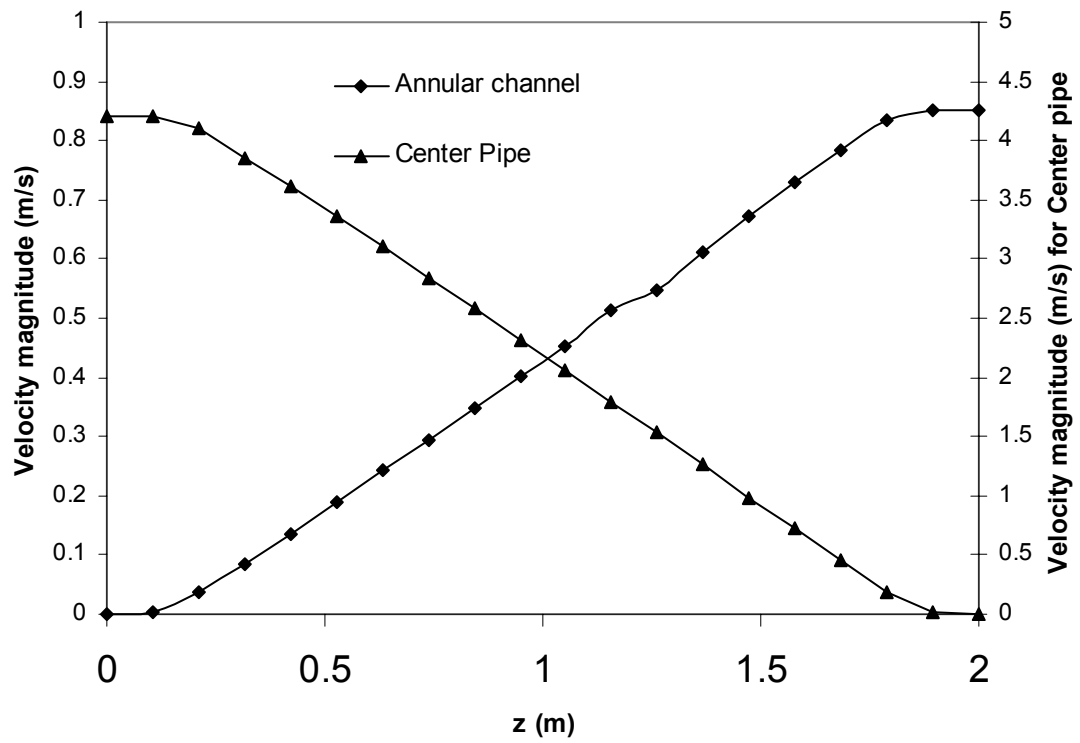
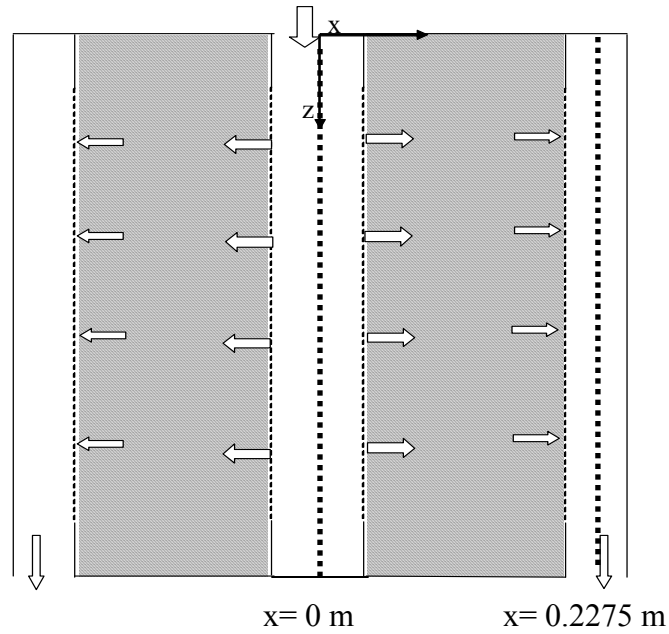


Figure 4.31: CF-z type annular channel and center pipe velocity profiles, at the center of an x - z plane of the channels.

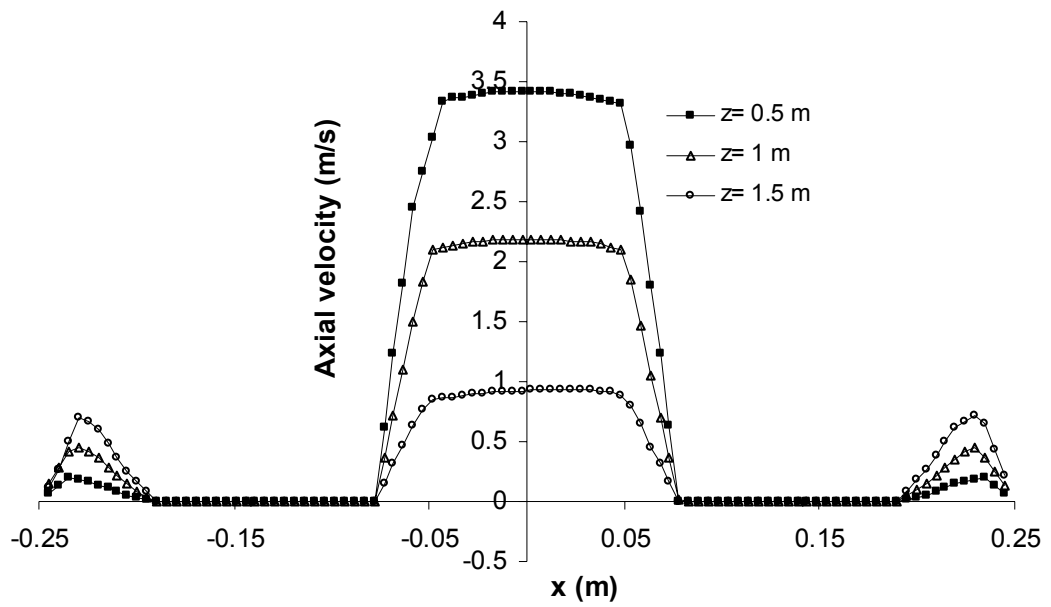
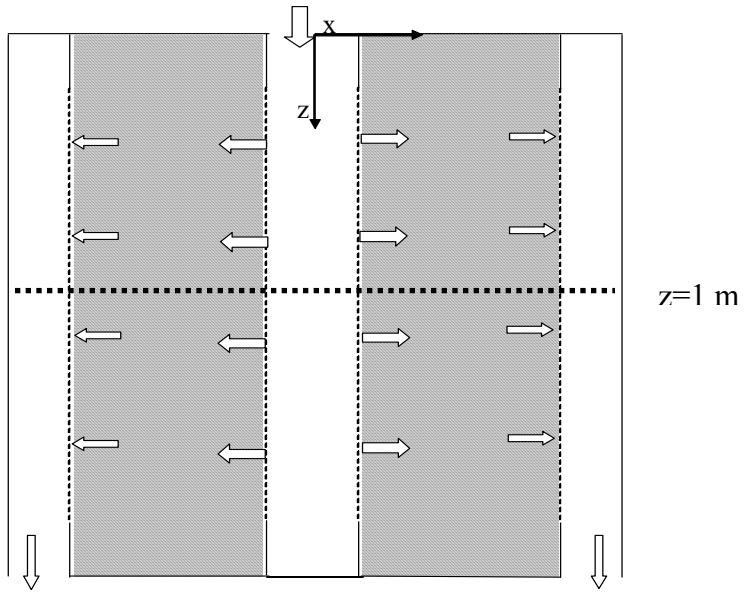


Figure 4.32: CF-z type axial velocity profile along the reactor radial direction.

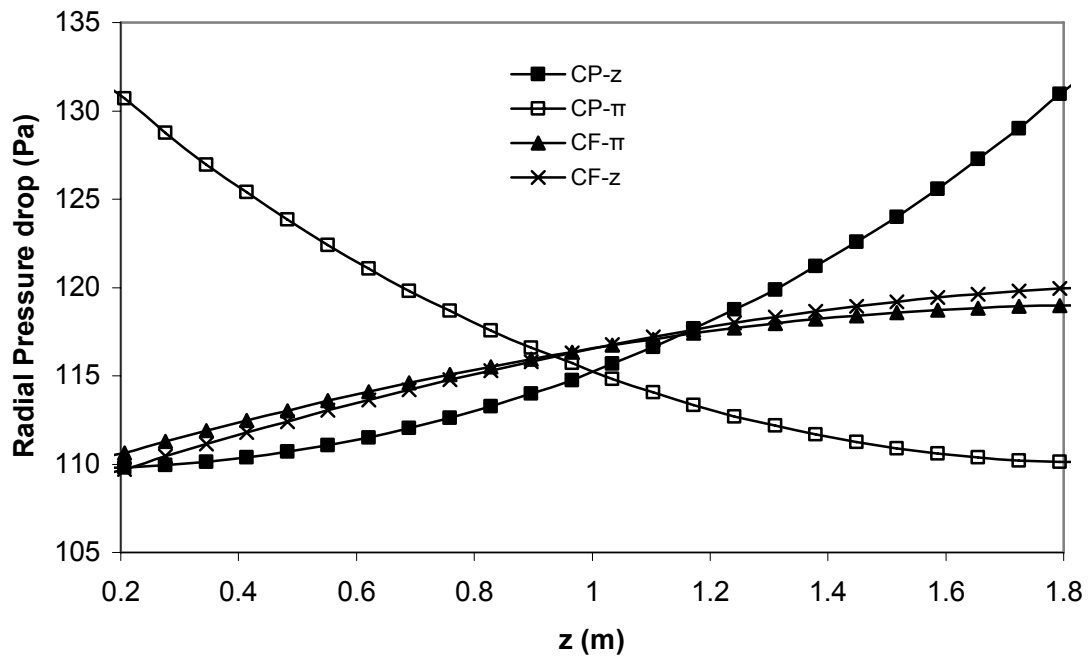
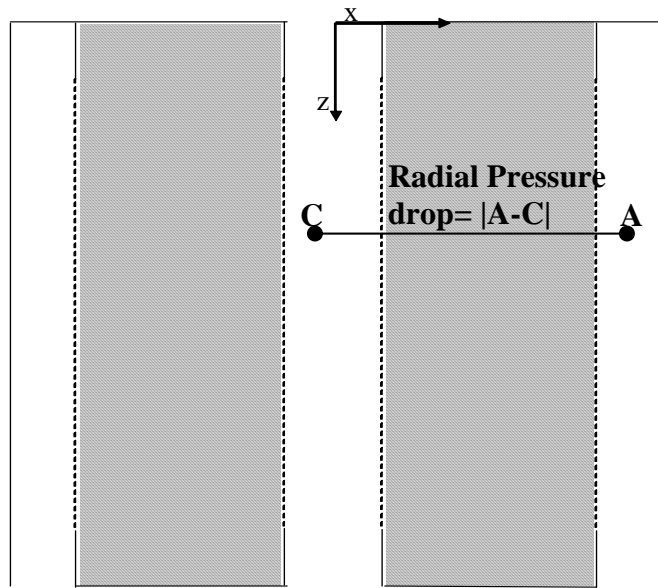


Figure 4.33: Radial pressure drop variations along the perforated section length of the bed.

To quantify the deviation from the uniformity and have one basis for the four configurations for comparison, the radial pressure drop for each configuration was normalized by dividing it by the maximum radial pressure drop. Figure 4.33 shows that CP-z, CF-z and CF- π , have the maximum radial pressure drop at the bottom of the bed while CP- π has it at the top of the bed.

Figure 4.34 shows the deviation of each configuration from the uniform flow. The normalized radial pressure drop for the uniform flow equals one at any axial position. From this figure it seems that CF- π is the best configuration which is closest to the uniform line. The second best is the CF-z. CP-z and CP- π show almost the same deviation from the uniformity. They have the lowest flow uniformity. Table 4.3 shows the deviation from the uniform flow in quantitative representation. Changing the configuration from CP-z to CF- π will improve the uniformity by a factor of 2.3.

Table 4.3: Maximum deviation from the uniform flow for the four radial flow configurations.

Radial flow configuration	Maximum deviation from the uniform line
CP-z	0.16
CP- π	0.16
CF- π	0.07
CF-z	0.09

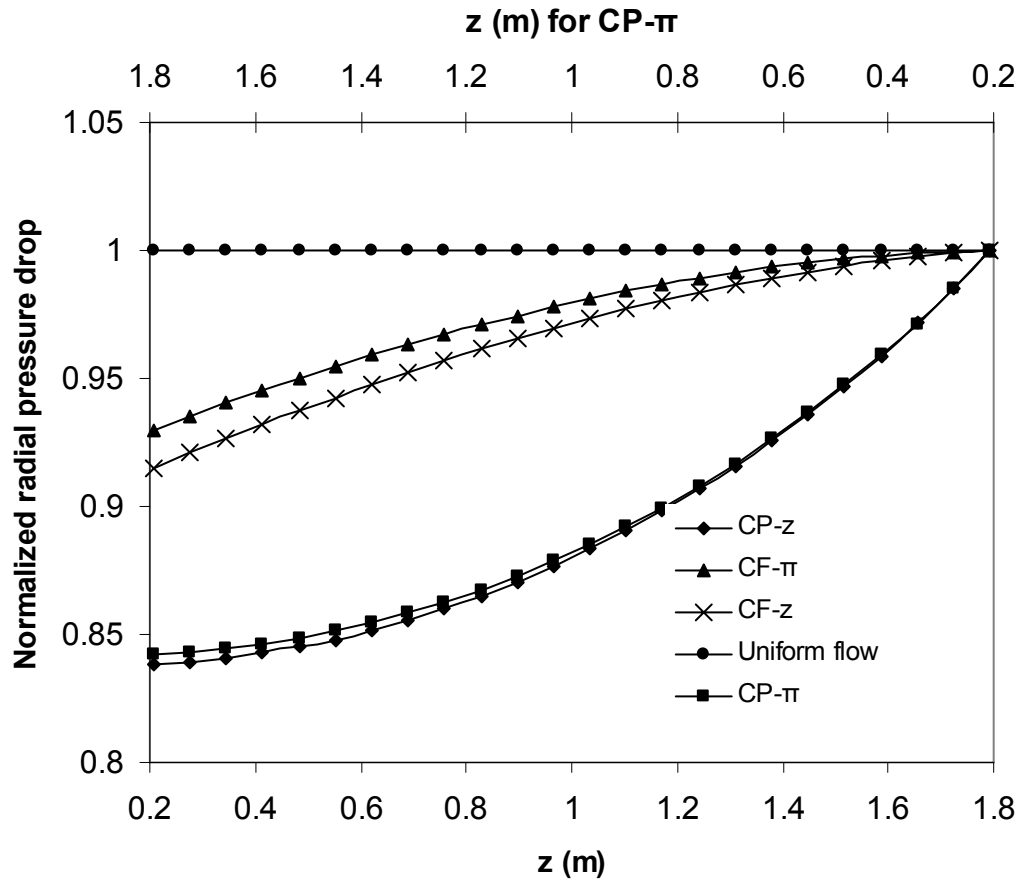


Figure 4.34: Deviation from uniform flow for the four radial flow configurations.

The lowest radial velocity inside the reactor bed occurs at uniform flow. This is preferred since it will have the optimum utilization of the catalyst bed and the minimum occurrence of the pinning phenomena. Therefore at the conditions in Tables 4.1 and 4.2, CF- π is the best configuration. Also it can be concluded from Figure 4.33 that uniform flow distribution gives lower reactor pressure drop.

CHAPTER 5

VALIDATION OF THE NUMERICAL MODEL AND PARAMETRIC STUDY

5.1 CFD Model Validation

The CFD model is validated against two sets of published data. A quantitative validation is carried out against Heggs *et al.* (1995) and a further quantitative validation is carried out against the data of Song *et al.* (1993). Following the validation of the model, the effects of a number of factors, including the ratio of the cross sectional areas of the annular channel and the center pipe, were investigated.

5.1.1 Validation Against Heggs *et al.* (1995)

A CFD model is constructed to simulate the radial flow multi-layered air filter used by Heggs *et al.* (1995). A schematic diagram of the model of Heggs *et al.* (1995) is shown in Figure 5.1. It is a CF-z configuration. The present CFD model simulates an RFBR identical to that used by Heggs *et al.* (1995) with the same flow and boundary conditions. The filter dimensions are shown in Table 5.1. The filter layers specification are shown in Table 5.2. By using Figure 5.1 and Tables 5.1 and 5.2, Heggs *et al.* (1995) multi-layered radial flow air filter is simulated. Three flow rates of 85, 152 and 255 m³/h are used.

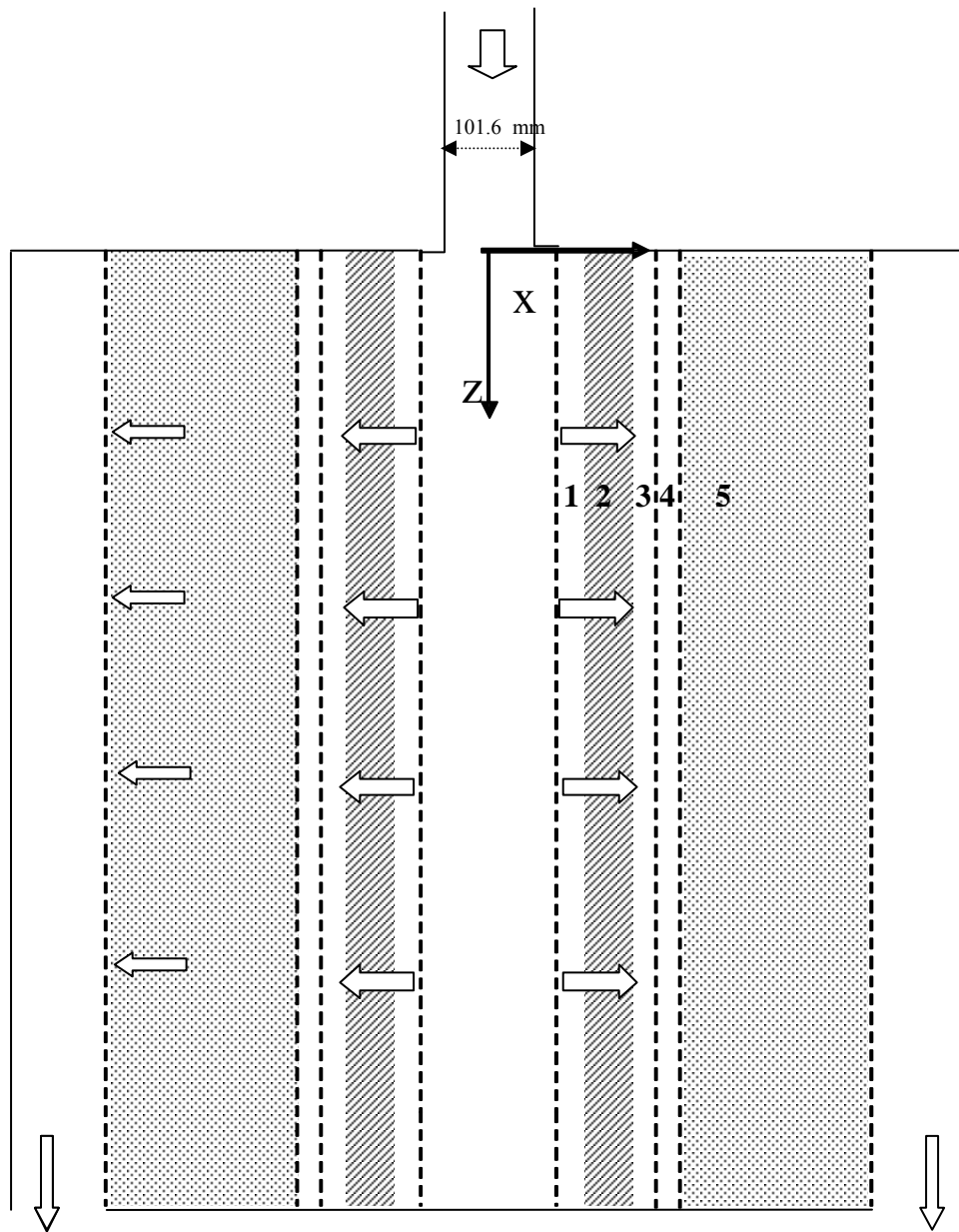


Figure 5.1: Heggs *et al.* (1995) multi-layered radial flow air filter, where 1, 2, 3, 4 and 5 are the bed layers. See Table 5.2 for details.

Table 5.1: Filter dimensions

Dimension*	L_s	L_p	L_b	D_{cp}	D_b	D_r
Value (mm)	0	260	260	126	330	340

*See Figure 4.1 for details of these dimensions.

Table 5.2: Bed layer specifications

Filter Layer	Thickness (mm)	Porosity
Center pipe perforated plate	1	0.326
Bed layer #1 Free space	2	1
Bed layer#2 Particulate filter	37.5	0.1
Bed layer #3 Free space	1.5	1
Internal perforated plate between layers 3 and 4	1	0.227
Bed layer #4 Free space	2	1
Internal perforated plate between layers 4 and 5	1	0.227
Bed layer #5 Carbon bed	56.5	0.412
Annular channel perforated plate	0.5	0.1475

Figures 5.2 and 5.3 show the pressure profiles predicted by the current study for the center pipe and the annular channel respectively, at a flow rate of 85 m³/h. The profile of the center pipe shows a pressure rise since it is the discharge channel and the profile of the annular channel shows a pressure fall since it is the collecting channel. Table 5.3 shows a comparison of the experimental and theoretical results of Heggs *et al.* (1995) and the present CFD simulation results. Heggs *et al.* (1995) also did a comparison between their measurements and predictions for the pressure profiles in the center pipe and the annular channel.

Table 5.3: A comparison of the pressure measurements of Heggs *et al.* (1995) and the current predictions at different flow rates.

Flow rate (m³/h)	Measurement and prediction	Pressure rise in center pipe (Pa)	Pressure fall in annular channel (Pa)	Total pressure drop (Pa)
85	Heggs experimental	5.1	48.1	362.5
	Heggs theoretical	2.0	16.5	380.7
	CFD simulation results	5.3	31.9	345
152	Heggs experimental	16.0	142.9	748
	Heggs theoretical	6.4	53.7	748.6
	CFD simulation results	16.6	97.6	710
255	Heggs experimental	41.3	349.2	1400
	Heggs theoretical	17.9	146.0	1315
	CFD simulation results	45.8	266.8	1428

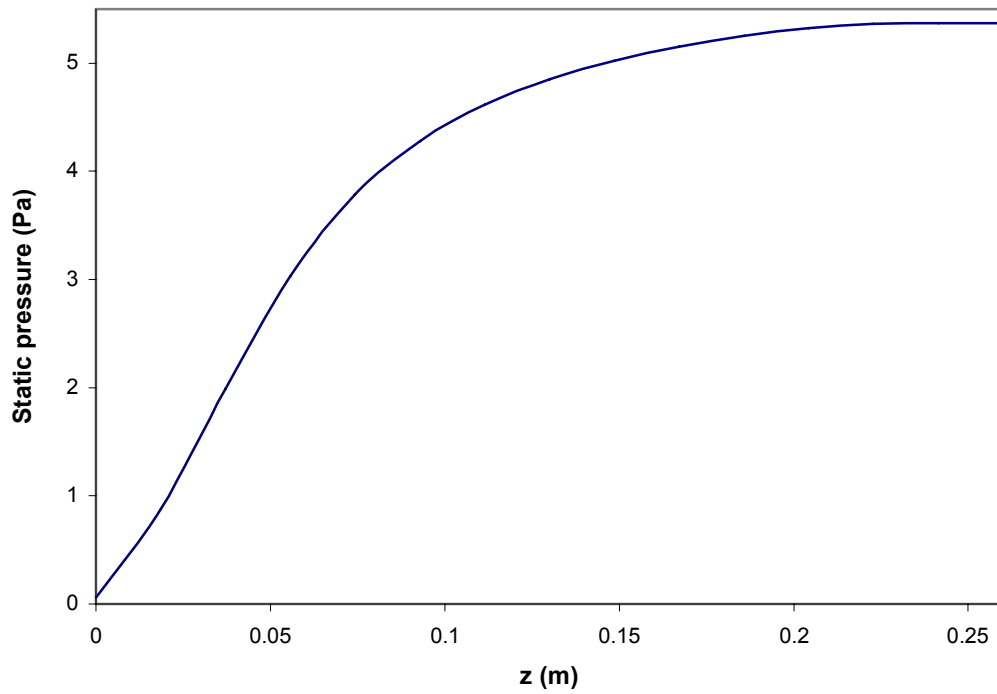


Figure 5.2: Predicted center pipe pressure profile for Heggs *et al.* (1995) multi-layered radial flow air filter at a flow rate of $85 \text{ m}^3/\text{h}$.

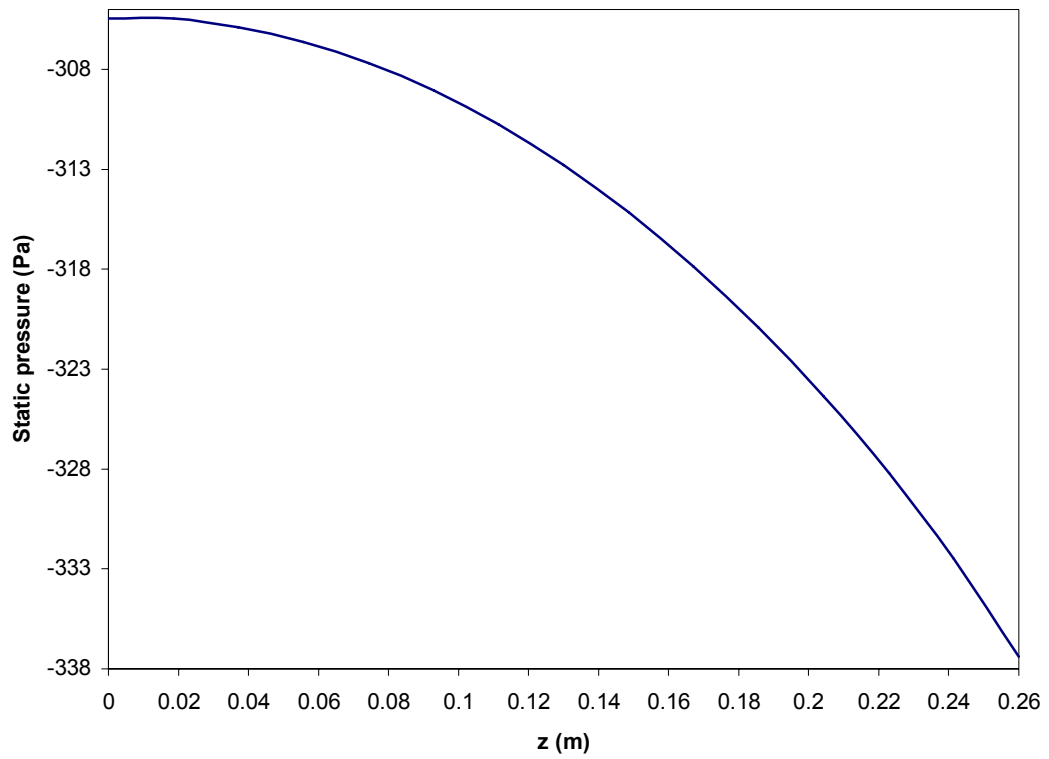


Figure 5.3: Predicted annular channel pressure profile for Heggs *et al.* (1995) multi-layered radial flow air filter at a flow rate of $85 \text{ m}^3/\text{h}$.

The pressure profile for the center pipe was normalized by dividing it by the maximum pressure rise and the pressure profile for the annular channel was normalized by dividing it by the maximum pressure fall. These numbers are also shown in Table 5.3. Figures 5.4 and 5.5 show a comparison of the normalized pressure profiles for the center pipe and the annular channel respectively. Reported results include the experimental and theoretical values of Heggs *et al.* (1995) and the prediction of the present CFD simulation model.

It can be seen from Table 5.3 and Figures 5.4 and 5.5 that the CFD model shows good agreement with experimental measurements. Furthermore, the CFD results are closer to the experimental results than the theoretical predictions of Heggs *et al.* (1995). This is mainly because Heggs *et al.* (1995) did not include the small inlet pipe above the center pipe that is shown in Figure 5.1. The inlet pipe above the center pipe has a smaller cross-sectional area which causes the flow to enter the center pipe as a high velocity jet. This causes a sharp pressure rise at the top section of the center pipe since a high velocity is maintained there and there is almost no flow reduction in the radial direction. Heggs *et al.* (1995) also mentioned that there are other flow obstructions at the inlet of the center pipe. There are no details about these obstructions. Implementing those details is likely to make the CFD results even closer to the experimental measurements. Despite of that the model gives good predictions for such a complex flow in a multi-layered radial flow filter. An advantage shown by the model is that it can include any external piping that may affect the flow profile in the radial flow reactor.

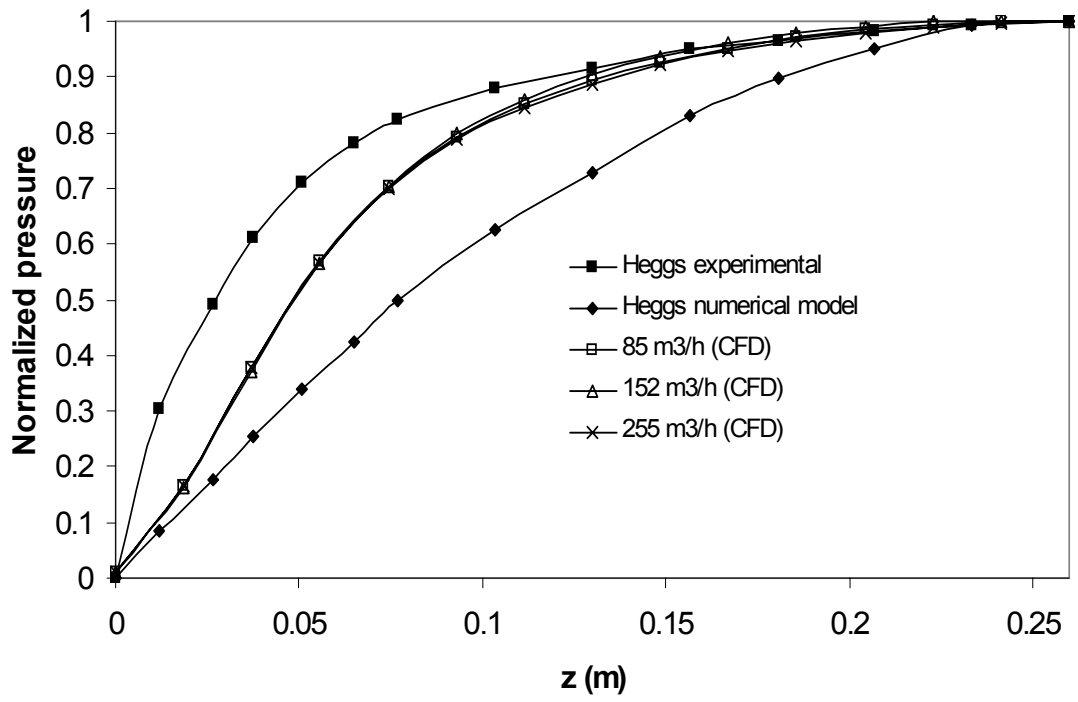


Figure 5.4: A comparison of the profile of the normalized pressure in the center pipe.

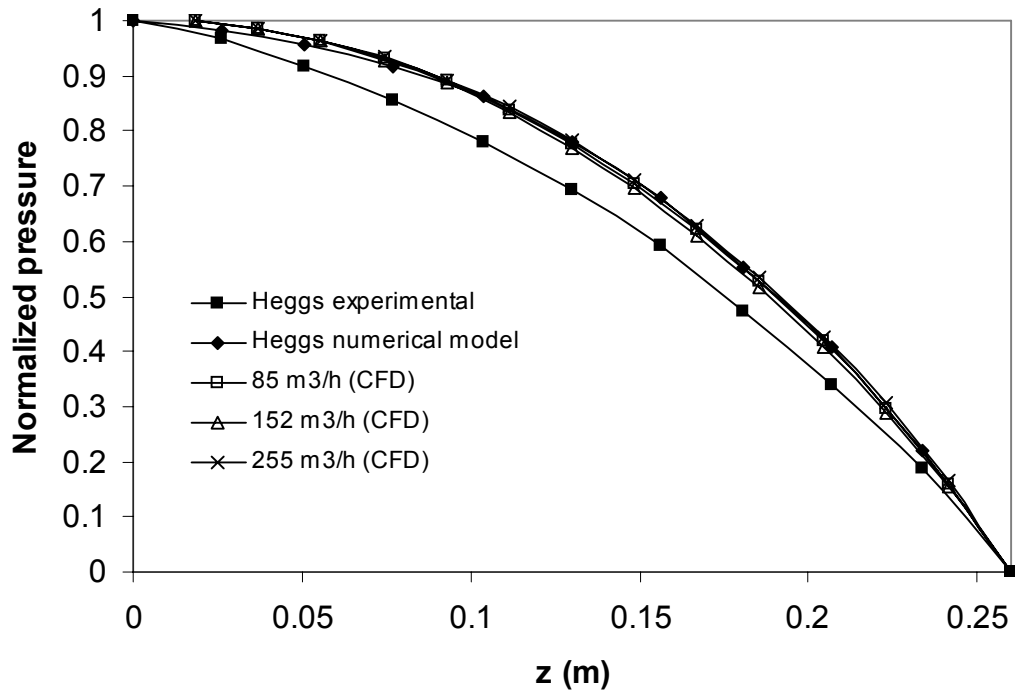


Figure 5.5: A comparison of the profile of the normalized pressure in the annular channel.

5.1.2 Validation Against Song *et al.* (1993)

The RFBR CFD model was also validated against experimental results for an RFMBR. Song *et al.* (1993) experimentally investigated the flow distribution in an RFMBR. The reactor is similar to that shown in Figure 1.3. All four configurations of the radial flow reactor were investigated. Song *et al.* (1993) experimental equipment was modeled without the sections above and below the particle bed. Figure 4.1 shows the model used to validate the present simulation model against the results of Song *et al.* (1993). The model dimensions are the same as those shown in Table 5.4. The flow and boundary conditions for this model are same as those shown in Table 4.2.

Table 5.4: The dimensions of the reactor used by Song *et al.* (1993)

Dimension*	L _s	L _p	L _b	D _{cp}	D _b	D _r
Value (mm)	320	1680	2000	130	410	500

*See Figure 4.1 for details of these dimensions.

To determine the flow distribution in the reactor, Song *et al.* (1993) calculated the maximum axial non-uniformity which is represented by :

$$non - uniformity = 1 - \sqrt{\frac{Radial \Delta P_{entrance}}{Radial \Delta P_{closed \ end}}} \quad (5.1)$$

From Table 5.5, it can be observed that the CFD model shows that the CF- π configuration has the most uniform flow distribution which agrees with the experimental findings of Song *et al.* (1993). However the values of the non-uniformities are much less than those determined by Song *et al.* (1993). One reason of that difference may be the value of C_2 for the perforated plate. Since Equation 3.7 was determined from the equation of the flow through square-edged holes on an equilateral triangular spacing, using it with different holes shape and spacing may lead to the wrong prediction of the perforated plate flow resistance. It seems from the CFD model results that the center pipe and the annular channel perforated plates have a higher resistance which leads to lower non-uniformities. By decreasing the resistance of the center pipe and the annular channel perforated plates, the CFD model results were significantly closer to the experimental results of Song *et al.* (1993) as shown in Table 5.6.

Table 5.5: A comparison of the non-uniformities obtained in the present CFD study with those of Song *et al.* (1993).

Radial flow configuration	non-uniformity	
	Song <i>et al.</i> , (1993)	CFD model
CP-z	0.2	0.032
CP- π	0.2	0.028
CF- π	0.04	0.011
CF-z	0.08	0.015

Table 5.6: A comparison of the non-uniformities by Song *et al.* (1993) with those found using the CFD model after decreasing the resistance of the center pipe and the annular channel perforated plates.

Radial flow configuration	non-uniformity	
	Song <i>et al.</i> , (1993)	CFD model
CP-z	0.2	0.12
CP- π	0.2	0.11
CF- π	0.04	0.044
CF-z	0.08	0.06

The predictions can be further improved by knowing more fine details about the reactor internals, such as the perforated plate resistance. For square-edged holes on an equilateral triangular spacing, Equation 3.7 gives good prediction of the perforated plate resistance as shown in the previous section which discussed the validation against Heggs *et al.* (1995). For other types of holes, the perforated plate resistance is usually given by the manufacturer or can be correlated from experimental results.

5.2 Parametric Study

Following the validation of the CFD model, the effects of the porosity of the center pipe, the annular channel and the bed are investigated. The effects of partially blocking the center pipe top section are also investigated. The dimensions and the boundary conditions shown in Tables 4.1 and 4.2 are used in the following sections.

5.2.1 Effects of the Center Pipe Porosity

Figure 5.6 shows the effect of the center pipe porosity on the flow distribution in a radial flow reactor. As the center pipe porosity decreases, the uniformity of the flow distribution increases. It is also observed that the results of a CF- π configuration with a porosity of 0.05 are closer to the uniform line than those of a CP- π configuration with a porosity of 0.012. Therefore it is not appropriate to select a CP- π configuration for this model. A reduction of the center pipe porosity to obtain a uniform flow distribution produces a high pressure drop in the reactor. Hence it increases the operating cost of the reactor.

5.2.2 Effects of a Low Center Pipe and a High Annular Channel Porosity

In a radial flow reactor, the center pipe porosity is usually low since it controls the uniform distribution of the gas. Figure 5.7 shows that setting the center pipe porosity higher than the porosity of the annular channel perforated plate increases the deviation of the flow distribution from the uniform flow distribution. When the center pipe porosity is 0.012 and the annular perforated plate porosity is 0.3, the flow is close to the uniform distribution. Using a higher porosity of the center pipe causes more flow maldistribution. However the advantage of this change is that it significantly reduces the reactor pressure drop as shown in Figure 5.8. Since the radial velocity at the bed outer diameter is lower than that at the bed inner diameter, using a high resistance at the bed outer diameter will produce lower radial pressure drop. If the radial flow reactor is used in a process that is not highly impacted by

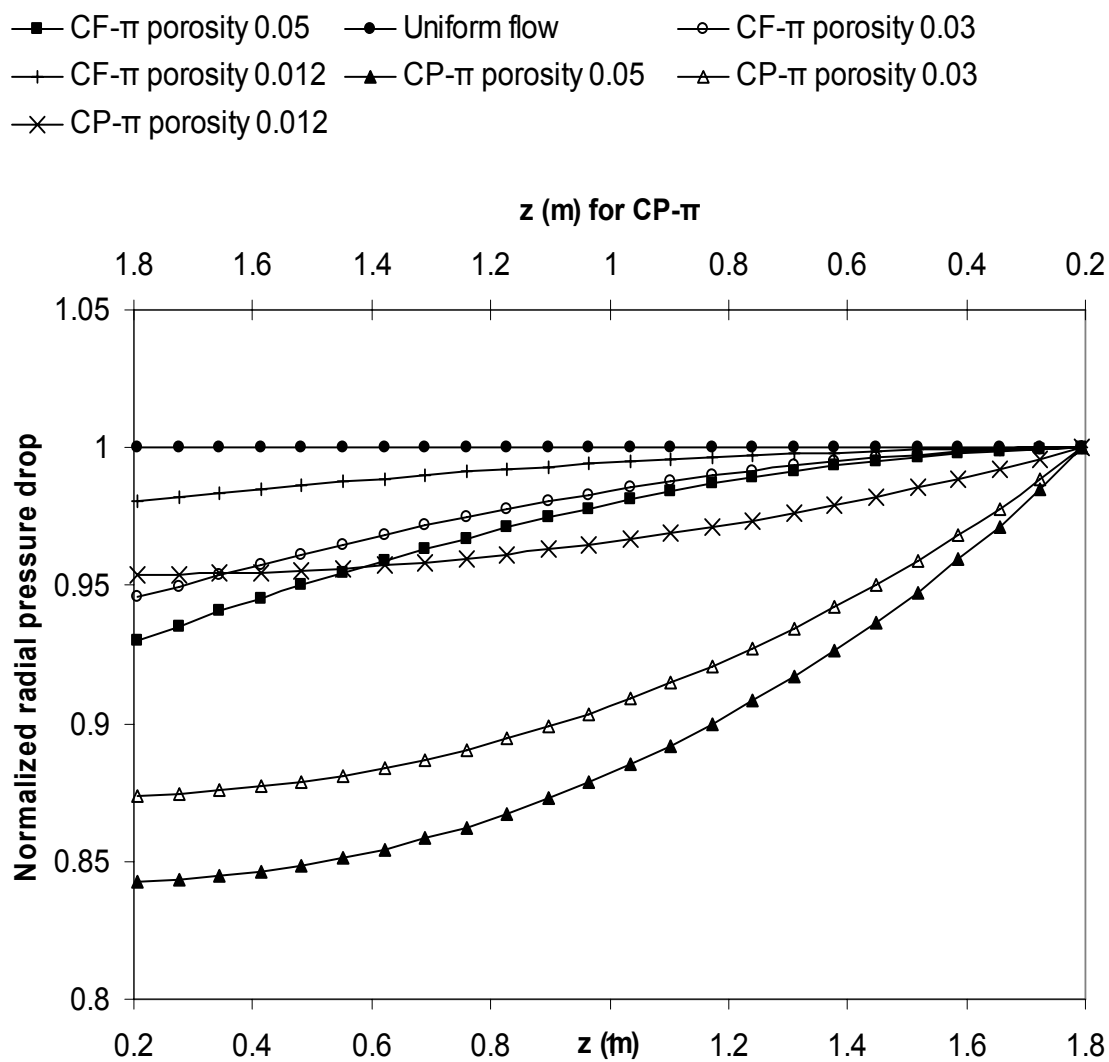


Figure 5.6: Effects of the center pipe porosity on the flow distribution in a radial flow reactor.

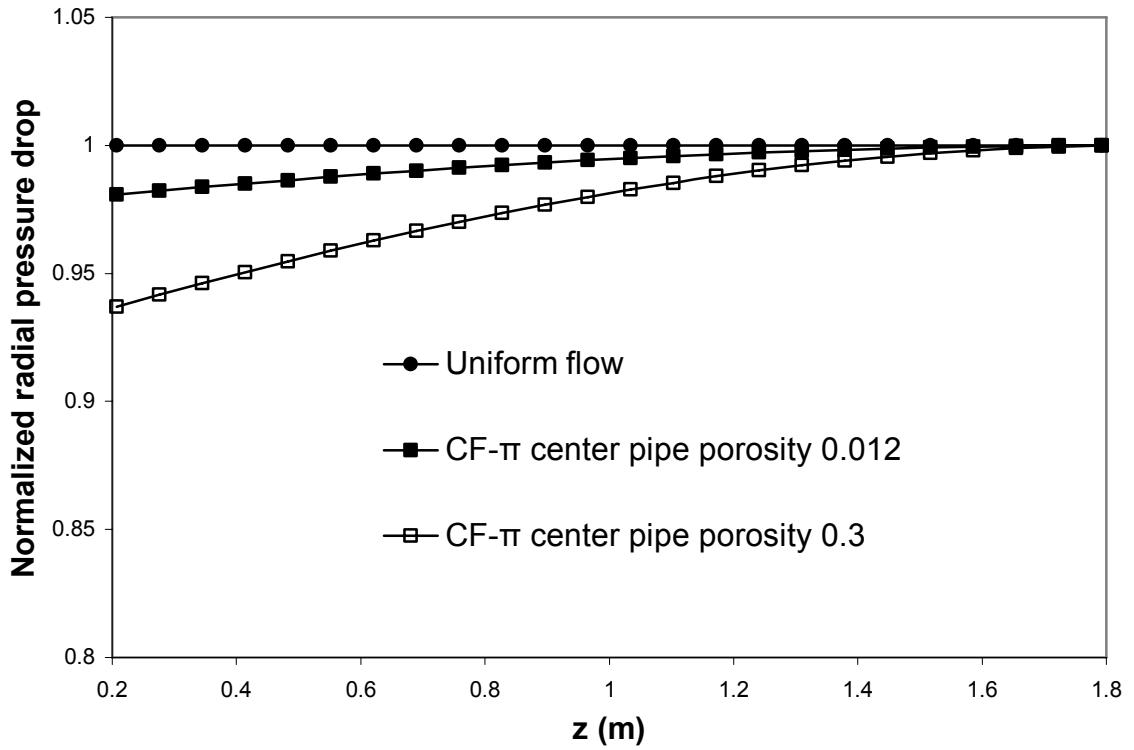


Figure 5.7: Effects of setting the center pipe porosity lower than the porosity of the annular channel perforated plate on the flow distribution.

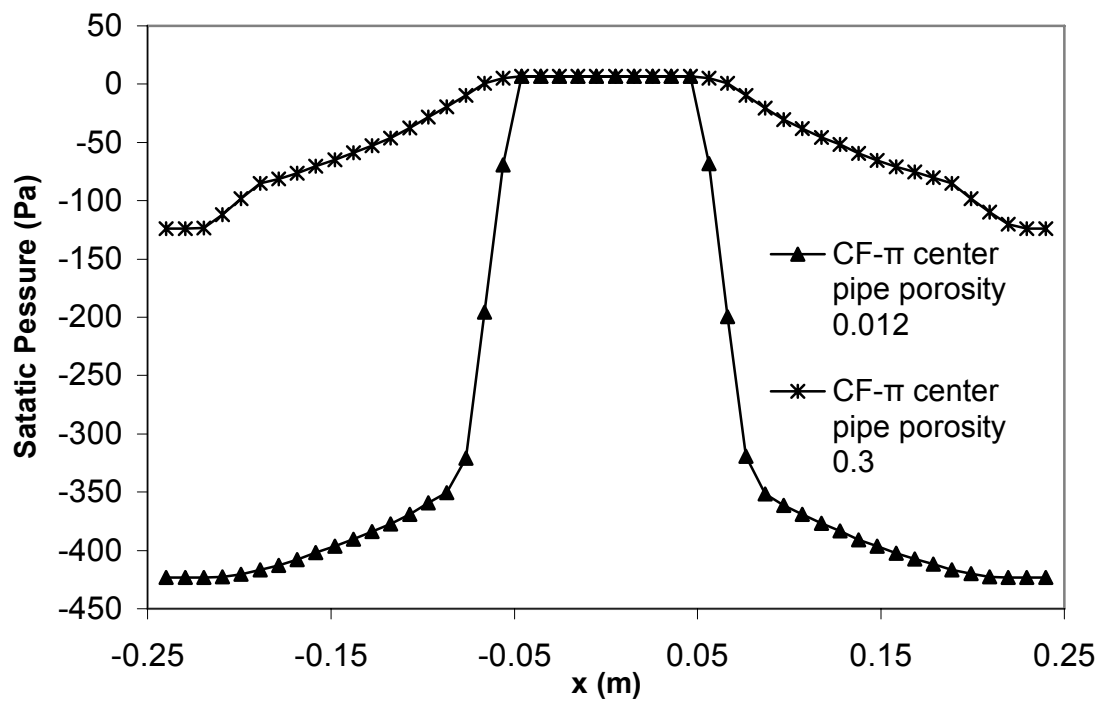


Figure 5.8: Effects of setting the center pipe porosity lower than the porosity of the annular channel perforated plate on the reactor radial pressure profile.

a minor non-uniform flow distribution, such as solid particle drying process, using the high flow resistance at the bed outer diameter may be an economical choice.

5.2.3 Effects of the Bed Porosity

Figure 5.9 shows the effect of the bed porosity on the flow distribution. A low bed porosity improves the flow distribution. Therefore a proper catalyst loading that maintains tight packing of the catalyst should be used to eliminate the flow maldistribution.

5.2.4 Effects of the Ratio of the Center Pipe to the Annular Channel Cross Sectional Area

The effects of the ratio of the center pipe to the annular channel cross sectional area were investigated numerically and experimentally for the CF- π configuration by Genkin *et al.* (1973). It was found that increasing this ratio will improve the flow distribution in a CF- π configuration. Chang and Calo (1981) found that at a ratio of 1, π -flow configurations will have the most uniform flow distribution. Mu *et al.* (2003) found that there is an optimum ratio at which the CP- π configuration has the most uniform flow distribution. In the present work the effects of this ratio for all four radial flow configurations are investigated. Figure 4.36 and Table 5.7 show that a CF- π configuration has the best flow distribution at a ratio of 0.21 (less than one). When this ratio is increased to one, a more uniform flow distribution was achieved by all configurations. Increasing the ratio was done by increasing the center pipe cross sectional area. The annular channel and bed cross sectional areas and the reactor height were kept the same as those in Table 4.1. At ratio of one, π -flow configurations have the most uniform flow distribution as shown in Table 5.7. At a ratio of 1.8

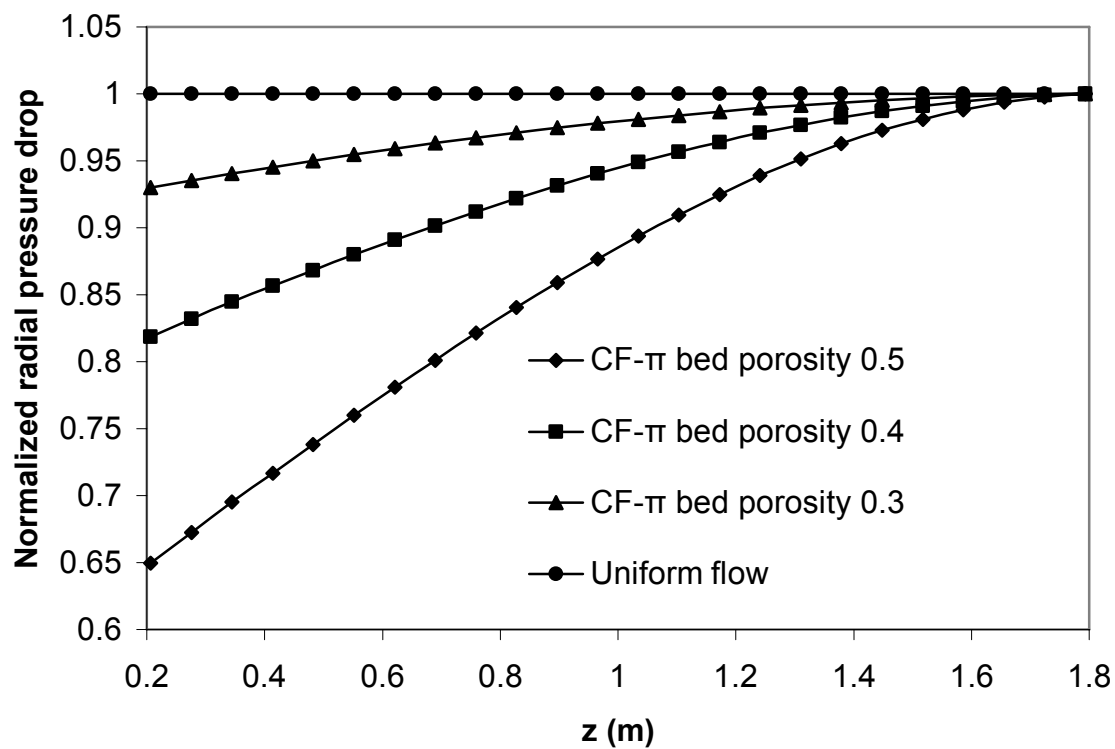


Figure 5.9: Effects of the bed porosity on the flow distribution in radial flow reactor.

(greater than one), a CP- π configuration has the best flow distribution. It seems that both or one of the π -flow configurations will always have the most uniform flow distribution.

Table 5.7: Non-uniformities at different ratios cross sectional areas

Radial flow configuration	non-uniformity		
	Ratio [*] (0.21)<1	Ratio=1	Ratio(1.8)>1
CP-z	0.084	0.013	0.010
CP- π	-0.089	-0.006	0.001
CF- π	0.036	-0.006	-0.013
CF-z	0.044	0.014	0.017

* Ratio: ratio of center pipe cross sectional area to that of annular channel.

The sign of the non-uniformity values for the CF- π and the CP- π configurations change as the ratio increases. This change of the sign of the non-uniformity indicates that an optimum value is passed. The optimum ratio for CF- π configuration is between 0.21 and 1 and that for CP- π is between 1 and 1.8. A high ratio produces a low reactor pressure drop and hence a low reactor operating cost. Therefore the CP- π configuration is the superior configuration for the radial flow reactor.

Increasing the ratio improves the flow distribution and at the same time reduces the reactor pressure drop. However improving the flow distribution by the center pipe porosity produces a higher reactor pressure drop. Therefore in designing a

radial flow reactor it is preferred to find first the optimum ratio that produces the most uniform flow and then manipulate the center pipe porosity to improve the uniformity.

5.2.5 Effects of Partially Blocking the Center Pipe Top Part

The previous parametric studies are applicable to both RFBRs and RFMBRs. A partial blockage of the center pipe perforated wall mainly occurs in an RFMBR. In an RFMBR, the process catalyst is circulated between the reactor system and the regeneration system. Catalyst dust and chip are produced by this circulation. If catalyst dust and chip reach the reactor system, they can plug the reactor perforated holes. In a CP- π configuration and since the flow is towards the center pipe, it usually suffers from blockage. The CFD model was used to simulate the blockage of the top part of the center pipe.

Figures 5.10-5.12 show the radial velocity profiles for a CP- π configuration under different conditions of the center pipe. With a clean center pipe, the radial velocity shows some deviation along the bed height. More flow is coming through the top part of the bed. The maximum radial velocity is 0.22 m/s. At low blockage of the top part of the center pipe, the deviation among the radial velocity profiles increased. The maximum radial velocity increased above 0.23 m/s. At severe blockage of top part of the center pipe, less flow comes through the top part of the bed. The maximum radial velocity increased to 0.26 m/s. Therefore blockage of the center pipe increases the deviation from the uniform flow and in addition to that the increase in the maximum radial velocity may initiate the pinning phenomena.

Designing a reactor with uniform flow distribution can be achieved by adjusting the reactor dimensions and the center pipe porosity. In an RFBR the clean

condition for the perforated plates may not be impacted during the operation. However in an RFMBR, it may be impacted by the operation due to the catalyst circulation. To keep the perforated plates in an RFMBR as clean as possible, dust removal facilities can be installed before the reactor system.

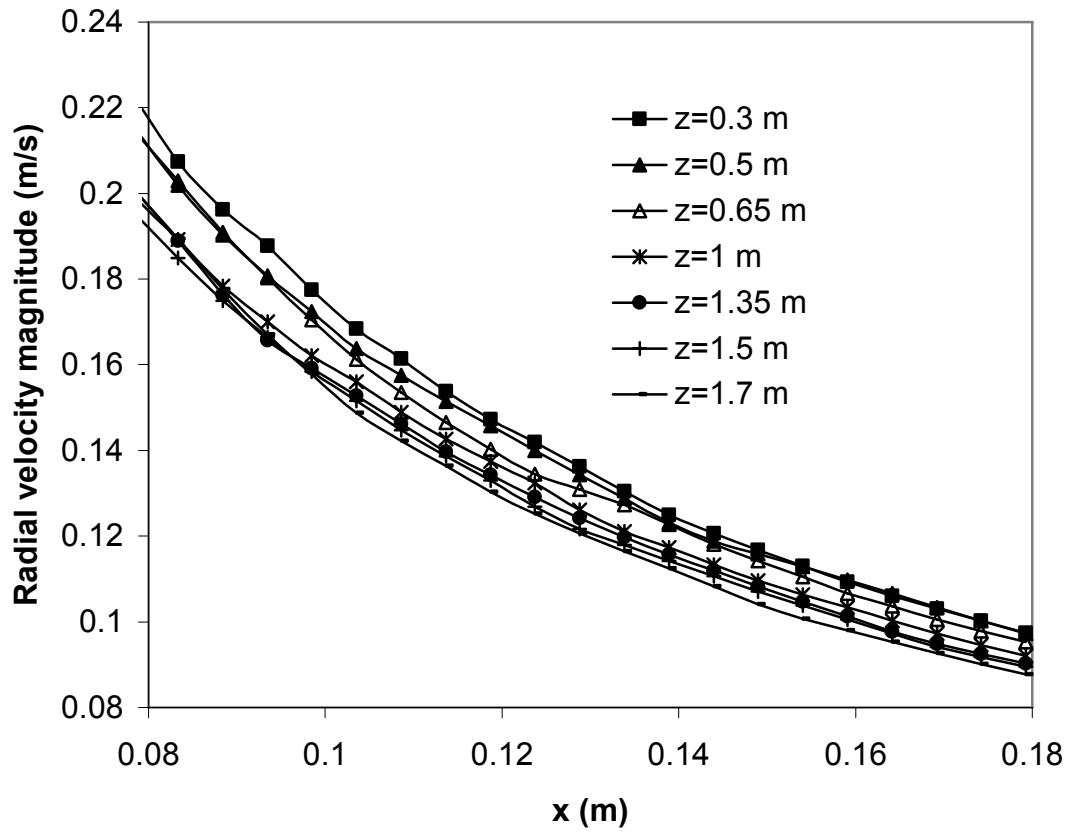


Figure 5.10: CP- π radial velocity profiles at a clean center pipe.

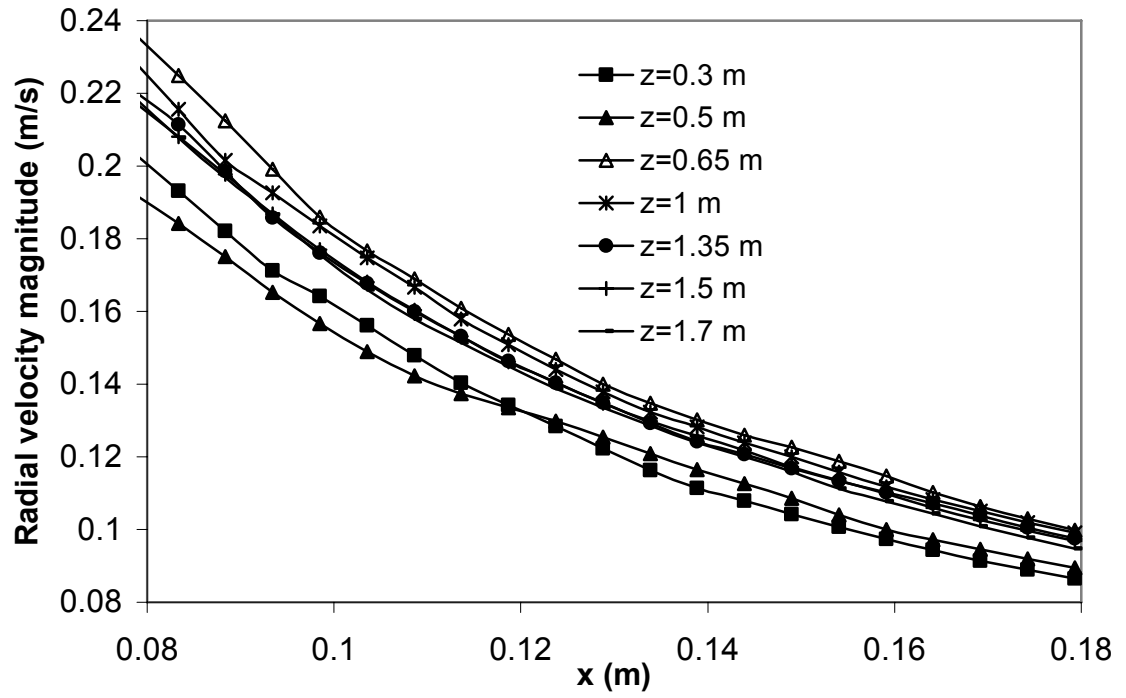


Figure 5.11: CP- π radial velocity profiles with a low blockage of the center pipe top part.

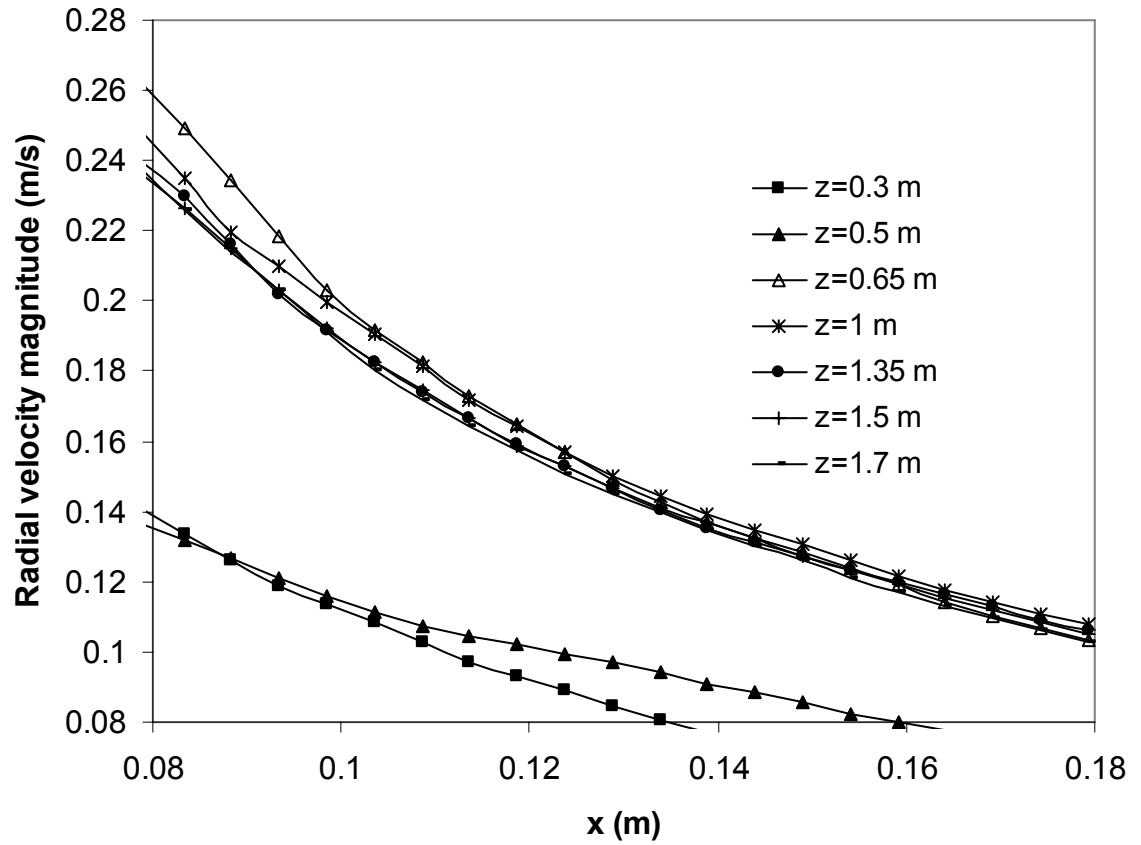


Figure 5.12: CP- π radial velocity profiles with a severe blockage of the top section of the center pipe.

CHAPTER 6

SIMULATIONS OF A MOVING BED REACTOR

6.1 Introduction

Although the fixed bed model in Chapter 4 gives the flow profile in the radial flow reactor and it can be used to minimize the occurrence of the pinning phenomena, it does not quantify the pinning phenomena. Previous researchers such as Ginestra and Jackson (1985), Doyle *et al.* (1986), Tsubaki and Tien (1987), and Song *et al.* (1994), developed models to quantify the pinning phenomena. These models are either applicable only to a simple geometry or subjected to a number of assumptions. Common assumptions used in developing these models are that the flow is distributed equally over the bed and it is uni-radial. These assumptions are valid if the radial pressure drop is totally independent of the axial direction. And if it is true it will be only applied for a clean reactor. A clean reactor can be designed to have uniform flow distribution. However, when it is in operation it will be subjected to many defects such as screen plugging, localized carbon formation, and so on. These defects will impact the flow distribution and divert it from the uniformity. Using these models to predict the pinning phenomena will be risky, since it will under-estimate the pinning phenomena. Also using these models with a contingency factor may over-estimate the pinning phenomena which is not economical. Therefore the best way is to solve the gas flow and the solid motion together. In addition to the complexity of the flow in a fixed bed radial reactor another complexity will be added by the solid flow.

6.2 Moving Bed with a Side Flow Inlet

A model was constructed to simulate downward gas-solid flow in a vertical two-dimensional duct. The duct was 50 cm high and 5 cm wide. A fine mesh and a time step of 1×10^{-4} s were used. A gas stream containing 10% solids is introduced at the top of the duct. The results show that the solid phase accelerates significantly, as expected, under the influence of gravity. The distribution of the solid in the pipe was found to be a function of the pipe diameter.

A side stream was then introduced where gas only is injected and the bed is treated now as a moving bed. The whole vertical duct was set with solids (50%) and was allowed to move down as a moving bed. A number of gas side velocities were used. The results are shown in Figure 6.1, where the effect of the gas rate on the creation of the cavity is clear. The formation of a cavity is the pre-cursor of pinning. As the gas side velocity was increased from 1 m/s to 6 m/s the cavity size was significantly increased. After finding that the model can predict the pinning phenomena, the geometry was converted to moving bed with cross gas flow.

6.3 Moving Bed with a Cross Gas Flow

The next CFD model simulated a downward moving solid bed with gas flowing across the bed this time. Figure 6.2 shows the RFMBR CFD model. Table 6.1 shows the boundary conditions of the CFD model. Gambit was used to construct the model in Figure 6.2. The two dimensional model was meshed uniformly with 0.1 cm step and the number of generated cells is 32,000. Fluent 6.1.22 was used to solve the governing equations of this model.

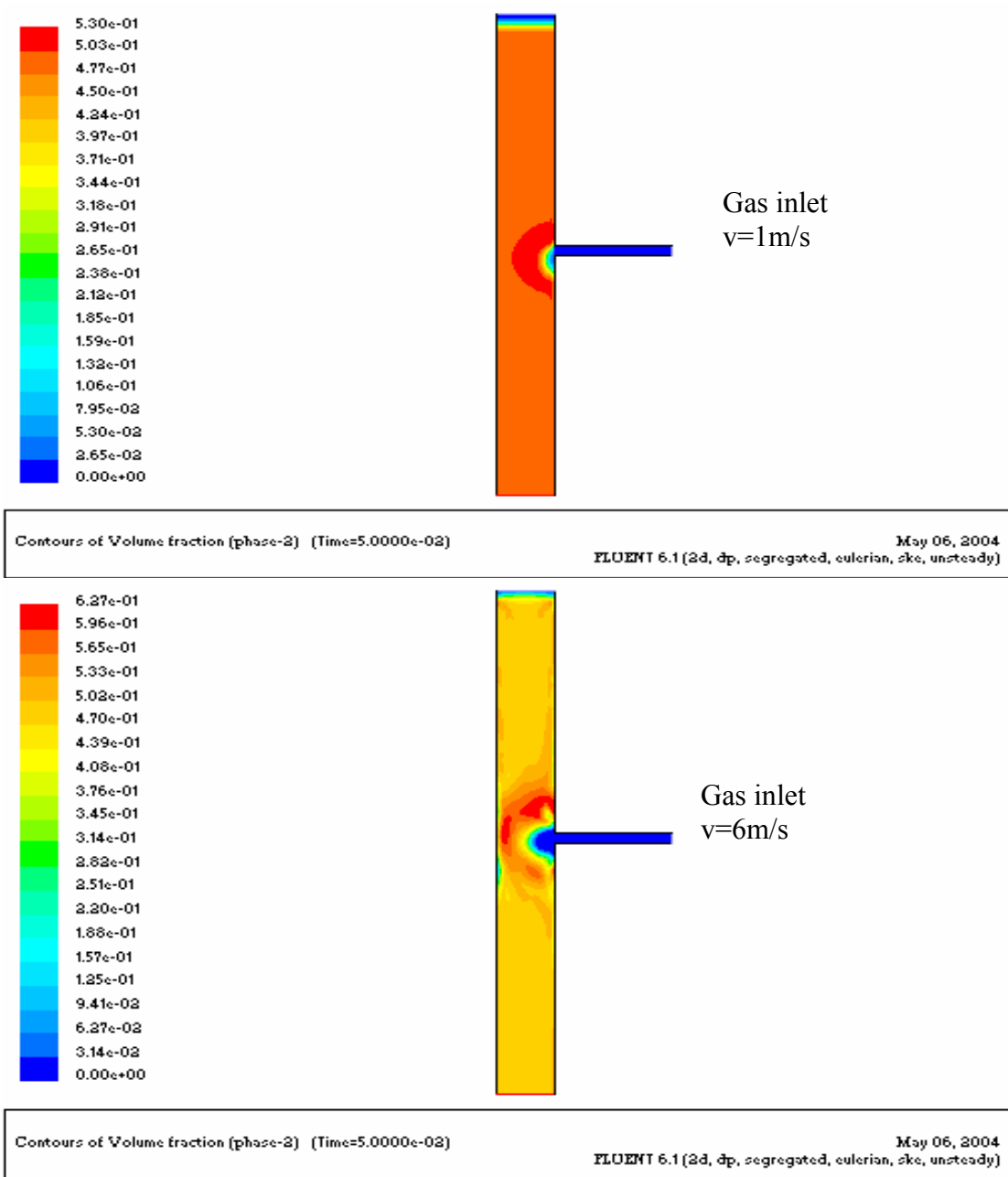


Figure 6.1: Effects of the side gas velocity on the solid movement and the formation of the cavity.

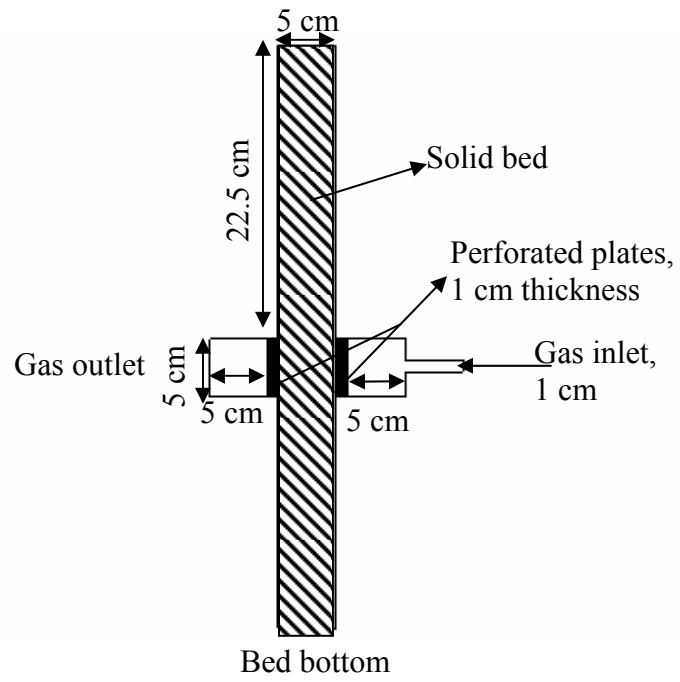


Figure 6.2: A schematic diagram of the RFMBR CFD model.

The simulation was done under unsteady condition with time step of 1×10^{-4} s. The stability criterion, $\Delta t / (\Delta x)^2$, is less than 0.2.

Table 6.1: Boundary conditions of the RFMBR model.

Boundary Condition	Value
Gas inlet velocity (m/s)	3
Gas outlet pressure (psig)	0
Bed top pressure (psig)	0
Bed bottom pressure (psig)	0
Perforated plates porosity	0.5
Solid bed particle diameter (mm)	1.25
Solid bed particle density	1650
Particle-particle angle of friction (deg)	32
Coefficient of restitution, e_s	0.9
Packing limit, $\alpha_{s,max}$	0.63

Figure 6.3 shows the gas velocity vectors at the cross flow section. Figure 6.4 shows the impact of the gas flow on the solid bed volume fraction. Cavity is initiated between the upstream perforated wall and the solid particles. In the next section the effects of gas velocity and solid particles diameter and density on the pinning phenomena are investigated.

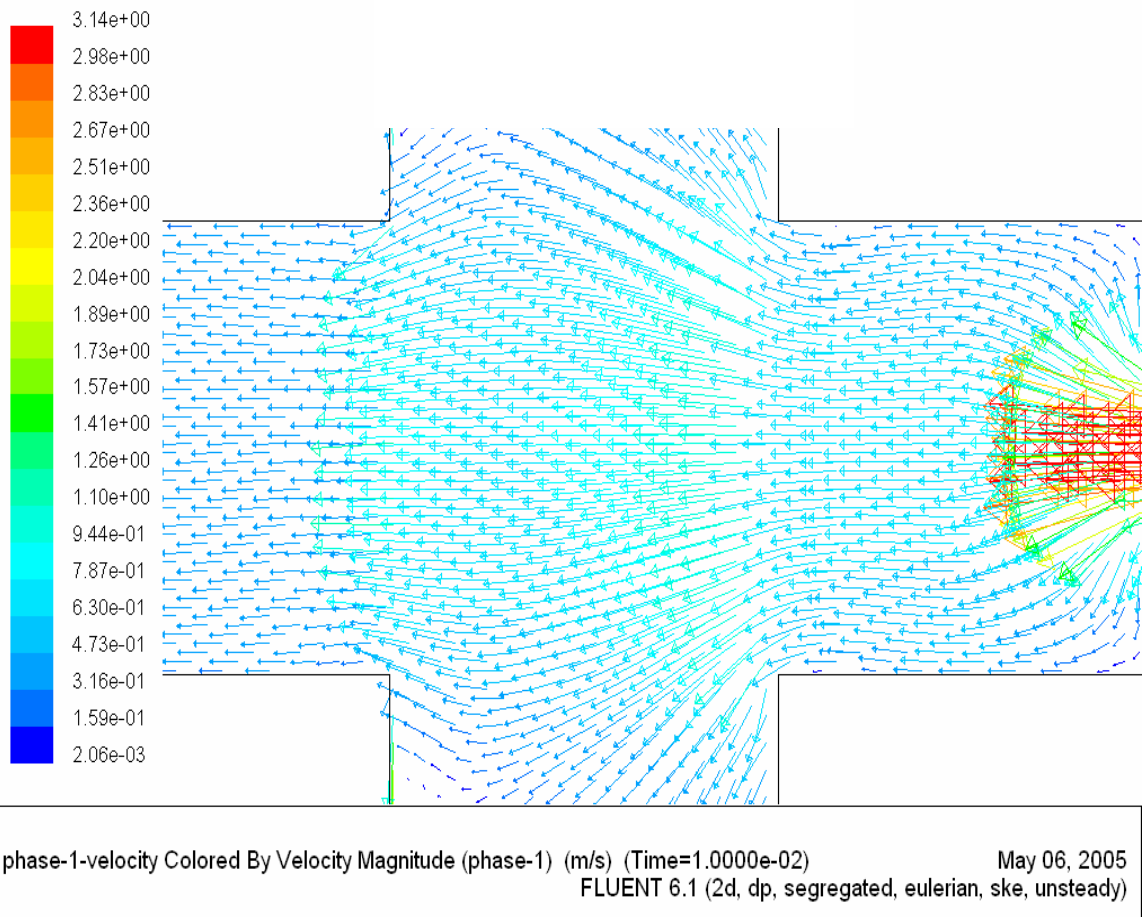


Figure 6.3: Magnified gas velocity vectors at the cross flow section.

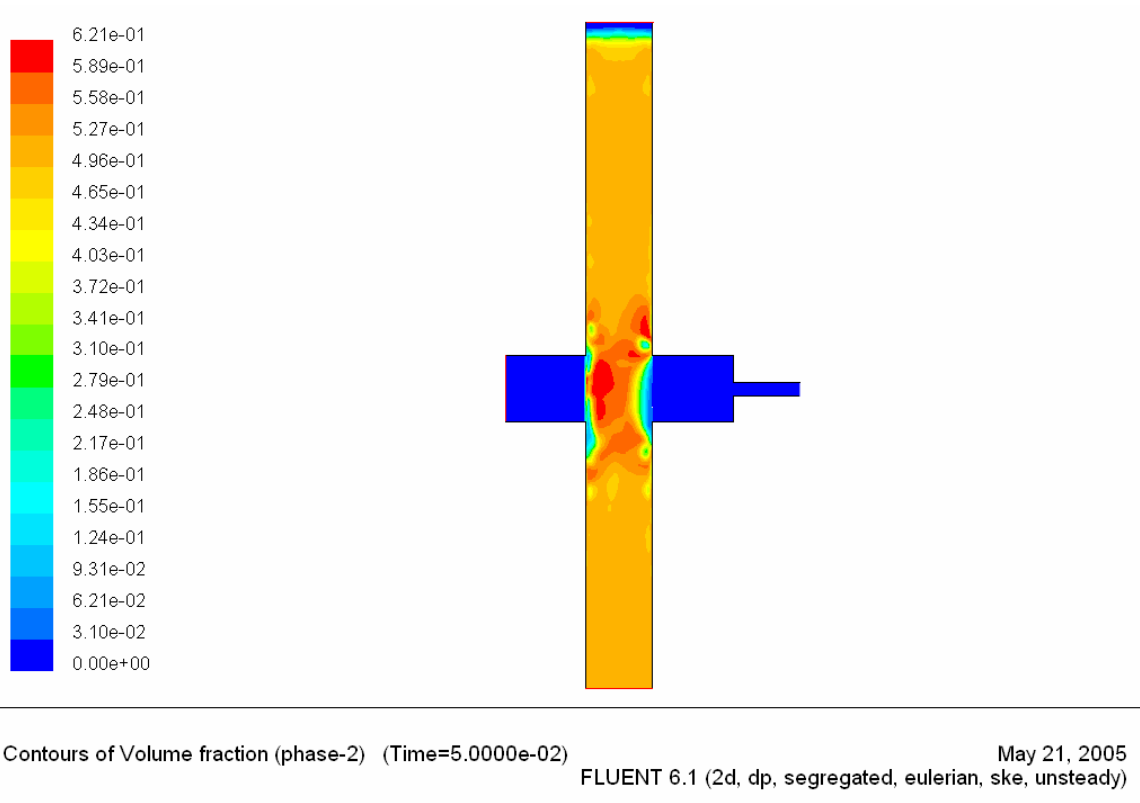


Figure 6.4: Impact of the gas flow on the solid bed volume fraction.

6.3.1 Effects of the Gas Velocity

Figure 6.5 shows that the cavity size increases as the gas side velocity increases. High gas velocity will create high drag force on the solid particles and drive the solid particles away of the upstream perforated wall. Figure 6.6 shows the catalyst volume fraction as function of the inlet velocity. As the velocity increases the solid volume fraction near the upstream perforated face decreases. It can be seen from Figure 6.6 that, at 30 m/s almost half of the bed is empty of solid particles. The velocity effect predicted by the model is in good qualitative agreement with Ginestra and Jackson (1985), Doyle *et al.* (1986), Tsubaki and Tien (1987), and Song *et al.* (1994) theoretical and experimental works.

6.3.2 Effects of the Solid Particle Density

Also the effect of the solid density on the pinning phenomena was studied. It was found that solid with high density has more resistance to the pinning phenomena as shown in Figure 6.7. Increasing the particle density will increase the gravitational force acting on the particle which causes more resistance of pinning phenomena.

6.3.3 Effects of the Solid Particle Diameter Size

Figure 6.8 shows the effect of solid particle diameter on the pinning phenomena. As the diameter increases, particles will have more resistance to the pinning phenomena. A particle with large diameter has more mass and surface area which will reduce the effect of the drag force exerted by the gas.

Effects of the solid particle density and size showed by the CFD model are in good qualitative agreement with Sastry *et al.* (2003) experimental work.

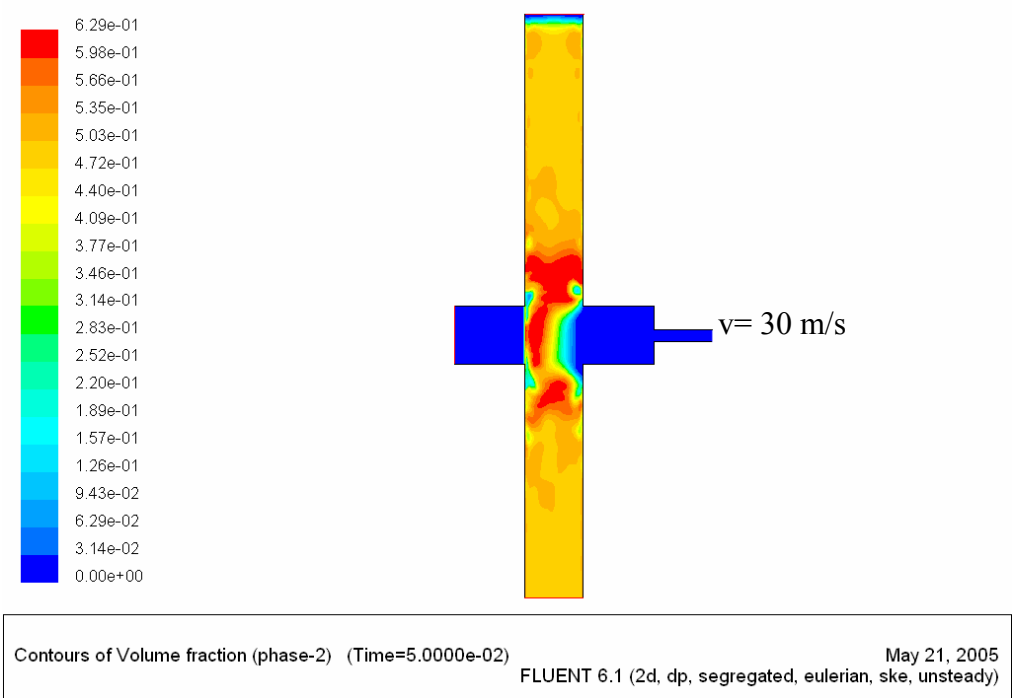
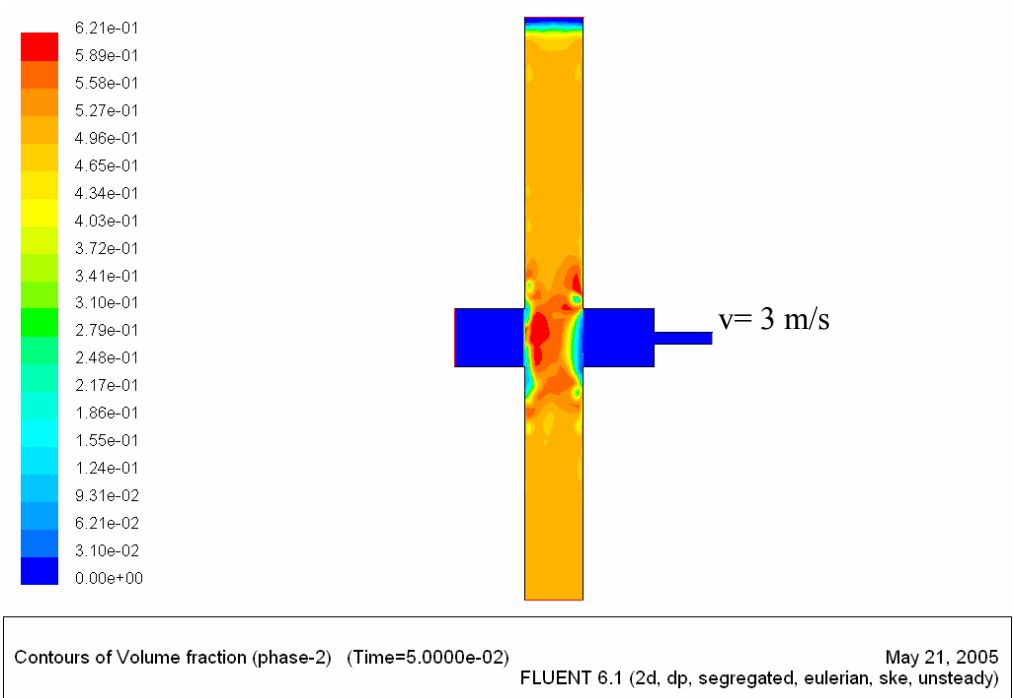


Figure 6.5: Effects of the side gas velocity on the formation of the cavity in an RFMBR.

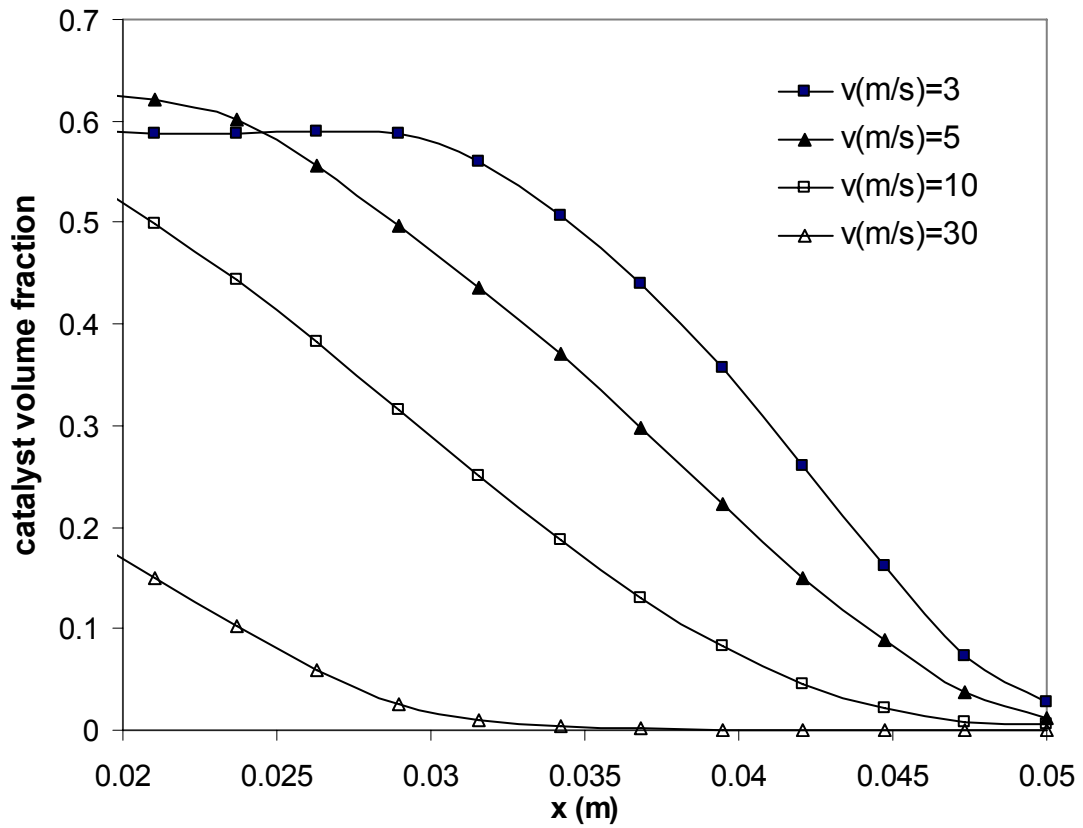


Figure 6.6: Catalyst volume fraction as function of gas velocity inlet, solid particle size and density are 1.25 mm and 1650 kg/m³ respectively.

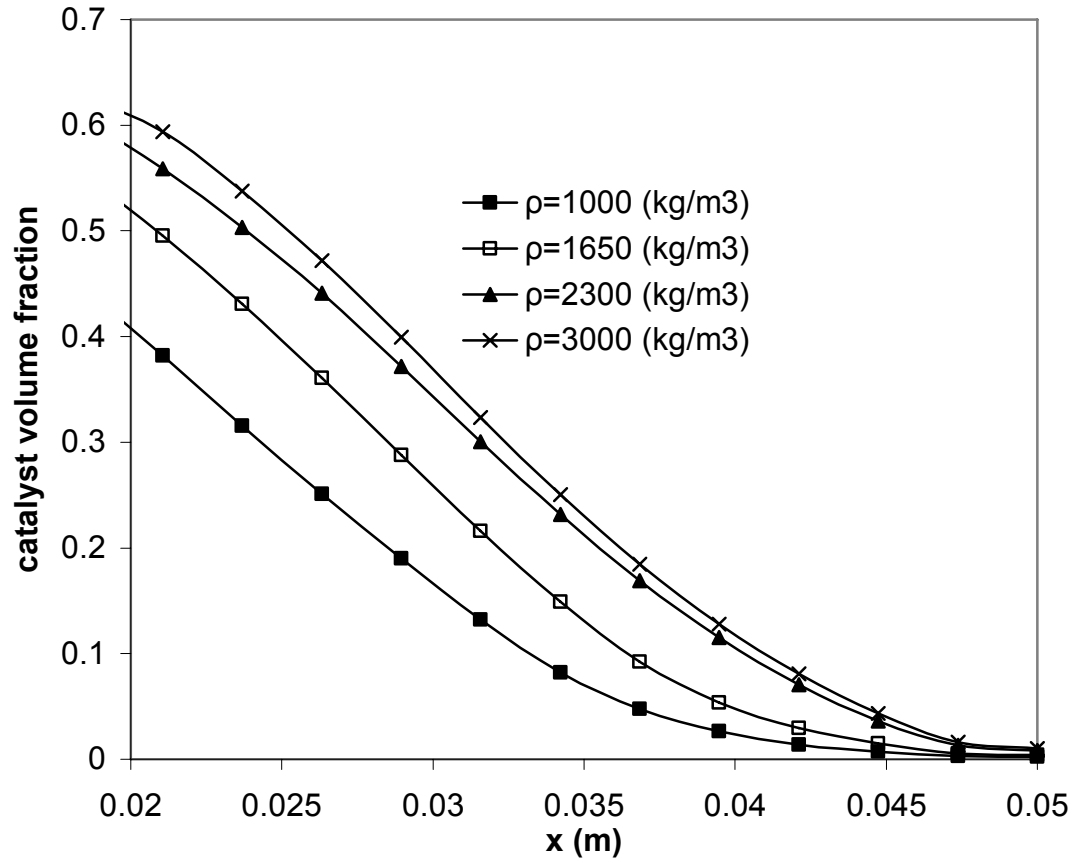


Figure 6.7: Effect of solid density on pinning phenomena, gas velocity is 10 m/s and solid particle size is 1.25 mm.

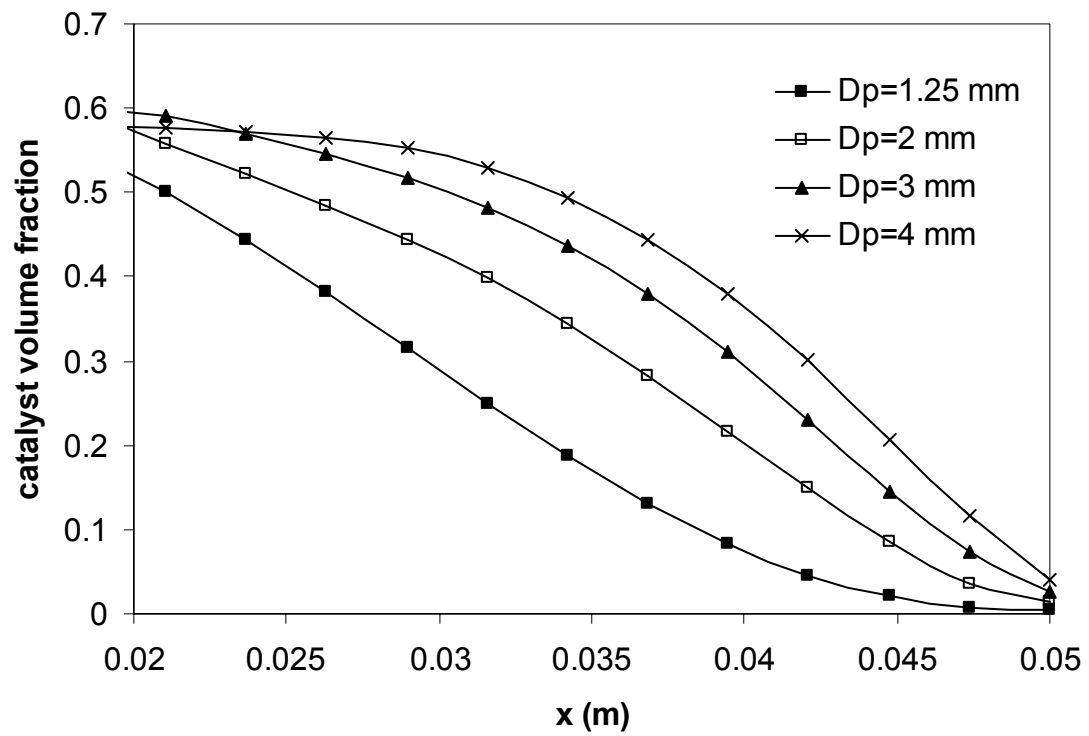


Figure 6.8: Effect of solid particle diameter on pinning phenomena, gas velocity is 10 m/s and solid particle density is 1650 kg/m³.

6.4 Moving Bed CFD Model Limitations

The moving bed CFD model considered both the gas flow and solid motion. However it has the below limitations:

1. CFD simulation of the moving bed reactor is highly expensive. It requires a very small time step, 10^{-4} or 10^{-5} s, to prevent unstable simulation. It required 1 day to get a solution at 0.05 s for the model in section 6.3.
2. Pours-jump model cannot be used for the perforated plate. This makes it necessary to represent the perforated plate with thin porous media. Meshing the geometry with a thin thickness generates a high number of computational cells.
3. From 1 and 2, the model is practically limited to a 2D simple geometry.
4. Particle-wall and particle-perforated plate interaction are not included. Friction between particle and especially the perforated plate is a factor of pinning phenomena.

Despite the above limitations, the moving bed CFD model quantitatively predicted the effects of the flow rate and solid particle density and size on pinning phenomena, and the predictions were in good agreement with published experimental findings.

CHAPTER 7

EXPERIMENTAL WORK

7.1 Introduction

Flow in a radial flow moving bed reactor (RFMBR) has been experimentally investigated by a number of researchers. However not all the reactor parameters were investigated. In this work an experimental set-up was constructed to study the effects of the flow inlet distribution and solid particles properties on pinning phenomena.

7.2 Experimental Set Up

Figure 7.1 shows a schematic diagram of the experimental set-up used in the current study. This set-up consists of a vertical column, 10 cm wide, 10 cm deep and 130 cm high. A central 29 cm section of two opposite faces is perforated. A long particle bed is placed above and below the perforation section (50.5 cm above and below) so that flow is mainly in the horizontal direction. The holes of the perforated faces are 0.3 cm in diameter. There are 15 holes across and 49 holes down each face, which means a total of 735 holes in each face. The porosity of the faces is 0.18. A sheet of fine wire mesh is placed on the inside of each perforated section to prevent solid particles from leaking and blocking holes and to ensure better distribution of radial air flow. This arrangement of holes is advantageous in carrying out parametric runs as it makes varying the porosity down the bed, if needed, possible.

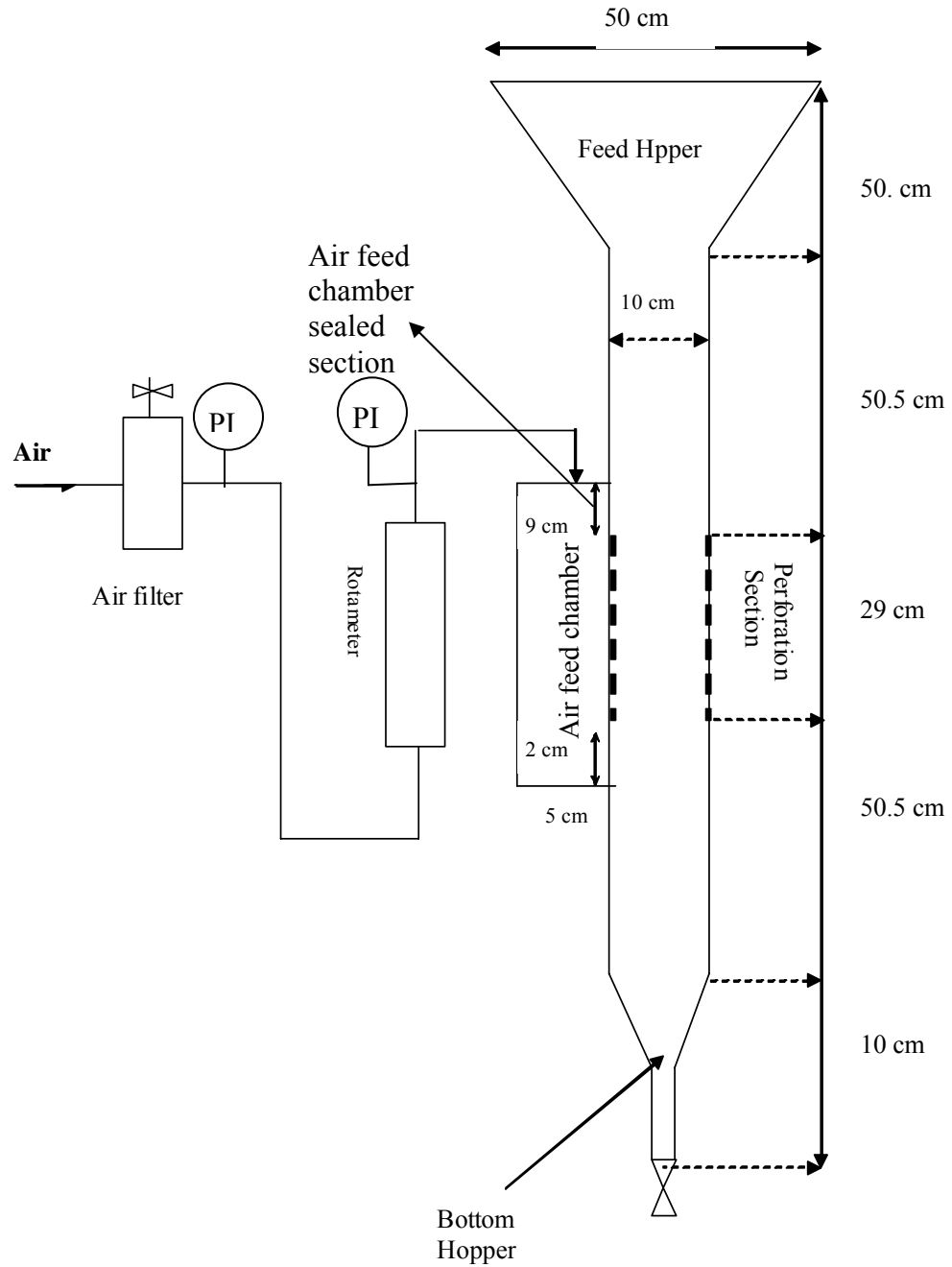


Figure 7.1 A schematic diagram of the radial flow moving bed experimental set-up used in the present study.

A feed hopper is placed on top of the column and a bottom hopper with a valve is connected to the bottom of the column. The rate of solids out is controlled by the valve at the bottom of the lower hopper. The solids velocity is measured using a stop watch. The feed hopper and the bed are filled with solids. The solids are returned manually to the feed hopper keeping the level of solids approximately at a constant level. The feed hopper is kept 70% full.

Air is drawn from the mains. A pressure gauge is placed on the air line. The air passes through two filters to capture the moisture, and then air passes through a rotameter. The rotameter can handle flow rates up to 48 SCFM. The air leaves the rotameter and enters a feed chamber approximating the industrial arrangement in an RFMBR. In an RFMBR the gaseous reactants enter through the scallops, resulting in a flow distribution along the bed height. In the present case, the air feed chamber depth is the same as that of the bed and its width is 5 cm as shown in Figure 1. Three different diameters were used to connect the rotameter to the air feed chamber. These diameters are $\frac{3}{8}$, $\frac{1}{2}$ and $\frac{3}{4}$ of an inch. The smaller the diameter, the more likely the air is to form a jet which in turn will influence the distribution of the radial air flow.

The rotameter is calibrated using an electronic gas meter. In a typical run, the valve is cracked open until the solids move one cycle. Then the solid velocity maintained at less than 2 mm/s. The air flow is then started gradually and is increased in discrete steps until the initiation of the cavity is observed. Air flow is then increased further until a full cavity, pinning, is formed which results in stopping the

solids above the perforated section from flowing. In this case a gas void of solids is created across the air flow. The size of this gap increases until the air flow is reduced so that the solids in the top half of the bed is flowing again.

The shape and location of the cavity is recorded using a digital video camera. Parametric runs are carried out using different diameters of the air inlet and various solids including sago, corn, and high density poly-ethylene (HDPE).

7.3 Characterization of Solid Particles

Four solid materials were used to study the effect of solid particles properties on the pinning phenomena. These solid materials were selected based on the availability of sufficient amount to conduct the tests. Solid particle properties were determined to help in analyzing the results.

7.3.1 Solid Particles size

The size of solid particle was determined by sieve analysis (Bowles, 1992). The sieve analysis was done in the Soil Lab of the Civil Engineering Department at KFUPM. Figures 7.2 shows the cumulative mass percentage frequency curve for the four solids as a function of the particle diameter. Table 7.1 shows the size distribution of the solid particles.

Table 7.1: Size distributions of particles

Particle	>4 mm	3.35-4	2.8-3.35	2.36-2.8	2-2.36	<2
Sago	0	0	0	16.9%	75%	7.8%
HDPE	<1%	92.2%	7.6%	0	0	0
Dukon-corn	0	0	0	13.9%	65.8%	20.2%
White-corn	0	35.4%	57.9%	6%	<1%	<1%

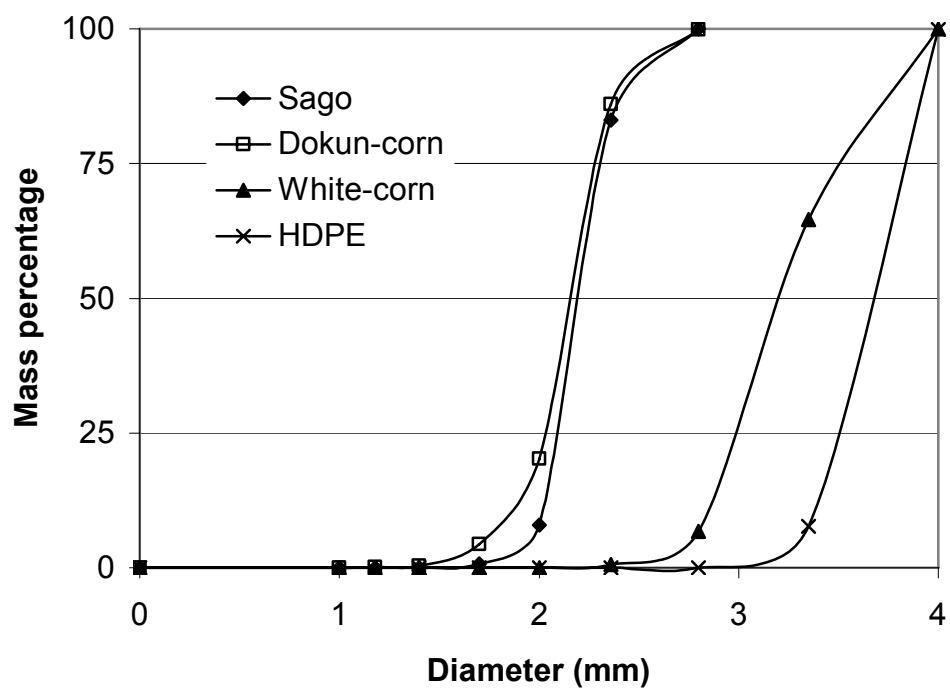


Figure 7.2: Cumulative mass percentage frequency curve using sieve analysis.

The average particle size was determined using the formula below (Allen, 1981):

$$d_p = \frac{\sum \frac{1}{2}(x_i + x_{i+1})dw}{\sum dw} \quad (7.1)$$

where dw is the mass of solid remained on a sieve of size x_i and the next sieve above is of size x_{i+1} . Particle size variation within the solid material was checked using:

$$\sigma_s^2 = \frac{\sum \frac{1}{2}(x_i + x_{i+1})^2 dw}{\sum dw} - d_p^2 \quad (7.2)$$

$$C_s = \frac{\sigma_s}{d_p} \quad (7.3)$$

where σ_s^2 is called the variation and C_s is the variation coefficient. Table 7.2 shows the average particle size and variation coefficient for the four solid materials. Since C_s is much less than 0.5 for all the solid materials, the size of particles can be considered as invariant within each of the solids (Kurz and Munz, 1975).

Table 7.2: Solid particles average size and variation coefficient.

Particle	d_p (mm)	C_s
Sago	2.22	0.09
HDPE	3.63	0.05
Dukon-corn	2.16	0.11
White-corn	3.25	0.11

7.3.2 Solid Particles Form and Sphericity

Solid particle form and sphericity were determined according to the ratio of the three particle axes using the triangular graph of Sneed and Folk (1985).

$$\text{Form} = \left(\frac{S}{L}, \frac{L-I}{L-S} \right) \quad (7.4)$$

$$\text{Sphericity} = \sqrt[3]{\frac{S^2}{LI}} \quad (7.5)$$

where L is the longest axis, I is the intermediate axis and S is the shortest axis. They were measured manually by a ruler. Sneed and Folk (1958) classified particle form in terms of platyness, bladedness, elongatedness, and compactness. Compact form is the closest form to a sphere shape. Table 7.3 shows the form and sphericity of the four solid materials. It can be seen that Sago particle has the closest shape to spherical particle and it can be used to represent the industry catalyst particle used in the moving bed reactor.

Table 7.3: Solid particles form and sphericity.

Particle	Form	Sphericity
Sago	Compact	0.975
HDPE	Compact-Platy	0.713
Dukon-corn	Compact-Elongated	0.796
White-corn	Compact-Bladed	0.746

7.3.3 Solid Particles Density, Bulk Density and Void Fraction

Particles density was determined by the liquid displacement method. Water and acetone were used as the displacement liquids. If V_l is the displaced volume by particles of weight w , the particles density ρ_s is given by:

$$\rho_s = \frac{w}{V_l} \quad (7.6)$$

Particles bulk density ρ_b was determined by measuring the volume V_T of particles of weight w using a graded cylinder.

$$\rho_b = \frac{w}{V_T} \quad (7.7)$$

Since V_T includes the volume of the particles plus the void volume. Therefore particles void fraction ε can be determined by:

$$\varepsilon = 1 - \frac{\rho_b}{\rho_s} \quad (7.8)$$

Table 7.4 shows the particles density, bulk density and void fraction for the four solid materials.

Table 7.4: Solid particles density, bulk density and void fraction

Particle	ρ_s (kg/m ³)	ρ_b (kg/m ³)	ε
Sago	1427	774	0.458
HDPE	971	619	0.363
Dukon-corn	1331	857	0.356
White-corn	1316	815	0.363

7.3.4 Solid Particles Angles of Internal and Wall Frictions

Angles of internal and wall frictions are factors that influence the pinning phenomena as shown by Ginestra and Jackson (1985), Doyle *et al.* (1986), and Pilcher and Bridwater (1990). The angles of internal friction and wall friction for the particle bed were determined from a shear test done in the Soil Lab of the Civil Engineering Department (Bowles, 1992). Table 7.5 shows the internal angle of friction, angle of wall friction and wall friction factor for the four solids used.

Table 7.5: Solid particles angles of internal and wall frictions

Particle	Internal angle of friction (deg)	Angle of wall friction (deg)	Wall friction factor
Sago	52.8	35	0.7
HDPE	34.9	17.7	0.32
Dukon (corn)	27.8	22.3	0.4
White corn	21.3	17.6	0.32

7.4 Experimental Results

The moving bed experimental setup was filled with solid particles. Since it is similar to the industrial catalyst used in the moving bed reactor, sago was used to check the operational and geometrical effects on pinning phenomena. To maintain a uniform bed void fraction, solid particles were allowed to have full circulation prior to introducing the air. As high gas flow rate is the well known cause of pinning phenomena, studying the effect of this flow rate was done first.

7.4.1 Effect of the Flow Rate

Figure 7.3 shows the effect of the gas flow rate on the pinning phenomena. At normal flow rate solid particles move down by the gravitational force with a close contact with the upstream perforated wall. When the gas flow rate is increased, some of the bed particles start to lose contact with the upstream perforated wall. At this condition, a cavity is initiated between the upstream perforated wall and the bed particles. As the flow rate is increased further, the cavity width increases until it spans the whole bed width and prevents the motion of the particles above the perforated section. At this condition the particles bed is at total pinning. Results in Figure 7.3 are in good

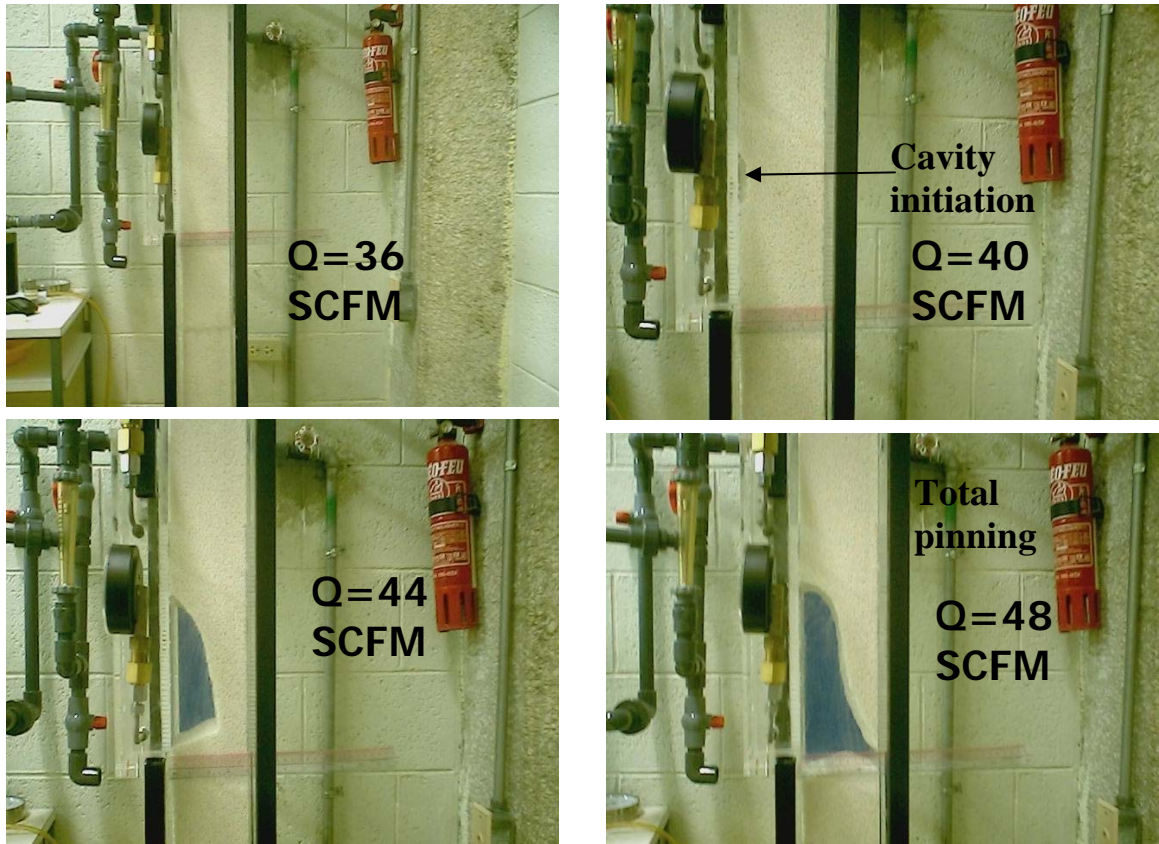


Figure 7.3: Effect of the gas flow rate on the pinning phenomena, using sago solid particles and 1/2 inch air inlet pipe.

qualitative agreement with results of the moving bed CFD model in chapter 6. Figure 7.4 shows the cavity wall profile as function of the air flow rate.

7.4.2 Effect of the Flow distribution in the Air Feed Chamber

To investigate the effects of the flow distribution in the air feed chamber on the pinning phenomena, three different inlet configurations were used. These configurations are 3/8, 1/2 and 3/4 inch inlet pipes. Because the air main header size is 3/4 inch, the selection of maximum size of 3/4 inch was the maximum limit. Since the flow distribution in the air feed chamber depends on the magnitude of the air inlet jet, each of the three inlet configuration is expected to give different flow distribution.

Figures 7.5 to 7.10 show the pinning phenomena at the three inlet configurations. Figure 7.5, 7.7 and 7.9 show the cavity initiation for the different inlet sizes. It can be seen from these figures that for a small inlet diameter, the jet diameter is smaller and the cavity initial height is limited (Figure 7.5). As the inlet diameter is increased, the jet diameter becomes larger and the cavity initial height become larger (Figures 7.7 and 7.8).

The cavity is initiated at the middle of the perforation section because of highest velocity there. As the air flow increases it grows until it spans the whole width of the bed. The final cavity profile at the total pinning is the same for the different inlet size as seen from Figures 7.6 and 7.8.

Table 7.6 shows the bed pressure drop and flow rate for the four inlet configurations at cavity initiation and total pinning. From Table 7.6 it seems that both inlet pressure and flow rate contribute to the pinning phenomena. Using 3/8 and 1/2 inch cause high inlet pressure and therefore high inlet flow jet. This high jet will

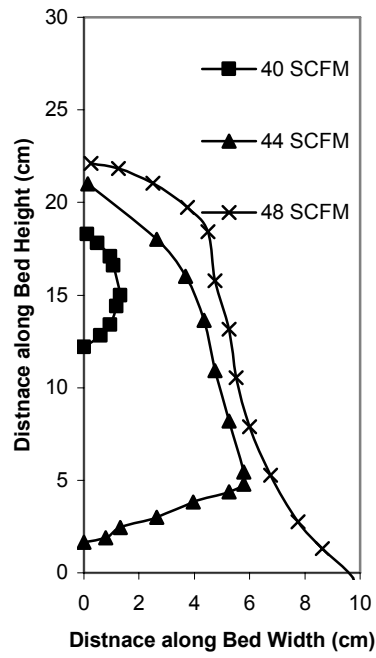


Figure 7.4: Cavity wall profile as a function of the gas flow rate, using sago solid particles and 1/2 inch air inlet pipe.



Figure 7.5: Cavity initiation for 3/8 inch inlet pipe.



Figure 7.6: Total pinning for 3/8 inch inlet pipe.



Figure 7.7: Cavity initiation for 1/2 inch inlet pipe.



Figure 7.8: Total pinning for 1/2 inch inlet pipe.



Figure 7.9: Cavity initiation for 3/4 inch inlet pipe.



Figure 7.10: Cavity profile for 3/4 inch inlet pipe at maximum air flow rate.

cause mal-distribution flow and concentrate the flow at one region which enhances the initiation of cavity. In the case of using 3/4 inch the inlet pressure was very low and so as the inlet jet. Therefore a high flow rate was achieved before the cavity initiation. In addition to that total pinning was not reached even at the maximum possible air flow rate. Therefore the pinning phenomena is affected by the reactor inlet distribution configuration.

Table 7.6: Bed pressure drop and flow rate for the four inlet configurations at cavity initiation and total pinning.

Inlet Pipe Size (inch)		Air inlet pressure (kPa)	Flow rate (ft ³ /min)	Bed pressure drop (KPa)
3/8	Cavity Initiation	81.0	14.87	1.5
	Total Pinning	132.7	15.15	
1/2	Cavity Initiation	68.9	26.95	1.4
	Total Pinning	89.6	31.84	
3/4	Cavity Initiation	24.1	39.90	1.5
	Total Pinning	30	No total pinning observed.	

7.4.3 Using 1/2 inch Inlet Pipe with Distributor

When a 1/2 inch inlet pipe with a distributor is used, the flow distribution in the bed was changed. In this configuration cavity initiated at the top of perforated section as seen in Figure 7.11. This means that highest velocity exists at the top section. By knowing that the highest velocity is at the top section, the porosity of top 30% of the



Figure 7.11: Cavity initiation for a 1/2 inch inlet pipe with a flow distributor.

downstream perforated wall was reduced. This modification eliminated the cavity initiation since it distributed the flow equally along the perforation section.

Figure 7.12 and Table 7.7 show a comparison between using 1/2 inch inlet pipe with and without distributor. Figure 7.12 shows that by changing the flow distribution in the air feed chamber, the cavity initiation location was changed. An inlet pipe with a distributor will produce a better flow distribution in the air chamber than a pipe without distribution, which contributes to preventing the pinning phenomena. However, Table 7.7 shows that cavity initiation when using a pipe with distributor started at lower flow rate. This is because the inlet pipe distributor was close to the start edge of the perforation section. This will force more flow to go to the top section of the bed. To eliminate this problem, flow should be allowed to reach the developed profile before reaching the perforation section. It can be done by increasing the length of air feed chamber sealed section above the perforation section, see Figure 7.1. The experimental setup does not have the flexibility to do this change.

Table 7.7: Bed pressure drop and flow rate for 1/2 inch inlet pipe with and without distributor at cavity initiation and total pinning

Inlet Pipe Size (inch)		Air inlet pressure (kPa)	Flow rate (ft ³ /min)	Bed pressure drop (KPa)
1/2	Cavity Initiation	68.9	26.95	1.4
	Total Pinning	89.6	31.84	
1/2 with distributor	Cavity Initiation	98.3	25.09	1.1
	Total Pinning		No total pinning observed.	

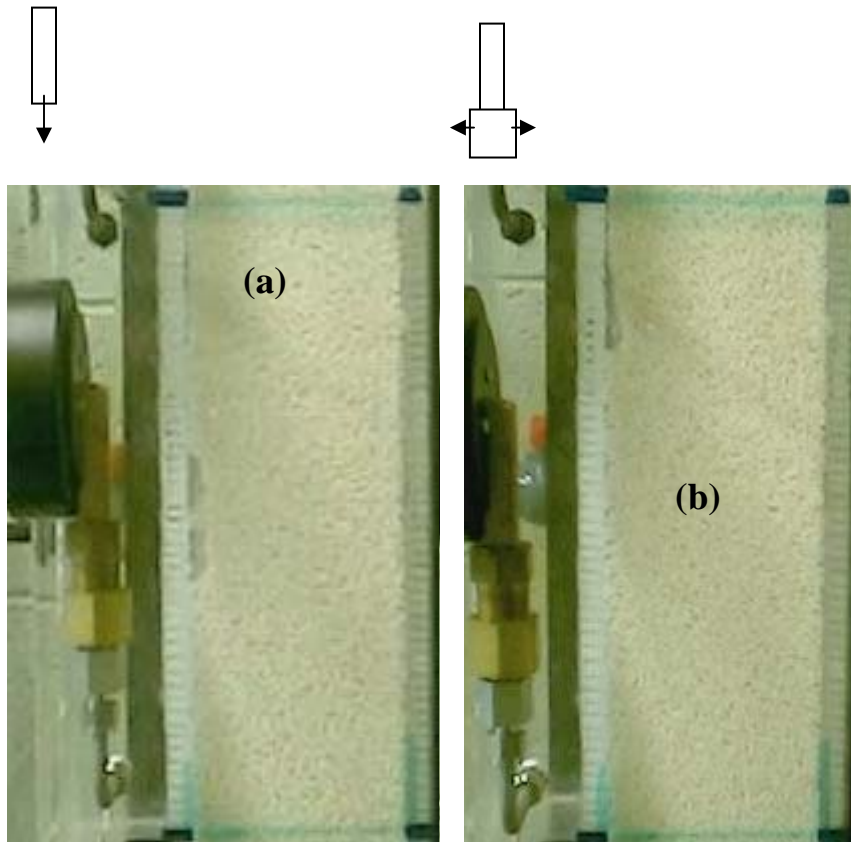


Figure 7.12: Cavity initiation for 1/2 inch inlet pipe with and without distributor, where (a) is for 1/2 inch without distributor and (b) is for 1/2 inch with distributor.

Therefore it can be concluded that, in designing an RFMBR, high jet flow in the annular channel should be eliminated to prevent the occurrence of the pinning phenomena. This can be done by a proper design of the reactor top section that is above the catalyst bed. One way to do that is by making the cross sectional area of the annular channel same as or greater than the reactor inlet pipe. Also, in designing an RFMBR, the flow in the annular channel should be allowed to reach the developed profile before reaching the perforation section. All of these design consideration can be checked using the CFD model developed in Chapter 4.

By knowing the flow distribution in a radial flow moving reactor, modifications can be done to eliminate or reducing the occurrence of the pinning phenomena. The flow profile can be determined by the fixed bed CFD model described in Chapter 4. Therefore using the fixed bed model will help in eliminating the pinning phenomena even though it does not quantify the pinning phenomena.

7.4.4 Effects of the Solid Particles Properties.

In this study, the four solid material characterized in this chapter were used. Table 7.8 summarizes the properties of these materials. The solid shape is not included to avoid complication in the interpretation of the results.

Table 7.8: Solid material properties.

Material	d_p (mm)	ρ_s (kg/m ³)	ε	Internal angle of friction (deg)	Angle of wall friction (deg)
Sago	2.22	1427	0.458	52.8	35
HDPE	3.63	971	0.363	34.9	17.7
Dukon-corn	2.16	1331	0.356	27.8	22.3
White-corn	3.25	1316	0.363	21.3	17.6

The test was done using the 1/2 inlet pipe with a distributor to eliminate the effect of the high mal-distribution caused by pipe without distributor. Table 7.9 and Figure 7.13 show the conditions and the profile for the cavity initiation. White-corn was found the best solid to resist pinning phenomena. White-corn has both high density and high particle size. Although HDPE has the lowest density it showed a similar resistance for the pinning phenomena as Sago and Dukon-corn. HDPE has the highest particle size. Therefore it can be concluded that the pinning resistance of a certain solid particle can be increased by two ways. The first is by increasing its density and the second is by increasing its diameter. This conclusion is in good qualitative agreement with the results of the moving bed CFD model presented in Chapter 6.

Table 7.9: Bed pressure drop and flow rate for various solid materials at cavity initiation.

Material		Air inlet pressure (kPa)	Flow rate (ft ³ /min)	Bed pressure drop (KPa)
Sago	Cavity Initiation	98.3	25.09	1.1
HDPE	Cavity Initiation	100	24.87	1.1
Dukon-corn	Cavity Initiation	86.2	24.74	1.6
White-corn	No cavity	99.3	24.96	1.1

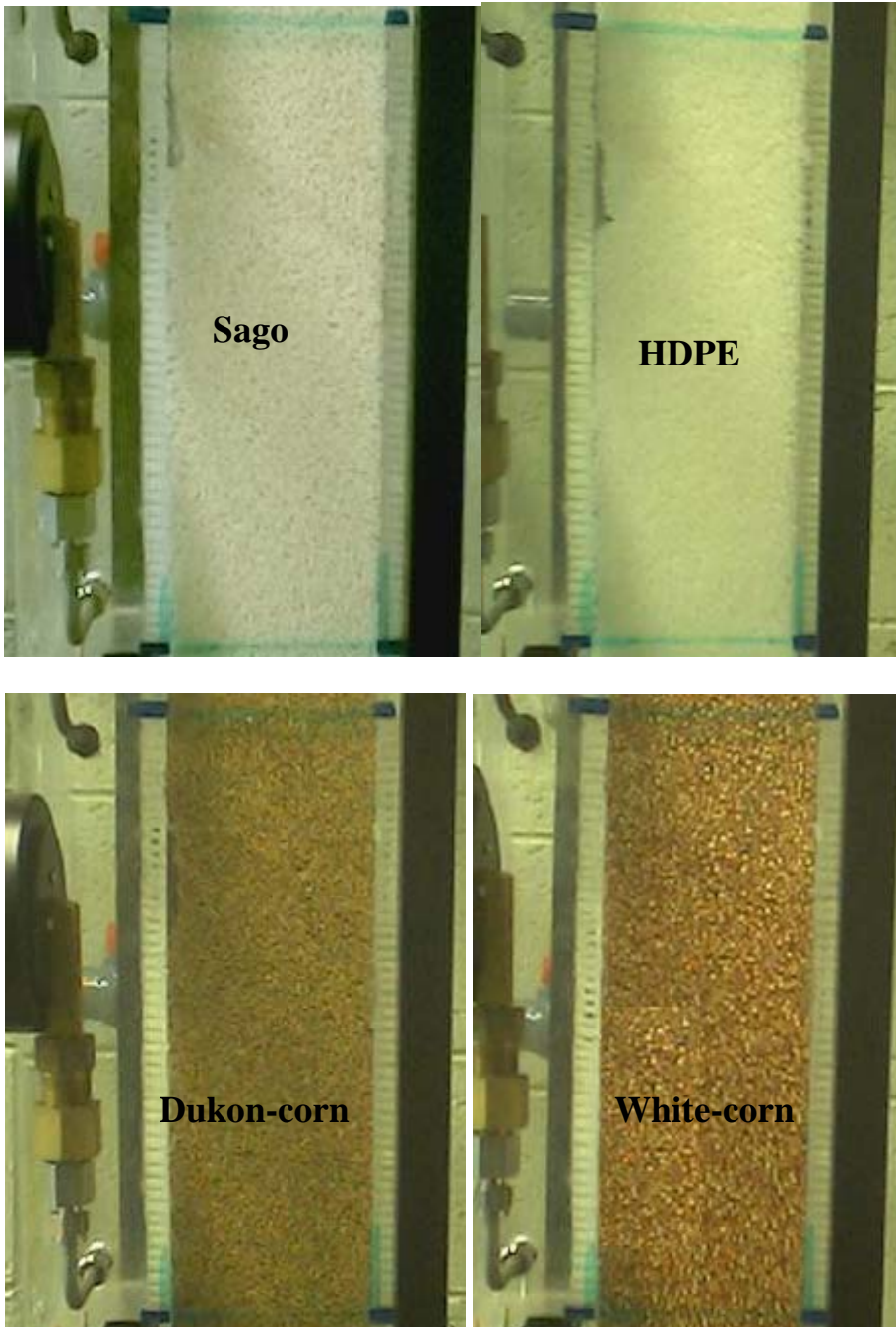


Figure 7.13: Cavity initiation for different solid materials.

7.4.5 Solid Particles Fluidization

An undesired phenomenon was observed during the experimental runs. After the cavity initiation and when the bed motion is stopped, catalyst fluidization will occur between the perforated wall and the cavity wall as seen in Figure 7.14. If this phenomenon occurs in an RFMBR it will create a lot of dust inside the reactor which will plug the reactor screen and contribute to the pinning phenomena.

In an RFMBR unit, the dust is usually generated when the catalyst is moving. However it was found that sometimes when the catalyst motion is stopped for a while and then started a lot of dust is collected. This is may be due to the fluidization phenomena. It seems that having a small cavity in the RFMBR is not major problem, however having fluidization is a major problem.



Figure 7.14: Catalyst fluidization after cavity initiation and stopping the bed motion.

CHAPTER 8

CONCLUSIONS AND RECOMMENDATIONS

8.1 Conclusions

Numerical and experimental investigation of flow and pinning phenomena in radial flow moving bed were carried out. Numerical investigations were done first for the fixed bed and then for the moving bed radial reactor. Comparisons between the numerical results and experimental results were done. The main conclusions of the present study are as follows:

- 1) CFD models for fixed bed radial flow reactor were generated. The models predicted the flow distribution inside the reactor.
- 2) Fixed bed models can predict the flow profile inside a moving bed reactor prior the cavity initiation.
- 3) The four configurations of the radial flow reactor were modeled. Each configuration was found to have a different flow profile.
- 4) For the reactor geometry shown in Table 5.1, CF- π found to have the best flow distribution.
- 5) In addition to optimum utilization of the catalyst bed and minimization of the occurrence of the pinning phenomena at the uniform flow, more power saving is found with a uniform flow. The pressure drop of CF- π is the lowest.
- 6) The fixed bed model was validated against Heggs *et al* (1995) and Song *et al* (1993). Good agreement was found.

- 7) The fixed bed model can be used to improve the flow distribution inside the moving bed and minimize the occurrence of the pinning phenomena.
- 8) The center pipe porosity, bed porosity, ratio of center pipe cross sectional area to that of the annular channel, and blocking the center pipe top section during the operation were found to affect the flow distribution inside the radial flow reactor.
- 9) CFD models for moving bed radial flow reactor were generated. The models predicted the gas and solid flows.
- 10) High flow rate, solid particle size and density were found to affect the pinning phenomena.
- 11) Results produced using the CFD moving bed model are found to be in qualitative agreement with some published results.
- 12) The pinning phenomena were investigated experimentally. Experimental results showed that the pinning phenomena is impacted by the flow inlet distribution.
- 13) Uniform flow distribution over the catalyst bed height will minimize the occurrence of pinning.
- 14) Solid particles properties have a significant impact on the pinning phenomena.
- 15) A undesirable phenomenon was observed when there is a cavity and the solid bed motion is stopped. The catalyst will fluidize between the perforated wall and the cavity wall until the gas flow rate is reduced or the catalyst

motion is resumed. This phenomenon creates a lot of dust in the reactor and contributes to poor flow distribution and to the pinning phenomena.

- 16) Initiation of pinning phenomena in an RFMBR should be always eliminated, since it may cause particles fluidization which will generate dust inside the reactor that will contribute more to the pinning phenomena.

8.2 Recommendations

Based on the present study, below are some areas where further research can be done:

1. Adding reaction term to the RFBR model in chapter 4. This is to study the reaction conversion and selectivity of the four radial flow reactor configurations and the effect of reaction on the flow distribution.
2. Implementing a relation between solid particle and the perforated wall and porous-jump boundary condition to the RFMBR model. This will make the model more stable and computationally less expensive.
3. Adding an outlet chamber to the moving bed experimental set up to run the experiment at z -flow or π -flow configurations and see the difference of each one.

REFERENCES

- Allen, T., “ Particle Size Measurement”, 3rd ed, Chapman and Hall, New York, 1981.
- Antos, G. J., Aitani, A. M., and Parera, J. M., “Catalytic Naphtha Reforming”, Marcel Dekker, Inc, New York (1995).
- Bolton, G. T., Hooper, C. W., Mann, R., and Stitt, E. H., “Flow Distribution Measurement in a Radial Flow Fixed Bed Reactor Using Electrical Resistance Tomography”, Proceedings of 17th International Symp. On Chem. Eng., Hong Kong, 2002, P L Yue 2002
- Bowles, Joseph E., “Engineering Properties of Soil and Their Measurement”, 4th ed., McGraw-Hill, 1992.
- Calo, J. M., “Cell Model Studies of Radial Flow, Fixed Bed Reactors,” *ACS Symp. Ser.*, **65**, 550, (1978)
- Cammarata, L., Lettieri, P., Mical, G. D., and Colman, D., “2D and 3D CFD Simulations of Bubbling Fluidized Bed Using Eulerian-Eulerian Models”, *International Journal of Chem. Reactor Eng.*, vol. 1, A48, 1-15, (2003)
- Chang, H. C., and Calo, J. M., “An Analysis of Radial Flow Packed Bed Reactors-How Are They Different?”, *ACS Symp. Ser.*, **168**, 305-329, (1981)
- Chang, H. C., Saucier, M., and Calo, J. M., “Design Criterion for Radial Flow Fixed-Bed Reactors”, *AIChE J.*, **29** (6) ,1039-1041, (1983)
- Ding, J. and Gidaspow, D., “A Bubbling Fluidization Model Using Theory of Granular Flow” *AIChE J.*, **36** (4), 523-538, 1990.

Doyle, F. J., Jackson, R., and Ginestra, J. C., "The Phenomenon of Pinning in a annular Moving Bed Reactor With Crossflow of Gas", *Chem. Eng. Sci.*, **41** (6), 1485-1495, (1986)

Ergun, S., "Fluid Flow through Packed Columns", *Chem. Eng. Prog.*, **48**(2):89-94, (1952)

FLUENT 6.1 Manual, Fluent Inc., Lebanon, NH USA (1998)

Gary, J. H., and Handwerk, G. E., "Petroleum Refining", Marcel Dekker, Inc, New York (1994)

Gautam, R., Bogdan, P. and Lichtscheidl, J., "Maximize Use of existing assets Through advances in CCR Reforming Catalyst", *European Refining Technology Conference Paris, France*, November 23-24, (1999)

Genkin, V. S., Dil'man, V. V., Sergeev, S. P., "The Distribution of a Gas Stream Over a Radial Contact Apparatus", *Int. Chem. Eng.*, **13** (1), 24-28, (1973)

Gidaspow, D., Bezburuah, R., and Ding, J., "Hydrodynamics of Circulating Fluidized Beds, Kinetic Theory Approach", In *Fluidization VII, Proceedings of the 7th Engineering Foundation Conference on Fluidization*, pages 75-82, (1992)

Ginestra, J. C., and Jackson, R., "Pinning of a Bed of Particles in a Vertical Channel by a Cross Flow of Gas", *Ind. Eng. Fundam.*, **24**, 121-128, (1985)

Heggs, P. J., Ellis, D. I., and Ismail, M. S., "The Modeling of Fluid-Flow Distributions in annular Packed Beds", *Gas Sep. & Pur.*, **8** (4), 257-264, (1994)

Heggs, P. J., Ellis, D. I., and Ismail, M. S., "Prediction of Flow Distributions and Pressure Changes in Multi-Layered Annular Packed Beds", *Gas Sep. & Pur.*, **9** (4), 243-252, (1995)

Hlavacek, V., and Kubicek M., "Modeling of Chemical Reactors-XXV: Cylindrical and Spherical Reactor with Radial Flow," *Eng. Sci.*, **27** , 177, (1972)

Jinfu, W., Zhanwen, W., Yong, J., and Zhiqing, Y., "Simulation of the Gas Distribution System for a Radial Flow Moving-Bed Catalytic Reforming Reactor with Flow Variation", *Shiyou*, **26** (9), 598-605, (1997)

Kurz, H. P., and Munz, G., "The Influence of Particle Size Distribution on the Flow Properties of Limestones Powder", *Powder Technol.*, **11**, 37, (1975)

Leach, B. E., "Applied Industrial Catalyst", vol. 1, Academic Press, New York (1983)

Little, D. M., "Catalytic Reforming, PennWell", Tulsa, OK (1985)

Lobanov, E. L., and Skipin, Y. A., "Increasing The Operating Efficiency of Radial Reactors in Reforming", *Chem. Tech. Fuels Oil*, **22** (5-6), 275-278, May-Jun (1986)

Marb, C. M., and Vortmeyer, D., "Multiple states of A Cross-Flow Moving Bed Reactor: Theory and Experiment", *Chem. Eng. Sci.*, **43** (4), 811-819, (1988)

Meier, H. F., Alves, J. J. N., and Mori, M., "Comparison Between Staggered and Collocated Grids in the Finite Volume Method Performance for Single and Multi-Phase Flow", *Computer and Chemical Engg.*, **23**(3), 247 (1999)

Meyers, R. A., "Handbook of Petroleum Refining Processes", McGraw Hill, New York (1996)

Nooy, F. M., "Dense Lodging", *Oil & Gas Journal*, **82** (46), 152-157, Nov 12 (1984)

Patankar, S. V., "Numerical Heat Transfer and Fluid Flow", McGraw, New York (1980)

Pilcher, K. A., and Bridgwater, J., "Pinning in a Rectangular Bed Reactor with Gas Cross-Flow", *Chem. Eng. Sci.*, **45** (8), 2535-2542, (1990)

Ponzi, P. R., and Kaye, L. A., "Effects of Flow Maldistribution on Conversion and Selectivity in Radial Flow Fixed-Bed Reactors", *AIChE J.*, **25**, 100, (1979)

Ranade, V. V., "Pushing the Limits of Existing Reactor Hardware Using Computational Flow Modeling: a Case of Oxyhydrochlorination Reactor", *Current Science*, **77** (10), 1303-1310, Nov 25 (1999)

Song, X., Wang, Z., Jin, Y., and Gong, M., "Investigations on Hydrodynamics of Radial Flow Moving Bed Reactors", *Chem. Eng. Technol.*, **16**, 383-388, (1993)

Song, X., Jin, Y., and Yu, Z., "Influence of Outward Radial Gas Flow on Particle Movement in an Annular Moving Bed", *Powder Technol.*, **79**, 247-256, (1994)

Sneed, E. D., and Folk, R. L., "Pebbles in the Lower Colorado River, Texas-A Study in Particle Morphogenesis", *Journal of Geology*, **66**, 114, (1958)

Suter, D., Bartoli, A., Schneider, F., Rippin, D. W. T., Newson, E. J., "Radial Flow Reactor Optimization for Highly Exothermic Selective Oxidation Reactions", *Chem. Eng. Sci.*, **45** (8), 2169-2176, (1990)

Syamlal, M., and O'Brien, T. J., "Computer Simulation of Bubbles in a Fluidized Bed." *AIChE Symp. Series*, **85**, 22-31, (1989)

Syamlal, M., Rogers, W., and O'Brien T. J., *MFIX Documentation: Volume I, Theory Guide*, National Technical Information Service, Springfield, VA, 1993.
DOE/METC-9411004, NTIS/DE9400087

Tsubaki, J., and Tien, C., "Solid Velocity in Crossflow Moving Beds", *Powder Technology*, **53**, 105-112, (1987)

Versteeg, H. K. and Malalasekera, W., *An Introduction to Computational Fluid Dynamics*, Longman Scientific & Technical, Essex (1995)

Vora, B. V., and Scott, N. H., "Hydrocarbon Conversion Process with Radial Flow and Controlled Hydrogen Addition", U.S. Patent 4869808, (1989)

Wachem, B.G.M., and Almstedt, A. E., "Methods for Multiphase Computational Fluid Dynamics", *Chem. Eng. J.*, **96**, 81-98, (2003)

Wen, C. Y., and Yu, Y. H., "Mechanics of Fluidization", *Chem. Eng. Prog. Symp. Series*, **62**, 100-111, (1966)

Yang, N., Wang, W., Ge, W., and Li, J., "CFD Simulation of Concurrent-Up Gas-Solid Flow in Circulating Fluidized Beds with Structure-dependent Drag Coefficient", *Chem. Eng. J.*, **96**, 3-13, (2003)

VITA

Name: Aqeel Ahmad Kareeri

Date of Birth: October 16, 1974

Nationality: Saudi

Educational Qualification: B.Sc. Chemical Engineering (1997)

King Fahd University of Petroleum & Minerals

Dhahran-31261, Kingdom of Saudi Arabia

M. S. Chemical Engineering (2004)

King Fahd University of Petroleum & Minerals

Dhahran-31261, Kingdom of Saudi Arabia